

A COST-EFFECTIVE, NONINVASIVE DUAL IMPEDANCE-BASED WEARABLE
FOR CONTINUOUS MONITORING OF CARDIOVASCULAR HEALTH:
DEVELOPMENT OF THE ANALOG FRONT-END

A Thesis

by

LAUREN D. YAMTHE

Submitted to the Graduate and Professional School of
Texas A&M University
in partial fulfillment of the requirements for the degree of

MASTER OF SCIENCE

Chair of Committee,	Gerard L. Coté
Committee Members,	Limei Tian
	Kamran Entesari
	Arum Han
Head of Department,	Miroslav M. Begovic

May 2023

Major Subject: Electrical Engineering

Copyright 2023 Lauren Deuna Yamthe

ABSTRACT

Vulnerable populations are considered high-risk for CVD development by experiencing a combination of low socioeconomic status, reduced access to healthcare, and/or genetic traits that increase susceptibility to CVD risk factors. Due to elevated mortality rates from CVDs in these areas, there is a need for low-cost, wearable devices that are capable of monitoring cardiovascular health for early detection and prevention. One approach for predicting the onset of CVDs includes the tracking of blood pressure (BP) and heart rate. This work focuses on the development of the analog front-end for a bioimpedance-based device that is cost-effective, noninvasive, and cuffless for the monitoring of cardiovascular health by continuous detection of heart rate (HR) and pulse transit time (PTT), which is another method that has the potential to be used for indirect BP measurement without the need for a cuff.

Bioimpedance (BIO-Z) is a favorable modality for CVD health monitoring by allowing for deep tissue penetration and conformability to a wearable format. The continuous measurement of BIO-Z corresponds to the impedance plethysmography waveform (IPG) where HR can be detected and monitored. A dual-IPG format permits continuous PTT acquisition and continuous, cuffless BP measurement. Therefore, two subsystems for dual-IPG measurement were designed and tested: the current driving and voltage sensing networks. The circuits were made into a prototype and its performance for continuous HR/PTT measurement was assessed through direct comparison with a benchtop, impedance cardiography system.

A second iteration of the dual-IPG device was fabricated into a compact, printed circuit board. An automatic feedback loop that continuously detects the magnitude of the injected current and shuts the system down if the applied current exceeds 1 mA and/or electrical safety standards was integrated and evaluated. The characteristics and accuracy of the current monitor was investigated by comparing the system's output with a multimeter. Calibration curves were then obtained and utilized for converting the system's output to the standard impedance unit: ohms. Lastly, after validating the calibration approach, an in vivo study was conducted to obtain the HR, PTT, basal impedance and pulsatile impedance of six test subjects.

DEDICATION

This thesis is dedicated to young, underrepresented minorities in STEM. May all your goals, aspirations, and dreams come true despite the statistics.

ACKNOWLEDGEMENTS

First and foremost, I would like to thank God for getting me to this point and continuing to mark the path for my future.

I would like to thank my committee chair, Dr. Gerard Coté for taking a chance on me and offering the opportunity to work in the OBSL lab. I appreciate your guidance, support, and encouragement throughout my graduate career.

I would also like to thank my committee members, Dr. Limei Tian, Dr. Arum Han, and Dr. Kamran Entesari for their support and counsel throughout the course of this research.

Additionally, I would like to thank the faculty and staff of the Electrical Engineering and Biomedical Engineering departments for making my time at Texas A&M University a wonderful experience. I am very proud to be a product of some of the best engineering programs in the nation.

I would also like to thank the OBSL research engineers, Cody and Richard. Thank you for your contributions to this body of work. I could not have implemented these designs without your help.

Thanks also goes to all the past and current members of the OBSL lab. Graduate school is not something that should be experienced alone. I am grateful for the colleagues that extended help, guidance, and time to brainstorm concepts or just talk in general. Specifically, I'd like to thank Lydia. You became my unforeseen lab blessing

that made the hardest parts of research manageable. They say the best things come when you least expect it, and I am glad you came.

To Harold, Elizabeth, Carlos, and Aléyah, thank you for your constant love, support, and motivation. I would not be able to do this without my tribe.

To Linda, Luther, and Leslie, thank you for always answering my calls and telling me that I can do it.

Finally, a big, special thanks to my Mom and Dad. Nothing can surpass the sacrifices you made to ensure that I would have more opportunities than you did growing up. Thank you for your love and encouragement. Both of you were always there when I needed it the most, and I am incredibly grateful to have your support.

CONTRIBUTORS AND FUNDING SOURCES

Contributors

This work was supervised by a thesis committee consisting of Dr. Kamran Entesari and Dr. Arum Han of the Department of Electrical Engineering and Dr. Gerard L. Cote [chair] and Dr. Limei Tian of the Department of Biomedical Engineering.

All work conducted for the thesis was completed by the student independently under the advisement of Dr. Gerard Cote of the Department of Biomedical Engineering.

Funding Sources

This work was supported by the PATHS-UP ERC funded by the National Science Foundation [ERC-164851]. Its contents are solely the responsibility of the authors and do not necessarily represent the official views of the National Science Foundation or PATHS-UP.

NOMENCLATURE

CVDs	Cardiovascular Diseases
BP	Blood Pressure
HR	Heart Rate
PTT	Pulse Transit Time
BIO-Z	Bioimpedance
IPG	Impedance Plethysmography
POC	Point-of-Care
SBP	Systolic Blood Pressure
DBP	Diastolic Blood Pressure
MABP	Mean Arterial Blood Pressure
ABPM	Ambulatory Blood Pressure Monitoring
PWV	Pulse Wave Velocity
PAT	Pulse Arrival Time
ECG	Electrocardiogram
PEP	Pre-Ejection Period
PPG	Photoplethysmography
IPG	Impedance Plethysmography
SNR	Signal-to-Noise Ratio
BMI	Body Mass Index
FFM	Fat-Free Mass

LBM	Lean Body Mass
ICF	Intracellular Fluid
ECF	Extracellular Fluid
RC	Resistor-Capacitor
CPE	Constant Phase Element
BIA	Bioimpedance Analysis
BIS	Bioimpedance Spectroscopy
AFE	Analog Front-End
AC	Alternating Current
DC	Direct Current
DIA	Diastolic Peak Fiducial Point
SYS	Systolic Foot Fiducial Point
MS	Max Slope Fiducial Point
RMS	Root-Mean Square
INA	Instrumentation Amplifier
CMRR	Common-Mode Rejection Ratio
LIA	Lock-In Amplifier
LPF	Low Pass Filter
HPF	High Pass Filter
BPF	Band Pass Filter
DAQ	Data Acquisition Unit
PMIC	Power Management Integrated Circuit

MCU	Microcontroller
ADC	Analog-to-Digital Converter
IC	Integrated Circuit
SPI	Serial Peripheral Interface
HCP	Howland Current Pump
DMM	Digital Multimeter
AM	Amplitude Modulated
SMD	Surface Mount Device
EOR	Error Occurrence Ratio
PCB	Printed Circuit Board
ΔZ_p	Pulsatile Impedance
Z_b	Basal Impedance
ULOQ	Upper Limit of Quantification
BPM	Beats Per Minute
ASIC	Application-Specific Integrated Circuit

TABLE OF CONTENTS

	Page
ABSTRACT	ii
DEDICATION	iv
ACKNOWLEDGEMENTS	v
CONTRIBUTORS AND FUNDING SOURCES.....	vii
NOMENCLATURE.....	viii
TABLE OF CONTENTS	xi
LIST OF FIGURES.....	xiv
LIST OF TABLES	xvii
CHAPTER I INTRODUCTION	1
I.1 Motivation and Clinical Significance	1
I.2 POC Technologies for BP and HR Measurement.....	3
I.2.i Discrete, Cuffed-based Monitors	3
I.2.ii Continuous, Cuffless Monitors	4
I.3 Background	8
I.3.i Bioimpedance	8
CHAPTER II PROPOSED DEVICE: DUAL-IPG FOR CVD MONITORING	15
II.1 Impedance Plethysmography for HR and PTT.....	15
II.2 AFE Circuit Design: System Overview.....	18
II.3 AFE Circuit Design: Current Driving and Monitoring Circuit	20
II.3.i Waveform Generation and Signal Conditioning	20
II.3.ii Additional Signal Conditioning.....	22
II.3.iii Voltage-to-Current Conversion: Improved Howland Current Pump (HCP) with Buffer	23
II.3.iv Current Monitor.....	34
II.4 AFE Circuit Design: Voltage Sensing Circuit.....	42
I.4.i Instrumentation Amplifiers	42
I.4.ii Demodulation (LIA) and Low-Pass Filter	43

CHAPTER III FEASIBILITY STUDY WITH PROTOTYPE DEVICE	50
III.1 Introduction: Design of Experiment.....	50
III.2 Feasibility Study: Materials	51
III.2.i Feasibility Study: Custom Prototype Device	51
III.2.ii Feasibility Study: Electrodes and Electrode Holder	52
III.2.iii Feasibility Study: Acquisition Units	53
III.2.iv Feasibility Study: Other	53
III.3 Feasibility Study: Methods.....	54
III.3.i Feasibility Study: Initial and Final HR Measurement.....	54
III.3.ii Feasibility Study: Electrode Placement and Arrangement.....	54
III.3.iii Feasibility Study: Device and Acquisition Parameters for Dual IPG Acquisition	55
III.3.iv Feasibility Study: Dual-IPG Signal Processing and Data Analysis for HR and PTT	56
III.3.v Feasibility Study: Statistical Analysis	62
III.4 Feasibility Study: Results and Discussion	63
III.4.i Feasibility Study: Error Ratio	63
III.4.ii Feasibility Study: HR and PTT Detection	64
III.5 Chapter Summary and Conclusions	66
 CHAPTER IV PERFORMANCE CHARACTERIZATION OF FINAL AFE HARDWARE.....	 67
IV.1 Introduction: Design of Experiments	67
IV.2 Preliminary Study 1: Loading Limits of Current Source	68
IV.2.i Preliminary Study 1: Overview.....	68
IV.2.ii Preliminary Study 1: Materials and Methods	69
IV.2.iii Preliminary Study 1: Results and Discussion	71
IV.3 Preliminary Study 2: Current Monitor Accuracy and Feedback Loop	72
IV.3.i Preliminary Study 2: Overview.....	72
IV.3.ii Preliminary Study 2: Materials and Methods	73
IV.3.iii Preliminary Study 2: Results and Discussion	75
IV.4 Preliminary Study 3: Calibration	80
IV.4.i Preliminary Study 3: Overview.....	80
IV.4.ii Preliminary Study 3: Materials and Methods	81
IV.4.iii Preliminary Study 2: Results and Discussion	84
IV.5 In Vivo Study	88
IV.5.i In Vivo Study: Overview	88
IV.5.ii In Vivo Study: Materials and Methods	88
IV.5.iii In Vivo Study: Results and Discussion.....	93
IV.6 Cost of Goods.....	98
IV.7 Chapter Summary and Conclusions.....	100

CHAPTER V CONCLUSIONS	102
REFERENCES	105
APPENDIX A IN VIVO STUDY DATA.....	111
APPENDIX B MATLAB CODE FOR DUAL-IPG SIGNAL PROCESSING, FEATURE EXTRACTION, AND BASELINE/PULSATILE IMPEDANCE ACQUISITION	113

LIST OF FIGURES

	Page
Figure 1. Electrode Placement for Bipolar and Tetrapolar Configurations	9
Figure 2. Equivalent Circuit for the Bipolar and Tetrapolar Electrode Configuration	10
Figure 3. The Cellular Pathway of Current flow at Low and High Frequencies	12
Figure 4. Single-Dispersion Cole-Model.	13
Figure 5. BIO-Z Measurement Along Artery of Biological Medium	15
Figure 6. IPG Resistor Model	16
Figure 7. IPG Measurement and Translation to IPG Waveform.....	17
Figure 8. Dual-IPG Measurement and Translation to PTT	18
Figure 9. Functional Block Diagram for Dual-IPG Device	20
Figure 10. Phase v. Time Relationship for a Sine Wave.....	21
Figure 11. Schematic of Waveform Generation and Signal Conditioning Stages	22
Figure 12. HCP Topology	24
Figure 13. Improved HCP Topology.....	26
Figure 14. Improved HCP with a Buffer Topology	29
Figure 15. Current Adjusting Segment	33
Figure 16. Functional Diagram for RMS-to-DC Technology.....	37
Figure 17. Continuous Current Monitoring Arrangement.	40
Figure 18. Code Flowchart for the Auto-Shutdown Feature.....	41
Figure 19. Current Driving and Monitoring Schematic	42
Figure 20. Lock-in Amplifier Response to AM Input.....	46
Figure 21. AM Signal with Noise	46

Figure 22. Filtering AM Signal + Noise with an Ideal BPF	47
Figure 23. Schematic of Voltage Sensing Network	49
Figure 24. Custom Prototype Device	51
Figure 25. Dry Electrodes on Electrode-Holder Interface	52
Figure 26. Electrode Interface Connected to Cobbler Board.	53
Figure 27. Proximal and Distal Locations for Dual-IPG Acquisition.....	54
Figure 28. Signal Processing: Filtering Stage	56
Figure 29. Signal Processing: Envelope Removal	58
Figure 30. Signal Processing: Feature Extraction	59
Figure 31. Occurrences of Negative PTT.....	61
Figure 32. PTT Error Occurrence Over Time	61
Figure 33. Feasibility Study: Within Trial EOR. a) BIOPAC: EOR by Trial. b) Custom: EOR by Trial.	63
Figure 34. Feasibility Study: Between Trial EOR	63
Figure 35. Feasibility Study Within Trial HR and PTT. a) BIOPAC: HR by Trial. b) Custom: HR by Trial. c) BIOPAC: PTT by Trial. d) CUSTOM: PTT by Trial.....	64
Figure 36. Feasibility Study Between Trial HR and PTT. a) PTT Comparison Between BIOPAC and Custom. b) HR Comparison Between BIOPAC and Custom.	64
Figure 37. Dual-IPG PCB	67
Figure 38. Preliminary Study 1: Schematic Diagram for ULOQ Study	70
Figure 39. Preliminary Study 1: Average RMS Current v. Load Resistance.....	71
Figure 40. Preliminary Study 2: Schematic Diagram for Current Accuracy Study	73
Figure 41. Preliminary Study 2.i: Correlation of Measured Current with Resistor Load	75
Figure 42. Preliminary Study 2.ii: Correlation of Measured Current with BIO-Z.....	77

Figure 43. Preliminary Study 2.iii: Functionality Test for Automatic Shutdown Feature	79
Figure 44. Preliminary Study 3.i: Schematic Diagram for Obtaining Calibration Curves	81
Figure 45. Preliminary Study 3.ii: Schematic Diagram for Calibration Method Validation	82
Figure 46. Preliminary Study 2.i: IPG Calibration Curves	84
Figure 47. Preliminary Study 2.i: Standard Deviation of Measured Voltage v. Load	85
Figure 48. Preliminary Study 2.ii Measured Impedance of LCR and Calibrated Device v. Theoretical Impedance	86
Figure 49. Preliminary Study 2.ii: Calibrated Device v. LCR Meter Measured Impedance.....	86
Figure 50. In Vivo Study: Wet Electrode Placement	89
Figure 51. In Vivo Study: Feature Identification of SYS, DIA, and MS	90
Figure 52. In Vivo Study: Error Compensation	92
Figure 53. In Vivo Study: Detect PTT by Fiducial Point Per Subject	93
Figure 54. In Vivo Study: Average HR and PTT. a) Average Detected HR by Subject. b) Average Detected PTT by Subject.	94
Figure 55. In Vivo Study: Basal Impedance v. Location	95
Figure 56. In Vivo Study: Pulsatile Impedance v. Location	96
Figure 57. In Vivo Study: Measured Impedance by Sex. a) Average Basal Impedance by Sex. b) Average Pulsatile Impedance by Sex	97

LIST OF TABLES

	Page
Table 1. Advantages and Disadvantages of HCP Configurations.....	31
Table 2. Accuracy of RMS Estimation Methods	39
Table 3. Device and Acquisition Settings for Feasibility Study	56
Table 4. Feasibility Study: Between Trial PTT of BIOPAC and Prototype	65
Table 5. Feasibility Study: Between Trial HR of BIOPAC and Prototype.....	65
Table 6. Preliminary Study 1: Estimated ULOQ Load of Current Source	72
Table 7. Preliminary Study 2.i: Accuracy of Current Detector with Resistor Load	76
Table 8. Preliminary Study 2.ii: Accuracy of Current Detector with BIO-Z Load.....	78
Table 9. Preliminary Study 2.iii: Summary of Digital Response to PMIC.....	79
Table 10. Preliminary Study 3.ii: Calibration Validation Component Values.....	83
Table 11. Preliminary Study 2.i: Calibration Curve Equations.....	84
Table 12. Preliminary Study 2.ii: Measured Impedance of LCR Meter and Calibrated Device	87
Table 13. In Vivo Study: Device and Acquisition Settings	89
Table 14. Cost of AFE Components	98
Table 15. In Vivo Study: Detected PTT from MS, DIA, and SYS Fiducial Points.....	111
Table 16. In Vivo Study: Detected HR and Applied Current	111
Table 17. In Vivo Study: Measured Basal and Pulsatile Impedance at the Proximal Electrode Pair.....	111
Table 18. In Vivo Study: Measured Basal and Pulsatile Impedance at the Distal Electrode Pair.....	112

CHAPTER I

INTRODUCTION

I.1 Motivation and Clinical Significance

CVDs continues to prevail in the United States where an estimated 82.6 million people were reported to have one or more forms of CVD in 2010 [1]. On a global perspective, CVDs are the number one cause of death and are responsible for about 17.9 million deaths annually [2]. The most common pathogenesis for CVDs is atherosclerosis, which is arterial narrowing by plaque buildup [3]. Hypertension, or high blood pressure (BP), in an atherosclerotic environment enables a positive feedback loop for further buildup of plaque in a blood vessel, which can lead to the development of CVDs if experienced long-term [3]. For these reasons, hypertension is commonly known as the “silent-killer” because the medical condition displays little-to-no symptoms, but is capable of inducing fatal CVD-related events [4]. Without fully understanding the harm of encountering CVD risk factors long-term, specifically hypertension, most people who have a form of CVD are unaware of their prognosis until experiencing life-threatening symptoms. For instance, 20% of chronic hypertension remains undiagnosed [5]. Additionally, undiagnosed CVDs account for 20-40% of heart attacks [5].

CVDs and their risk factors are typically diagnosed in a clinical setting by a series of blood tests, imaging scans, and/or health monitoring systems (i.e., electrocardiogram, or echocardiogram) [6]; however, access to these technologies is not available to all. Out of the 17.9 million deaths that happen worldwide, low- and middle-

income countries are affected the most by CVDS, making up 75% of global CVD-related deaths [2]. Those who experience CVD risk factors and/or symptoms in these areas, have less access to healthcare programs that provide the technology for early detection and treatment [2]. Although access to healthcare is largely dependent on income, overall health status depends on two individual, but sometimes related, factors: socioeconomic status and ethnicity [7-9]. Statistics show underserved populations, which are socially marginalized, are at an increased risk of developing cardiovascular diseases in the US [7]. Similarly, Black and Mexican Americans are highly susceptible to CVDs due to elevated rates of hypertension and diabetes, respectively, when compared to rates seen in white American populations [7-9]. Therefore, there is a need to reduce CVD mortality rates in high-risk communities by proactive, community-based interventions.

Studies suggest BP management as a viable option for mitigating the development of CVDs in vulnerable populations [10]. Clinical trials have shown a reduction in CVD events by a minimum of 17% for every 10 mmHg decrease in systolic BP [11]. Monitoring of BP levels can result in lifestyle adjustments that lower the risk of hypertension and prevent the occurrence of CVD-related events. Although hypertension, is one of the main risk factors of CVD, the role of tachycardia, or increased heart rate, cannot be overlooked or underestimated as an independent risk factor as well [12]. A resting heart rate above 80-85 beats per minute (BPM) is directly correlated to the development of hypertension and atherosclerosis where both conditions promote the occurrence of CVD-related events [12, 13]. Continuously monitoring BP, in combination with HR, is an improved solution for predicting the onset of CVD; however, this

category of monitoring requires point-of-care (POC) technology that is compact, portable, noninvasive and cost-effective to reach underserved and underrepresented populations.

I.2 POC Technologies for BP and HR Measurement

I.2.i Discrete, Cuffed-based Monitors

For decades, physicians revolved around the mercury sphygmomanometer in combination with auscultatory-based references for noninvasive, in-office BP measurement. This method utilizes an inflatable cuff that wraps around the upper arm and a manometer to measure the air pressure in the cuff. The cuff is then inflated until blood flow is blocked in the brachial artery and then slowly deflated. During deflation, the systolic blood pressure (SBP) and diastolic blood pressure (DBP) are identified using the pressure measured when the sound of the artery arises (SBP) and leaves (DBP) [14]. These instances are most commonly known as Korotkoff sounds I and V and require training to properly distinguish [14].

While the auscultatory BP method dominated the industry in the twentieth century as the first noninvasive BP technique, it has recently been replaced by the oscillometric method for automated BP measurement at the hospital and home [15]. This technology is the most common POC device for BP measurement and is similar to the auscultatory approach; however, rather than using sound, the system uses the small oscillatory changes in pressure that occur during deflation due to pulsatile blood flow in the brachial artery [16]. The detection and analysis of the pressure waveform is electronically captured and analyzed. As the amplitude of these pressure oscillations

vary during the deflation period, the mean arterial blood pressure (MABP) is identified at the pressure where the oscillation amplitude is the largest. The SBP and DBP is then estimated using the MABP and a version of the fixed-ratio method [16].

An in-office hypertension diagnosis typically requires an evaluation of multiple BP measurements over 1-4 week intervals [17]. Although oscillatory BP monitors allow for automated and at-home measurement, this type of device can only acquire discrete measurements, which requires the user to remember to take measurements on a regular basis. To mitigate reliance on user compliance, ambulatory blood pressure monitoring (ABPM), which is a long-term application of the oscillometric BP monitor, has been introduced as the gold standard for noninvasive hypertension diagnosis [18].

ABPM automatically captures BP in 15-30 minute intervals over a 24-hour time period. While ABPM is the most common method for out-of-office hypertension diagnosis, these cuff-based devices are bulky, uncomfortable, and still require user compliance for monitoring chronic hypertension (> 24 hours) [10]. For these reasons, the research community is investigating passive approaches like cuffless BP monitoring.

1.2.ii Continuous, Cuffless Monitors

One method of cuffless BP monitoring uses pulse wave velocity (PWV), the propagation velocity of an arterial pulse wave, to estimate blood pressure through theoretical equations like Bramwell–Hill and Moens–Korteweg [19]. PWV can be calculated by pulse transit time (PTT), the time it takes for a pulse wave to travel between two arterial sites, and/or pulse arrival time (PAT) detection, the time it takes for a pulse to arrive at an arterial site [19, 20]. For PAT-based BP monitoring, a

combination of electrical measurement of the pulse wave activity, typically via electrocardiogram (ECG) for the reference time, and mechanical measurement of the pulse wave activity, from waveforms like photoplethysmography for pulse arrival, is required. While PTT can be obtained similarly to PAT with an electrical-mechanical measurement configuration, the minimal requirement is the detection of mechanical activity at two arterial sites [19].

There are a few downfalls with PAT/PTT-based BP monitoring due to the inclusion of ECG. The electrical-mechanical measurement of PAT uses the R-peak of the ECG waveform as the initial time reference for pulse arrival. The pre-ejection period (PEP) between the onset of the R-peak and the pumping of the blood from the left ventricle into the aorta results in a time delay. Therefore, PAT quantifies the sum of PTT and PEP. The inclusion of PEP adds a source of error because of its variability and unpredictability [21]. Although the electrical measurement of ECG is more motion-tolerant, there are also physical limitations to the modality that make it difficult to conform to a small, wearable form factor. The lead configuration for the acquisition of quality ECG signals typically needs to be across the heart via chest patch. Alternatively, for wrist wearables that include ECG measurements, the patient is required to use a finger from the opposing arm to touch an exposed electrode pad on the device to complete the circuit, which completely eliminates hand function during data acquisition and any hope of continuous monitoring. To avoid these complications for PTT detection, modalities that measure mechanical pulse wave activity like photoplethysmography

(PPG), high-sensitive pressure transducers, and impedance plethysmography (IPG) are being developed.

Even though all mechanical pulse wave modalities are susceptible to motion artifacts, there are a few features that make IPG more favorable for continuous health monitoring in comparison to PPG or pressure transducers. While PPG is a well-known, low-cost modality used for heart rate monitoring and, when multiple wavelengths are employed, can be used to monitor pulse-oximetry in clinical settings, the use of the optical sensor for pulse wave detection encounters design challenges when evaluating subjects with different skin pigmentations and body masses [22, 23]. Most PPG sensors for heart rate monitoring can use one wavelength but for pulse oximetry, a combination of 2 or 3 different wavelengths of light are required such as: green (495-570 nm), red (620-750 nm), and IR (780-1000 nm) [24-27]. Longer wavelengths in the red or IR range are advantageous when including various skin pigmentations and body masses because of the reduced light absorption and scattering from the tissue components such as elastin, collagen, and melanin and subcutaneous lipids [28, 29]. This allows for deeper penetration of the light to reach the arteries or arterioles; however, the effects of skin thickness are still prevalent where a predicted 40% loss in light amplitude can be contributed to obesity [30]. Green light has traditionally been used because of its high absorptivity by hemoglobin in red blood cells [31]. This trait allows for a greater sensitivity to blood volume changes; however, its short wavelength exhibits shallow penetration and increased absorption by melanin from darker skin tones, which makes it difficult for the light to reach vascular regions [32]. In contrast, IPG is able to reach

deeper tissue regions because it does not have the absorption limitations from light for detection and instead uses high frequency current [33]. Using an electrical flow transmitter instead of light also removes ambient light as source of error seen with PPG acquisition [19].

In terms of pressure sensors (piezoresistive, capacitive, piezoelectric, etc.) the material and fabrication of each transducer type corresponds to its own set of challenges. Piezoresistive sensors struggle with hysteresis due to deformation of the porous structures in the active layer over time [34]. Capacitive-based sensors are highly affected by parasitic capacitances and low pressure sensitivity depending on the type of dielectric material [35]. Piezoelectric sensors are created using hard inorganic materials which are susceptible to low pulse wave signal-to-noise ratio (SNR) due to conformity issues [34]. A method to combat these issues includes detection in a semi-occlusive environment; however, this poses an additional constraint for its wearable format [33]. Bioimpedance-based sensors overcome the limitations faced by pressure transducers by allowing for the potential for cuffless measurement and conformability to a wearable format.

To date, there are no wearable devices that are commercially available for cuffless BP monitoring [36]. In July of 2022, LiveMetric's smartwatch device was the first to receive FDA clearance by 510k for a compact device that detects BP every 10 seconds; however, this smartwatch is not available for individual sale and uses an array of pressure sensors rather than bioimpedance [37]. The use of a dual-IPG sensor composed of low-cost components offers the possibility of accessible, noninvasive cuffless-BP monitoring in high-risk communities and underserved and underrepresented

populations. Therefore, it is important to design, develop, and validate robust hardware that can be used for these purposes.

I.3 Background

I.3.i Bioimpedance

I.3.i.a Definition

Bioimpedance (BIO-Z) is a measurement method that is used to quantify the physiological response to an externally applied electrical stimulus [38]. This method measures tissue resistance to electrical flow by utilizing an alternating current (AC) source with electrodes to drive the stimulus and sense the response of the biological medium. The mathematical extrapolation of BIO-Z can be described by Ohm's law where the impedance (Z) of a biological medium is equivalent to the tissues voltage response (V) divided by the current injected into the system (I). Due to the conductive and dielectric properties of tissue, BIO-Z is complex with both a magnitude and phase. Equation 1 expresses BIO-Z equation in its complex form.

Equation 1.

$$Z \angle \theta = \frac{V \angle \theta}{I \angle \theta}$$

To date, BIO-Z has been used to characterize blood flow and a number of body composition parameters including, but not limited to, body mass index (BMI), hydration/body fluid, and fat-free mass (FFM) or lean body mass (LBM) [39]. For most impedance-based biosensors with a cardiovascular application, the injection current is a sinusoidal signal at a set frequency between the range of 10 kHz and 250 kHz [40-42]. The frequency of the injection current resides in this range to allow current to pass

through the whole system containing the extracellular fluid (ECF), intracellular fluid (ICF), and cell membrane [39]. This phenomenon is the foundation for the deep region detection qualities of bioimpedance-based modalities.

I.3.i.b Electrode Placement

BIO-Z can be acquired in a bipolar or tetrapolar configuration. A bipolar arrangement consists of two electrodes that both inject the current and measure the voltage response. Alternatively, the tetrapolar configuration utilizes four electrodes where a pair of electrodes transmit the alternative current and the remaining pair receive the tissue response via voltage measurements. Figure 1 displays the difference in electrode placement between both layouts.

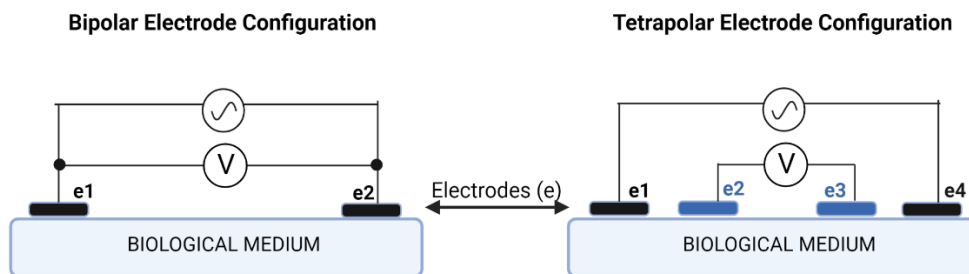


Figure 1. Electrode Placement for Bipolar and Tetrapolar Configurations [Created with BioRender.com]

Due to local polarization at the electrode-skin interface, an additional contact impedance is introduced into the system [38, 43]. The contact impedance of the electrode plays a significant role in the choice of electrode configuration. For a bipolar electrode placement, the contact impedance is in series with the impedance of the sample, causing the measured voltage response to include the impedance of the

electrode-skin interface and the tissue. Alternatively, measurement from a tetrapolar configuration isolates the voltage response from solely the sample because current is being passed through a separate pair of electrodes. Figure 2 displays this difference with the equivalent circuits for the bipolar and tetrapolar layout.

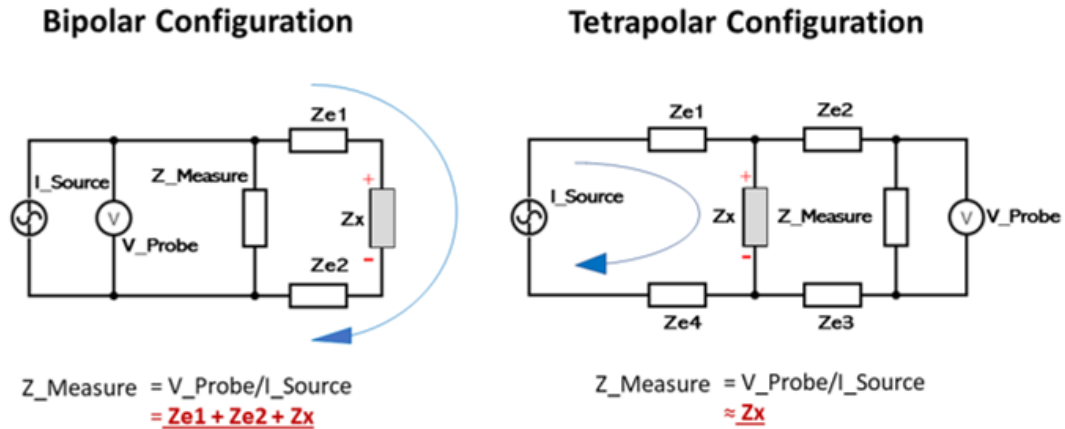


Figure 2. Equivalent Circuit for the Bipolar and Tetrapolar Electrode Configuration

At frequencies below 1 kHz, the impedance of the electrode-skin interface ($< M\Omega$) dominates in comparison to the impedance of the tissue ($< k\Omega$) [44, 45]. Even so, at frequencies higher greater than 1 kHz, the influence of contact impedance is not small enough to exclude [44, 45]. Therefore, detecting minor variations in BIO-Z is unrealistic in a bipolar arrangement [44]. The displacement of BIO-Z due to cardiac activity typically maxes out at 0.1Ω ; thus, a tetrapolar configuration is preferred because the detection method minimizes the influence of the electrode contact impedance and allows for sensitive monitoring of cardiovascular health [46, 47].

I.3.i.c Current Flow and RC Model for a Biological Medium

The electrical flow through a biological medium is impacted by chemical and electrical factors [48]. There are two passive components that are commonly used to model biological mediums: resistors and capacitors. The conductivity of a biological medium reflects the resistance of the BIO-Z model where the ions in a biological medium transport electrical current [48]. Both conductivity and resistance of a biological medium share a relationship with the dissolved ion concentration. An increase in ion concentration increases the conductivity and decreases the resistance of the medium. Electrolyte solutions (blood, sweat, interstitial fluid, etc.) and soft tissues mainly contribute to the resistance of the body because of their high conductivity properties [48]. Additionally, other factors like temperature, viscosity, and the distance between measuring electrodes impact the conductivity and electrical resistance. In terms of capacitance, a biological medium displays dielectric properties due to the permittivity of tissue. Permittivity is the tissue's ability to store energy when impacted by an electric field [48]. The permittivity of a biological medium varies based on tissue type (skin, fat, muscle) and injection frequency.

The analysis of biological mediums focuses on the characterization of its conductive and dielectric properties. For BIO-Z models, a local cellular analysis is used to formulate resistor-capacitor (RC) models [48]. These models consider the ICF, ECF, and the membrane of cell. Due to the ions in the electrolytic solutions of the ICF and ECF, both compartments are conductive and contribute to the resistance of a biological medium; however, the membrane that separates these compartments acts as a dielectric

[48]. This type of functionality can be represented by a capacitor, where the cell membrane is the dielectric material and the fluid in the intracellular and extracellular compartments are the plates [48]. As a result, BIO-Z is complex and frequency dependent because of the method of current flow. At low frequencies, current flows around the cells; however, at higher frequencies current can penetrate the ICF in a biological medium. Figure 3 shows this alternative pathway of current flow at low and high frequencies.

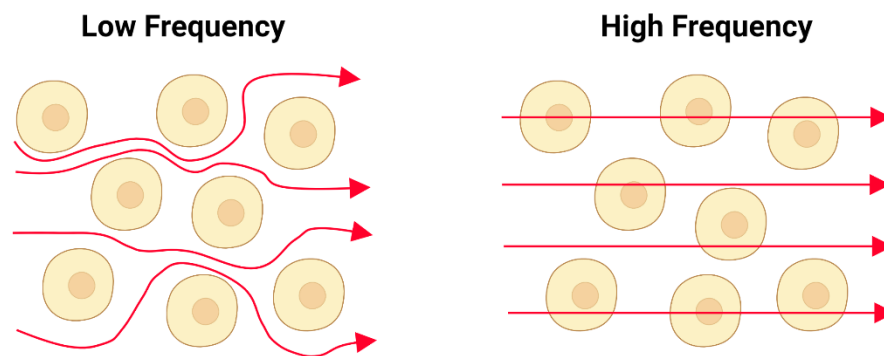


Figure 3. The Cellular Pathway of Current flow at Low and High Frequencies
[Created with BioRender.com]

Although there are a number of RC models that have been proposed as an equivalent to this behavior, the most common and simplest BIO-Z model is the single-dispersion Cole model, which consists of two resistors and a constant phase element (CPE) capacitor [48].

Figure 4 displays the single-dispersion Cole model for a biological medium.

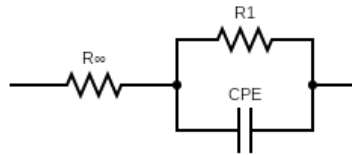


Figure 4. Single-Dispersion Cole-Model.

By taking advantage of how chemical and electrical properties vary by tissue type, BIO-Z is used to characterize body composition with single measurements at one or multiple frequencies. For example, total body water is estimated using a combination of two procedures: bioimpedance analysis (BIA) and bioimpedance spectroscopy (BIS). BIA captures the BIO-Z at a single frequency and maps that value to the volume of the subject's extracellular fluid. As mentioned, as the amount of body fluid increases, the biological medium becomes more conductive, resulting in a lower BIO-Z. However, as measurements can vary subject-to-subject, the use of BIS mitigates these discrepancies by collecting BIO-Z measurements at multiple frequencies rather than one. With more careful consideration of the permittivity and dielectric properties of skin, fat, and muscle, this same methodology is also applied for FFM, LBM, and BMI estimation.

I.3.i.d Limitations

Despite the increased penetration depth for BIO-Z devices, there are disadvantages to the sensing modality that should be considered for the system's circuit design and signal processing. Physiological noise obtained from the body is a

dominating and unavoidable contributor to the corruption of the IPG signal [49]. Intrinsic body noise includes, but is not limited to, muscle activity, parasitic capacitances between the body and earth, anisotropic properties of tissue resulting in the modification of current flow along a longitudinal axis, and skin polarization at the electrode-skin interface [49, 50]. Additionally, power line noise (60Hz/50Hz) is experienced at a greater extent due to the capacitive coupling at the electrode leads and skin-electrode interface [51]. Although internal noises play a significant role in signal quality, the electrode type and placement also contribute to the SNR [52]. The contact noise at the electrode-skin interface varies depending on the electrode category: dry or wet electrodes [51]. A tetrapolar configuration helps mitigate the electrode influence during measurement; however, the electrode effects are still prominent. Therefore, there is a need for the development of a robust, analog front-end (AFE) for a bioimpedance-based sensor that continuously monitors cardiovascular health despite noise interferences.

CHAPTER II

PROPOSED DEVICE: DUAL-IPG FOR CVD MONITORING

II.1 Impedance Plethysmography for HR and PTT

Rather than a single measurement of BIO-Z, which is performed for BIA and BIS procedures, IPG is the continuous measurement of BIO-Z over a period of time. When the electrode unit is placed near the artery in a tetrapolar configuration, IPG acquisition is optimal for the monitoring of cardiac activity. Figure 5 shows the measurement of BIO-Z as blood travels through the artery.

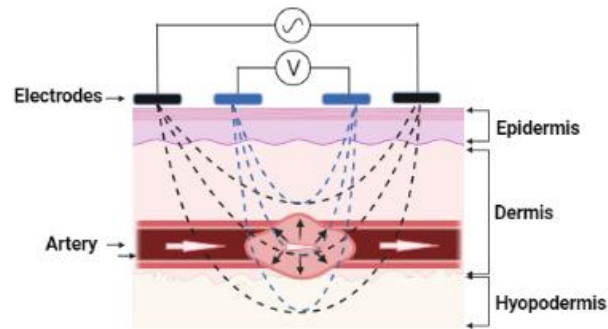


Figure 5. BIO-Z Measurement Along Artery of Biological Medium
[Created with BioRender.com]

The major benefit of the tetrapolar arrangement is the ability to exclude the phase component of BIO-Z for pulse-wave activity. Due to the four-electrode configuration eliminating the impact of the electrode-skin interface and isolating the voltage response from the tissue, the conductivity fluctuations from blood flow translates to variations in BIO-Z that is primarily resistive at static frequencies between 1 kHz – 100 kHz [46, 47, 53, 54]. When measuring this change over time, previous studies have shown a small

contribution from the phase component (up to 12 degrees), while the real component of the IPG signal contains 96% of the information of the complex quantity [47, 53]. Hence, the phase component may be neglected for IPG measurement in the 1 kHz -100 kHz frequency range and the single-dispersion Cole model can be simplified down to two resistors when analyzing pulse wave activity. With this model, one resistor represents the basal impedance of the sample, while the other resistor describes the variation in impedance from pulsatile blood flow. Figure 6 shows the resulting resistive model for IPG.

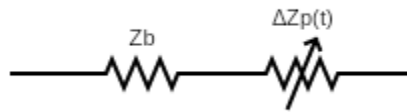


Figure 6. IPG Resistor Model

The IPG waveform, $Z(t)$, consists of two periodic components: (1) a pulsatile or AC component and (2) a non-pulsatile or direct current (DC) component. The pulsatile component (0.5-5 Hz) of an IPG signal corresponds to volume changes in the arteries caused by systolic and diastolic cardiac activity, $\Delta Z_p(t)$. As blood pumps throughout the cardiovascular system, the arterial blood volume varies, resulting in pulsatile fluctuations in BIO-Z. During the systolic phase, a large influx of blood runs through the system. Because fluid is less resistant to electrical flow, a low impedance is measured during this phase [55]. Contrarily, during the diastolic phase, there is less fluid in comparison, resulting in higher impedance measurements. The non-pulsatile component,

which derives from a combination of stationary components, like tissue, venous blood, and non-pulsatile arterial blood, is described as the basal impedance, Z_b . The basal impedance is an average impedance of the physiological components described above [53]. Figure 7 expresses the basal impedance as fixed for simplification; however, over periods of time, this value can fluctuate at very low frequencies (0.14-0.9 Hz), for example, due to respiration.

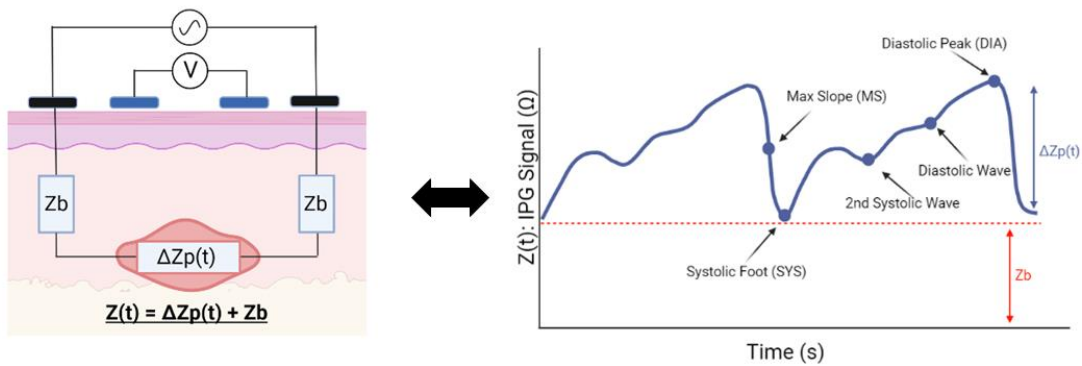


Figure 7. IPG Measurement and Translation to IPG Waveform
[Created with BioRender.com]

Generally, most cardiovascular information is collected from the fiducial points of the pulsatile, AC component of the IPG signal. The diastolic peak (DIA) is the highest point of an IPG signal and represents both the end of the diastolic phase and the onset of the systolic phase. The systolic foot (SYS) is the lowest point of the IPG waveform and accounts for the decrease in resistance as blood is pumped from the left ventricle. The second systolic wave is formed by the reflection of the blood in the vascular bed and the diastolic wave represents the onset of the diastolic phase [56]. Lastly, the max slope point (MS) characterizes the moment of maximum impedance change. By plotting the

derivative of the IPG signal, the MS point can clearly be identified. The frequency of these points in a given time period represents heart rate. When two adjacent IPG sensors are placed on the radial artery, these critical points can also be used to detect PTT. Using a six-electrode configuration, the time delay between the critical points of the two IPG signals corresponds to the pulse transit time. Figure 8 displays dual-IPG acquisition and the corresponding waveforms for PTT detection. The systolic foot of the IPG signal and the max slope point from its derivative are the best to use for PTT detection because of its consistency throughout acquisition.

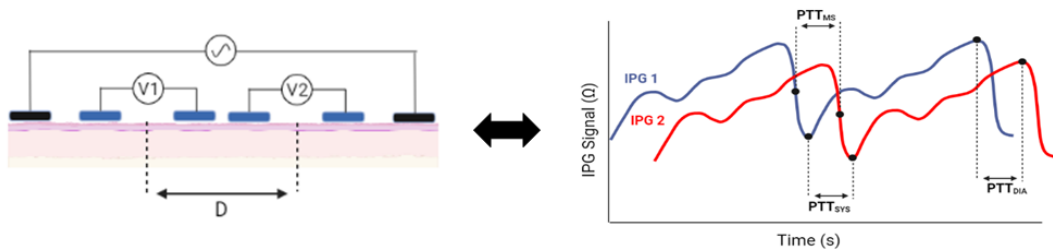


Figure 8. Dual-IPG Measurement and Translation to PTT
[Created with BioRender.com]

II.2 AFE Circuit Design: System Overview

The AFE of the bioimpedance-based device contains three main subsystems for dual-IPG acquisition and current monitoring: the current driving network, the voltage measuring network, and the current detection network. The current driving network generates a low magnitude, sinusoidal current with a programmable frequency and magnitude set by the user. This unit also provides the carrier signal for the demodulation performed in the voltage sensing network.

The output of the current source is passed through a shunt resistor and then applied to the subject with the injection electrodes (I_+ , I_-). By utilizing the voltage drop across the shunt resistor, the current detection network converts the AC voltage to its equivalent root-mean square (RMS) value in the form of a DC signal.

To fulfill the design requirements for dual-IPG acquisition, the voltage sensing network contains two identical circuits for voltage measurement at the proximal and distal locations of the wrist along the radial artery. The voltage sensing electrodes ($V1_+$, $V1_-$, $V2_+$, $V2_-$) provide the tissue's response to the applied current to an instrumentation amplifier (INA) with a high common-mode rejection ratio (CMRR). The INA amplifies the weak signal for further amplitude demodulation by a lock-in amplifier (LIA). The signals are then passed through a lowpass filter (LPF) and sampled by a data acquisition unit (DAQ).

The AFE is provided with the necessary power supplies by an external power management integrated circuit (PMIC) that receives 5 V from the Arduino Uno R3 microcontroller (MCU) and outputs 3.3 V and ± 5 V power rails. One feature of the PMIC includes programmable shut-off via digital input from the MCU. To make use of this feature, the output of the current monitoring network is sent to both the DAQ and the analog-to-digital converter (ADC) of the MCU. In doing so, a feedback loop is maintained during signal acquisition and the power of the system can be shut down based on magnitude of the measured current.

All analog signals produced by the AFE are measured by National Instrument's NI USB-6003 DAQ, which allows for simultaneous sampling of up to four differential

analog signals at a 16-bit resolution. Figure 9 provides a functional block diagram for the entire system.

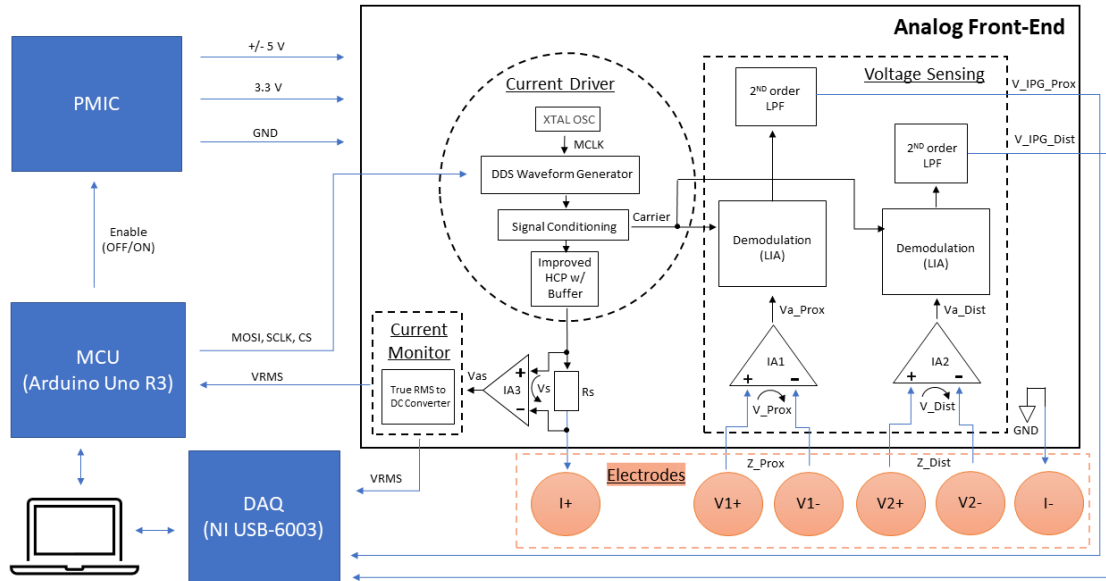


Figure 9. Functional Block Diagram for Dual-IPG Device

II.3 AFE Circuit Design: Current Driving and Monitoring Circuit

II.3.i Waveform Generation and Signal Conditioning

A sinusoidal voltage is generated by Analog Device’s DDS waveform generator, the AD9837ACP. This integrated circuit (IC) is a compact, low-power solution to producing accurate AC signals for wearable devices. It features a power consumption of 8.5 mW at 2.7 V supply and allows for a programmable frequency of up to 8 MHz using 3-wire serial peripheral interface (SPI) communication [57]. In comparison to the Wein Bridge oscillator, which is a simpler and more common approach to sine wave

generation, the AD9837 is favorable in the fact that it does not encounter distortion due to saturation, which is the main drawback from using a Wein Bridge oscillator [58].

Programmable waveform generation is achieved by sampling the sinusoidal, 16 MHz clock signal from the spread spectrum crystal oscillator (Mercury United Electronics, 3QHM53C0). The output frequency is calculated by making use of the linear relationship between the phase of the input sine wave and time. Figure 8 provides a visual of this linear dependency.

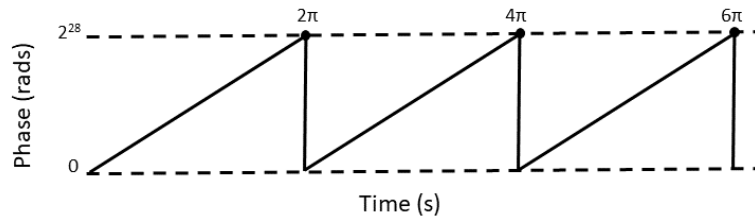


Figure 10. Phase v. Time Relationship for a Sine Wave

The change in phase for a given period is described by Equation 2:

$$\Delta Phase = \omega \Delta t$$

Equation 2.

By converting the angular frequency to linear frequency and replacing the reference period with the reference clock frequency ($\Delta t = 1/f_{MCLK}$), Equation 3 expresses the output frequency is below:

$$f_{out} = \frac{\Delta Phase \times f_{MCLK}}{2\pi}$$

Equation 3.

The implementation of this equation with the 28-bit frequency input provided by the user produces a 0.6 V_{p-p} sine wave at a resolution of 0.06 Hz and a 0.3 V DC offset

[57]. The output of the DDS then undergoes signal conditioning that shifts the DC offset to $V_{CC}/2$ and amplifies the sine wave to a peak-to-peak voltage of 1 V using a low noise, low distortion, and high slew rate operational amplifier (Analog Devices, AD8045ACP). Figure 11 displays the circuit for waveform generation and signal conditioning. This framework for this circuit was adapted from the SparkFun MiniGen shield.

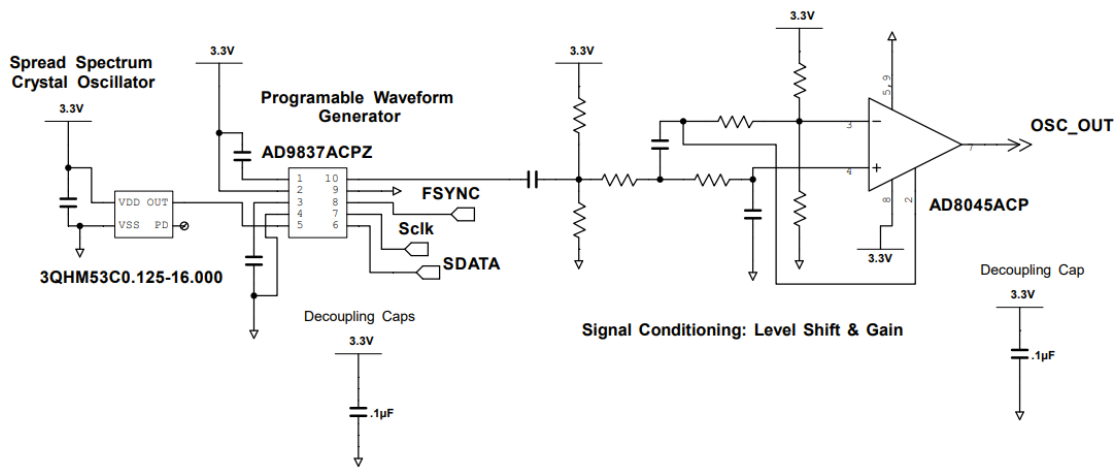


Figure 11. Schematic of Waveform Generation and Signal Conditioning Stages

It is important to note that although the AD9837ACP IC is capable of generating sinusoidal, triangular, and square wave signals, a sine wave is preferred because it allows for the use of signal processing methods that are straightforward. Alternative waveform types, like the square and triangular signals, introduce additional harmonics in the frequency domain that must be accounted for when resolving the IPG signal.

II.3.ii Additional Signal Conditioning

Due to the capacitive nature of the cell membrane, injecting a DC current is undesirable for an IPG application. Electrical stimuli at this frequency causes a build-up in charge at the electrode-skin interface that should be limited for electrical safety

purposes. Additionally, as mentioned previously, applying a DC current to a biological medium blocks conduction throughout the cell and neglects the ICF's contribution to BIO-Z. Therefore, following waveform generation, the sine wave is passed through a multiple-feedback bandpass filter (BPF) to remove the DC offset and any sideband ripples that are exhibited as images of the fundamental frequency during the Nyquist sampling performed by the DDS waveform generator [57]. The center frequency of the BPF has been set to roughly 17 kHz (16.932 kHz) with a bandwidth of 1.662 kHz. As you increase the injection frequency, the tissue-to-contact impedance ratio increases; thus, resulting in a larger contribution to the signal from the biological medium [45]. Due to this, there may be a need to inject different frequencies of current. Under those circumstances, this stage can be replaced with a high pass filter (HPF) that has a cut-off frequency of 1kHz or larger.

After filtering, the signal is used as the input for two operations: voltage-to-current conversion and demodulation via a LIA (Analog Devices, AD630).

II.3.iii Voltage-to-Current Conversion: Improved Howland Current Pump (HCP) with Buffer

I.3.iii.a The Basic HCP

There are two main goals to achieve when designing a current source for a BIO-Z application: 1) a high output impedance to avoid current draw by the source and 2) a large output voltage swing to have access to the entire range of the low power supplied to the system. With the aim of accomplishing these features, the basic HCP is used as the foundation for voltage-to-current conversion.

To understand the theory of operation, figure 12 displays the HCP with a single AC voltage input.

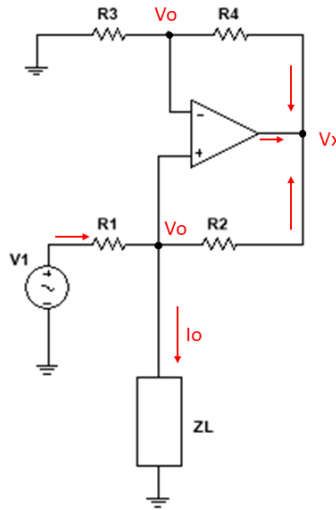


Figure 12. HCP Topology

For this configuration, the “output” is defined at the node with the load impedance (Z_L), which is the also the same node as the non-inverting input. Therefore, the voltage at both inputs of the op-amp is equivalent to the output voltage (V_o), as there is no potential difference between the inputs of an ideal op-amp.

Using KCL at both the inverting and non-inverting inputs, the following relationships shown in Equation 4 and Equation 5 are deduced.

$$V_x = V_o \left(1 + \frac{R_4}{R_3}\right) \quad \text{Equation 4.}$$

$$I_o = \frac{V_1 - V_o}{R_1} - \frac{V_o - V_x}{R_2} \quad \text{Equation 5.}$$

By substituting Equation 4 into Equation 5, the output current is expressed by Equation 6.

$$I_o = \frac{V_1}{R_1} + \frac{V_o}{R_o} \quad \text{where, } R_o = \frac{R_1 R_2 R_3}{R_1 R_4 - R_2 R_3} \quad \text{Equation 6.}$$

The influence of the output voltage on the output current can be eliminated by setting $R_1/R_2 = R_3/R_4$. In doing so, the resulting output impedance is infinite and the gain the output current is dependent on one resistor, R_1 as shown in Equation 7.

$$I_o = A * V_1 \quad \text{where, } A = \frac{1}{R_1} \quad \text{Equation 7.}$$

From the circuit analysis of the basic HCP, a high output impedance is demonstrated, but only when the resistors are almost perfectly matched. Therefore, for precision applications, it is important to use low tolerance resistors as the output impedance can drop down as low as 250 kΩ when all resistors are 10 kΩ at a 1% tolerance [59].

The major disadvantage of the basic HCP is the limited capabilities at the output which do not allow the voltage of the output node (V_o) to reach rail. For instance, if $R_1=R_2=R_3=R_4$, the voltage at the output node is limited to $V_x/2$ based on Equation 4. Thus, the output swing of the basic HCP can only reach half the supply voltage for this case scenario. Without having access to the entire rail at the output, low-power devices encounter challenges to drive enough current across larger loads like high impedance dry electrodes [59]. Due to this, the improved HCP should be adopted for more headroom.

I.3.iii.b The Improved HCP

The improved HCP allows for a greater output swing by splitting R_2 into two resistors, R_{2a} and R_{2b} , and relocating the output of the current source to the node between these two resistors. Figure 13 displays this change in topology.

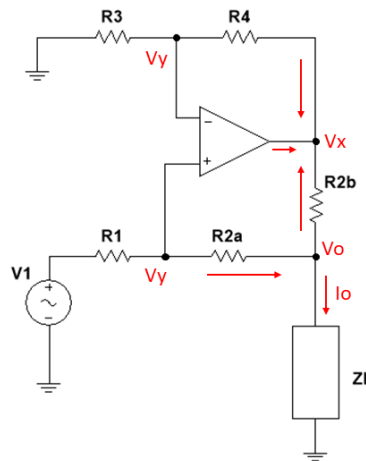


Figure 13. Improved HCP Topology

First, to understand how the voltage swing range is widened, the conditions for an infinite output impedance should be determined. By performing a circuit analysis for this configuration, Equation 8 expresses the output current for the improved HCP.

$$I_o = V_1 \left(\frac{\frac{R_3}{R_4}(R_{2b}+R_{2a})+R_{2a}}{\frac{R_3 R_{2b}}{R_4}(R_1+R_{2a})} \right) + \frac{V_o}{R_o} \quad \text{where,} \quad R_o = \frac{\frac{R_3 R_{2b}}{R_4} \left(\frac{R_1+R_{2a}}{R_{2b}+R_{2a}} \right)}{\frac{R_1}{R_{2b}+R_{2a}} - \frac{R_3}{R_4}} \quad \text{Equation 8.}$$

From Equation 8, an infinite output impedance is achieved when $R_3/R_4 = R_1/(R_{2b}+R_{2a})$. This condition is similar to that of the basic HCP where the sum of R_{2b} and R_{2a} replaces R_2 in the denominator. As a result of applying this condition to Equation 8, the influence of the output voltage is removed and the expression for the output current is simplified to Equation 9.

$$I_o = A * V_1 \quad \text{where,} \quad A = \frac{R_4}{R_3} * \frac{1}{R_{2b}} \quad \text{and} \quad \frac{R_3}{R_4} = \frac{R_1}{R_{2b}+R_{2a}} \quad \text{Equation 9.}$$

To meet this condition, the ratio between R_3 and R_4 is typically 1-to-1 and R_{2b} is set to a low value while R_1 and R_{2a} are high resistance (100 kΩ or 1 MΩ), which minimizes the influence of R_{2b} in the ratio. When this occurs, the current gain is primarily dependent on the resistance of R_{2b} .

After deriving the constraints for the improved HCP, the maximum voltage at the output can be determined by shorting the input voltage and performing a circuit analysis at the non-inverting and inverting nodes of the op-amp.

Equation 10 and Equation 11 display these relationships at each node respectively.

$$V_y = V_x \left(\frac{R_3}{R_3 + R_4} \right)$$

Equation 10.

$$V_0 = V_y \left(1 + \frac{R_{2a}}{R_1} \right)$$

Equation 11.

The expression for the voltage at the output node is deduced by substituting Equation 10 into Equation 11, resulting in Equation 12.

$$V_0 = V_x \left(1 + \frac{R_{2a}}{R_1} \right) \left(\frac{R_3}{R_3 + R_4} \right)$$

Equation 12.

For simplicity, we can make the assumption that $R_1 = R_{2a} = R_3 = R_4$. In doing so, Equation 12 reduces to $V_0 = V_x$ and the maximum voltage swing at the output is now equivalent to the power supply for this case.

Through the evaluation of the improved HCP topology, an expanded range in output swing and a high output impedance is exhibited when the conditions in Equation 9 are met. Similar to the basic HCP, the resistors should have a low tolerance for precision applications; however, the additional requirement of high resistant resistors (R_1 , R_{2a} , R_3 , and R_4) introduces more instability due to increased error when resistor matching and additional thermal noise to the system. These disadvantages are avoided in

the improved HCP with a buffer configuration, which adds a buffer to the output of the current source and removes the reliance on large resistors for a high output impedance.

I.3.iii.c Improved HCP with a Buffer

The improved HCP with a buffer displays the same benefits of the improved HCP without encountering more instability and thermal noise from high value resistors.

Figure 14 shows the schematic of the improved HCP with a buffer configuration.

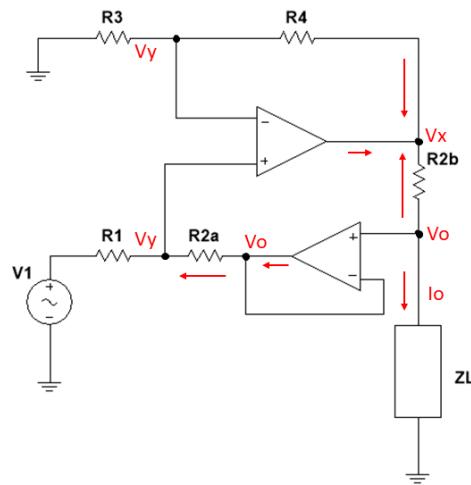


Figure 14. Improved HCP with a Buffer Topology

After performing a circuit analysis, the expression for the output impedance is shown in Equation 13.

Equation 13.

$$R_o = \frac{(R_1 + R_{2a}) \frac{R_3 R_{2b}}{R_4 R_{2a}}}{\frac{R_1}{R_{2a}} - \frac{R_3}{R_4}}$$

Now, the output impedance for this topology is infinite when $R_3/R_4 = R_1/R_{2a}$. By adding the buffer at the output of the current source, there is no longer a need for large

resistors or carefully choosing R_1 , R_{2a} , and R_{2b} to meet the tight constraints in Equation 9.

Other than possessing different conditions for an infinite output impedance, the performance of this source, in terms of output current and voltage swing, is analogous to the improved HCP. Equation 14 provides the expression for the output current, which is the same as that of the improved HCP and can be easily adjusted by varying one resistor, R_{2b} . Additionally, the expression for the output voltage is the same as Equation 12; thus, the efficiency of the output is also equivalent to the improved HCP.

Equation 14.

$$I_o = A * V_1 \quad \text{where,} \quad A = \frac{R_4}{R_3} * \frac{1}{R_{2b}} \quad \text{and} \quad \frac{R_3}{R_4} = \frac{R_1}{R_{2a}}$$

While the improved HCP with a buffer embodies all the positive features of the basic and improved HCP, there is still one downfall in its design that is relevant to the design of a wearable device: the need for a second op-amp. Adding another active component increases the cost, size, and power consumption of the system. Fortunately, there are many low-power, low-cost precision op-amps that come in a dual-channel configuration for compact applications [60]. By utilizing these types of op-amps, the weaknesses that come from the including an additional active component are miniscule in comparison to the drawbacks of the basic and improved HCP configurations.

Table 1 provides an overall summary of the advantages and disadvantages that have been discussed in this section for each topology.

Table 1. Advantages and Disadvantages of HCP Configurations

	Basic HCP	Improved HCP	Improved HCP with a Buffer
Advantages	<ul style="list-style-type: none"> - One resistor current gain adjustment - One active component <ul style="list-style-type: none"> - High output impedance when conditions met - Lower thermal noise and instability due to smaller resistors 	<ul style="list-style-type: none"> - One resistor current gain adjustment - Wide voltage output swing - One active component <ul style="list-style-type: none"> - High output impedance when conditions met 	<ul style="list-style-type: none"> - One resistor current gain adjustment - Wide voltage output swing - High output impedance when conditions met - Lower thermal noise and instability due to smaller resistors
Disadvantages	<ul style="list-style-type: none"> - Low output swing 	<ul style="list-style-type: none"> - High thermal noise and instability due to large resistors 	<ul style="list-style-type: none"> - 2 active components

Based off the in-depth analysis of each arrangement, the voltage-to-current conversion for the current driving network consists of the improved HCP with a buffer, where the voltage input, V_1 is an amplified version of the waveform generation and signal conditioning stages. The improved HCP with a buffer has been chosen because it exhibits features that make it more advantageous for stable, accurate, wide-range current injection in comparison to its counterparts. Additionally, the influence from having two active components in the system is mitigated by using op-amps that are contained in a compact, high precision, and cost-effective, dual-channel IC chip (Texas Instruments, OPA2277). Thus, the AC current source for dual-IPG acquisition has been designed for the most optimal performance.

I.3.iii.d Gain Adjustment of the HCP for Current Variation

During continuous data acquisition, there are a number of circumstances that can cause variations to the quality of the IPG signal. This includes, but is not limited to, an increase in electrolytes at the electrode-skin interface due to sweating, variations in electrode conformity to the skin due to movement, and decreases in sensitivity caused by electrode degradation over time. While the injection frequency directly impacts the ratio between the amount of tissue contribution in comparison to electrode contact contribution, the RMS magnitude of the source also plays a key role in signal quality; where, the greater the applied current, the higher the SNR [33]. As different subjects and/or test cases may require different intensities of current, the current source is designed with a supplemental feature that allows for the adjustment of applied current.

Stemming from Equation 14, the simplest method for current variation without altering the input to the source consists of modifying one component, resistor R_{2b} . By taking advantage of the indirect relationship between R_{2b} and the output current of the improved HCP with a buffer, the current gain can be increased/decreased with a series of parallel resistors and a switch. Figure 15 displays the current gain adjustment stage of the current driving network where R_{i_A} and R_{i_B} represent nodes V_o and V_x in Figure 14.

With an injection frequency of 17 kHz, the lowest resistance in the array of resistors has been set to output an RMS current that is a maximum of 1 mA.

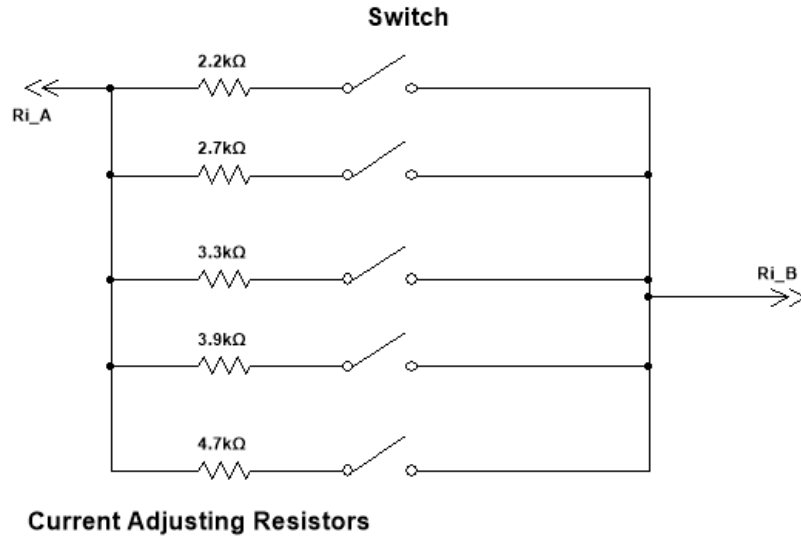


Figure 15. Current Adjusting Segment

With the goal of acquiring data with a high SNR, injecting larger magnitudes of current is an attractive approach to ensuring a better signal quality, especially during acquisition environments that negatively impact the IPG signal. However, driving larger currents results in more power consumption from the system. Not to mention, there are also limitations when applying current to human subjects. Therefore, current regulation and monitoring must be put into place while the dual-IPG system is in use.

For safety purposes, there is a maximum amount of current that can be injected into a subject to minimize tissue heating and danger to the patient. This limit is a function of frequency and has been adopted from the medical equipment standards of the IEC 6060-1.

Equation 15 shows the guard bands that are in place for different ranges of frequency [61, 62].

$$I_{max}(f) = \begin{cases} 100 \mu A & f \leq 1 \text{ kHz} \\ 100 \mu A * \frac{f}{1 \text{ kHz}} & 1 \text{ kHz} < f < 100 \text{ kHz} \\ 10 \text{ mA} & f \geq 100 \text{ kHz} \end{cases} \quad \text{Equation 15.}$$

As mentioned, the operating frequency for the dual-IPG system has been set to 17 kHz. Therefore, according to the medical electrical safety regulations, the maximum current that can be safely injected into the human body at 17 kHz is 1.7 mA. Being that the current source has been designed to peak at 1 mA, the maximum applied current from the device is 58% of what is medically safe for human subjects; however, with any powered circuit comes the possibility of unforeseeable circumstances that can cause the system to act out of specification. Due to this, a current monitoring system in combination with an automatic shutdown feedback loop is integrated into the current driving network.

III.3.iv Current Monitor

I.3.iv.a Common Methods for Continuous Current Monitoring

The ultimate goal for a current monitor with a BIO-Z application, is to recover the RMS of the signal in order to quantify the effective AC applied to the biological medium. One characteristic of skin that must be considered for current measurement is the anisotropic properties of its cells and tissue. When applying current to a biological medium, the pathway of electrical flow is not consistent [63]. Along the longitudinal

axis of a limb, the composition and orientation of cells varies which modifies current flow [63]. This variation can be seen in the voltage response measured from the subject, and even though the signal from the waveform generator is sinusoidal, the signal received from the BIO-Z load may be distorted. Therefore, the approach for recovering the RMS of the signal must be accepting of irregular waveforms while remaining accurate. Commonly, there are three methods used by traditional digital multimeters (DMM) for RMS estimation: average responding, True RMS, and True RMS AC+DC. In order to design a system that can accurately relay the RMS of a BIO-Z signal it is important to explain the theory behind calculated RMS and the options for approximating the RMS of an analog signal.

I.3.iv.b Average Responding

By definition, the RMS of a continuous signal is calculated by squaring the waveform, averaging the sum of each point in the squared signal over a period of time, and taking the square root of that mean. Equation 16 shows the function for RMS.

$$V_{RMS}(t) = \sqrt{\frac{1}{T} \int_0^T V(t)^2 dt}$$

Equation 16.

Contrary to the RMS approach which uses the mean of the squared signal, the average responding method captures the mean absolute value of the continuous signal with the intent of attaining the average rectified value (ARV), or V_{avg} .

The function for the average rectified values is shown in Equation 17.

Equation 17.

$$V_{avg}(t) = \frac{1}{T} \int_0^T |V(t)| dt$$

For a perfect sinusoid with a peak value of V_{pk} , The RMS is equivalent to $\frac{V_{pk}}{\sqrt{2}}$, while the ARV is $\frac{2V_{pk}}{\pi}$. By rearranging both expressions to equate to V_{pk} and solving for V_{RMS} , Equation 18 shows the relationship between the ARV and the RMS of a sinusoidal wave.

Equation 18.

$$V_{RMS} = \frac{\pi}{\sqrt{8}} V_{avg} \approx 1.11 V_{avg}$$

Now, it is clear how the average responding method determines the RMS for a perfect sinusoid with the ARV and a calibration constant (1.11). This approach can be implemented with a simple rectifier and low pass filter, which produces the ARV as a DC signal, and the calibration constant to calculate V_{RMS} . Another alternative includes a more direct recognition of V_{RMS} by obtaining V_{pk} with a rectifier and precise peak detector and multiplying that output by $\frac{1}{\sqrt{2}}$. Both methods will require a calibration protocol to ensure the correct V_{RMS} maps to the detected V_{avg} or V_{pk} .

Despite the fact that the average responding method is the most straightforward, there is a major weakness in its approach that makes it unacceptable for a BIO-Z application: the derivation process that is based off a perfect sine wave. For example, when evaluating a triangular or square wave, Equation 18 no longer remains true. Due to this, a great amount of error can be expected for irregular waveforms like those which

can come from a biological medium. Therefore, an approach that can better account for irregularities should be considered.

I.3.iv.c True RMS and True RM AC + DC

True RMS technology effectively produces the RMS of an AC waveform using methods that directly stem from the formula for RMS. In doing so, the RMS of signals that are not perfectly sinusoidal can be evaluated. At a high level, the analog implementation of Equation 16 is carried out with some multiplier/divider ICs and a LPF. The functional diagram for the execution of this approach is shown in Figure 16.

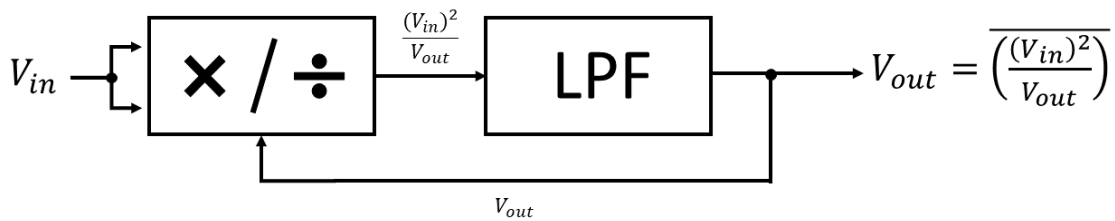


Figure 16. Functional Diagram for RMS-to-DC Technology

The multiplier/divider stage results in an output of $\frac{(V_{in})^2}{V_{out}}$. Similar to the strategy used in the average responding method, the mean of the multiplier/divider output is obtained by passing the signal through a LPF, resulting in a DC signal that is equivalent to $\overline{\left(\frac{(V_{in})^2}{V_{out}}\right)}$. On the account that V_{out} is DC, Equation 19 shows the reinterpretation of V_{out} .

$$V_{out} = \overline{\left(\frac{(V_{in})^2}{V_{out}}\right)} = \frac{\overline{((V_{in})^2)}}{V_{out}}$$

Equation 19.

By reorganizing Equation 19, Equation 20 displays the relationship between the input and the output signal.

$$V_{out}^2 = \overline{(V_{in})^2} \quad \text{Equation 20.}$$

Therefore, by solving for V_{out} , Equation 21 shows how the DC output of True RMS technology relates to the RMS of the input signal.

$$V_{out} = \sqrt{\overline{(V_{in})^2}} = V_{RMS}(V_{in}) \quad \text{Equation 21.}$$

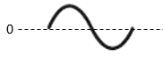
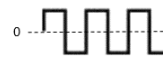
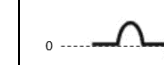

IC's that perform this function are called RMS-to-DC converters and are often employed in True RMS and True RMS AC + DC DMMs. Most ICs will have additional stages for rectification and biasing, but the portion of the RMS-to-DC converter that performs the RMS function is most commonly known as the RMS core.

The only difference between True RMS and True RMS AC+DC is the input to the RMS core. For True RMS, the signal sent to the RMS core is AC-coupled; while, True RMS AC+DC sends a DC-coupled input. When evaluating Equation 16 with an AC waveform that has a DC offset, it is evident that the solution is not equivalent to the that of its AC-coupled counterpart. Therefore, depending on the DC-to-AC ratio of the signal, the True RMS method produces an undeniable amount of error that is not ideal for precise RMS acquisition.

While all methods described can be used to accurately measure a perfect, sinusoidal signal with no offset, only True RMS AC+DC can quantify the RMS value

for both sinusoidal and non-sinusoidal AC signals with and/or without a DC offset [64, 65]. Table 2 displays the accuracy of each method for different types of signals.

Table 2. Accuracy of RMS Estimation Methods

RMS Estimation Method	Result with Sine Wave Input 	Result with Square Wave Input 	Result with Single Phase Diode Rectifier Input 	Result with Sine Wave + DC Offset Input 
Average Responding	Correct	10% high	40% low	~50% low
True RMS	Correct	Correct	Correct	~50% low
True RMS AC+DC	Correct	Correct	Correct	Correct

Note: This table assumes the peak of each waveform is 1 V, the DC offset is 1 V (if applicable), and the input for the True RMS AC+DC method is DC-coupled; while, the input for the average responding and True RMS methods are AC-coupled.

I.3.iv.d True RMS AC+DC for Continuous Current Monitoring

Although the DC offset is removed by the multiple feedback BPF of the AC current source, motion artifacts, skin-electrode adherence, and the composition and orientation of cells in tissue may cause the signal to the RMS core to mildly skew from a zero offset [48]. Therefore, to properly account for any unexpected irregularities in the continuous signal, the True RMS AC+DC method has been implemented in the current monitoring stage of the current driving network with a low-cost, low-power, precision True RMS IC (Analog Devices, AD736). The IC is operated in a DC-coupled configuration; thus, allowing accurate RMS estimation of both AC and AC+DC signals.

Prior to RMS conversion, the input to the RMS-to-DC converter should be obtained from a static component to allow for simple conversion to the RMS current, or

I_{RMS} . Thus, rather than using the voltage across a biological medium with a varying impedance, a $100\ \Omega$, 0.1% resistor is placed in series to the output of the current source and the voltage change of the resistor is obtained by an INA with a gain of 1. Figure 17 displays the arrangement for continuous current monitoring through the shunt resistor, R_s , where the probes represent the voltage difference obtained by an INA.

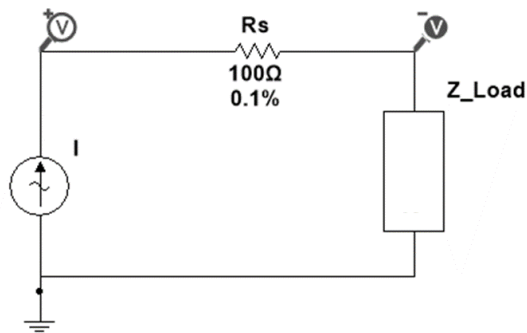


Figure 17. Continuous Current Monitoring Arrangement.

The INA features high precision, high CMMR, and more importantly, high input impedance characteristics to ensure the current applied to the tissue is not altered (Analog Devices, LT6370). The resistance of the shunt resistor R_s is set to $100\ \Omega$ because the resistance remains in the range of typical BIO-Z values from the wrist, and it is small enough to not overload the current source. A low tolerance resistor is used for current monitoring in order to mitigate error from the passive component when calculating the RMS of the applied current. By feeding the AC waveform obtained from the low tolerance shunt resistor to the RMS-to-DC converter, the RMS voltage of the shunt resistor is obtained by sampling the DC signal. The MCU then applies Ohm's law

with the measured RMS voltage and the known resistance R_s . Equation 22 displays the conversion performed by the MCU.

Equation 22.

$$I_{RMS}(t) = \frac{V_{RMS}(t)}{R_s}$$

With the continuous monitoring of the current by the MCU, an automatic feedback loop is programmed to send a digital signal that disables the PMIC and effectively shuts off the entire IPG system if the magnitude of the applied current exceeds 1 mA. The flowchart that describes the code for the automatic feedback loop is displayed in Figure 18.

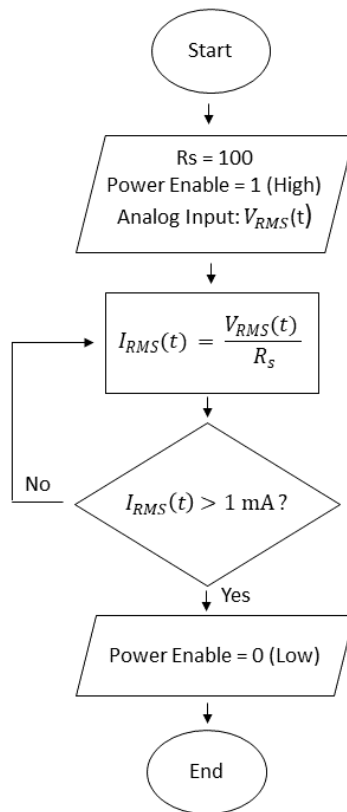


Figure 18. Code Flowchart for the Auto-Shutdown Feature

Lastly, Figure 19 displays the remaining portion of the current driving network with the inclusion of the continuous current monitor.

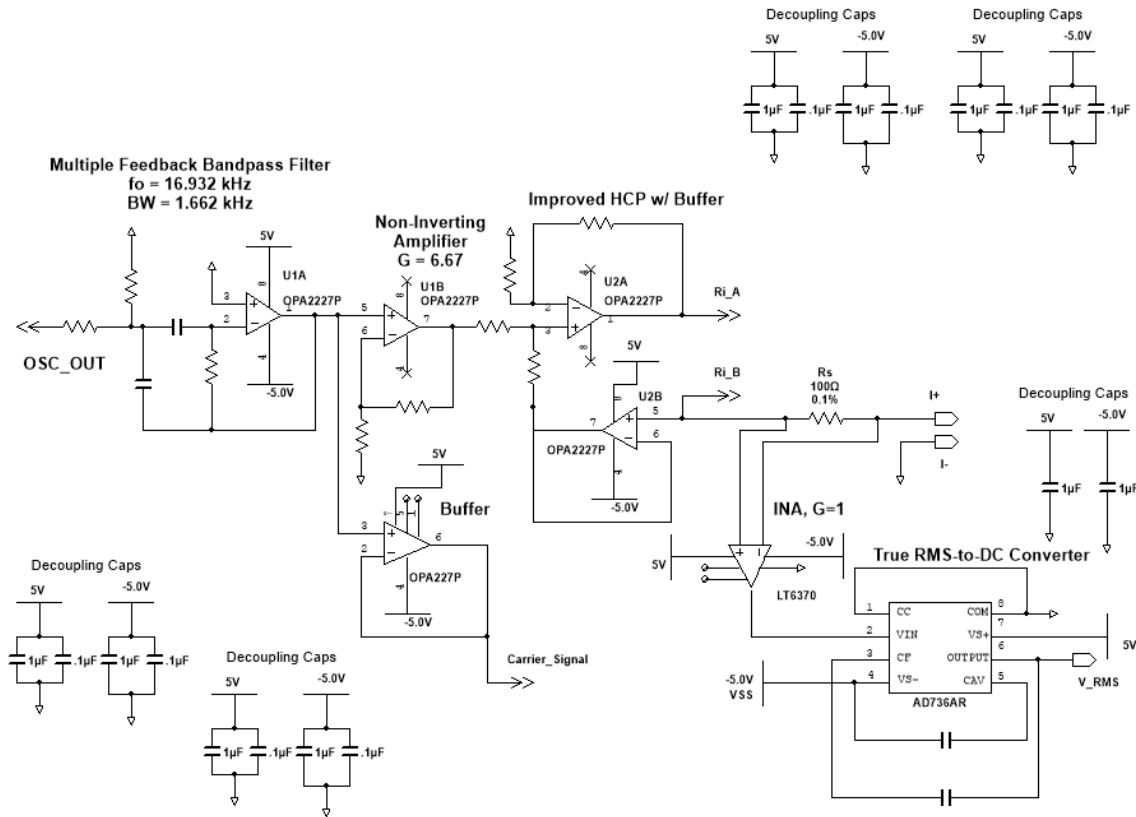


Figure 19. Current Driving and Monitoring Schematic

II.4 AFE Circuit Design: Voltage Sensing Circuit

1.4.i Instrumentation Amplifiers

As mentioned briefly, capacitive coupling at the electrode-skin interfaces is one of the main limitations of the BIO-Z modality. Due to this, the raw signal acquired by the voltage sensing electrodes is cluttered with powerline noise which makes a significant contribution to the common mode voltage. The use of an INA with a high CMRR plays a critical role in reducing the influence of powerline noise on the IPG

signal [66]. Therefore, the same INA in the current monitoring stage of the current driving network is employed to acquire the difference across the BIO-Z. This INA has a CMRR of 94 dB at DC, low voltage noise of $7 \frac{nV}{\sqrt{Hz}}$ at 1 kHz, and maximum gain of 1000 for small magnitude bio-signals. For the dual-IPG system, the gain has been set to 14.44 to produce the largest signal without saturating subsequent stages.

1.4.ii Demodulation (LIA) and Low-Pass Filter

The signal obtained from a pair of voltage-reading electrodes is amplitude modulated (AM); where, the carrier signal is an AC voltage at a frequency that is set by the oscillator in the current injection network, and the message signal is the IPG signal at a frequency near the subject's heart rate (~ 1 Hz). This poses a few design constraints for the wearable device because of the hardware attributes that are necessary for high frequency data acquisition. To prevent aliasing, a modulated signal at 17 kHz would require an MCU that can sample and store continuous, dual-IPG data at a minimum frequency of 34 kHz. As the size of the MCU decreases, it becomes less feasible to meet these needs for data acquisition. Therefore, the voltage measurement network includes a LIA-based demodulation circuit to extract the near-1 Hz IPG signal from its 17 kHz carrier wave and sample at a lower frequency.

Synchronous demodulation by phase-sensitive detection allows the LIA to perform small signal measurement with high SNR. Down to the nanovolt scale, LIAs are capable of extracting low amplitude AC signals out of a variety of interfering intrinsic and extrinsic sources of noise like input noise, 1/f noise, and Johnson/thermal noise, shot noise, and powerline noise [67].

The theory of operation can be explained by beginning with the desired IPG signal, $s(t)$, the AM signal that transmits the IPG signal by the external carrier signal, $x_{AM}(t)$, and the 17 kHz external carrier signal, $c(t)$. For simplicity, the carrier signal is a sine wave with an amplitude of 1, making $c(t) = \sin(\omega_c t)$, where ω_c is $2\pi f_c$. Using the external reference, the LIA creates an internal reference signal, $r(t)$, that has a small phase shift, making $r(t) = V_{ref} \sin(\omega_{ref} t + \theta_{ref})$, where θ_{ref} is the phase shift between the external and internal reference and $\omega_c = \omega_{ref}$. The AM signal is $x_{AM}(t) = \sin(\omega_{AM} t + \theta_{AM})(1 + ms(t))$, where m is the modulation index, ω_{AM} is $2\pi f_{AM}$, and θ_{AM} is the phase shift between the external reference and the AM signal. During synchronous demodulation, phase-sensitive detection includes amplification of the input signal, mixing/multiplying the internal reference signal and the input AM signal, and filtering with a LPF. In doing so, the direct output of the LIA, which mainly performs amplification and mixing, is shown in Equation 23.

Equation 23.

$$\begin{aligned}
 V_{LIA}(t) &= x_{AM}(t)r(t) \\
 &= \left[\frac{1}{2} V_{ref} (1 + ms(t)) \right] \cos([\omega_{AM} - \omega_{ref}]t + \theta_{AM} - \theta_{ref}) - \\
 &\quad \left[\frac{1}{2} V_{ref} (1 + ms(t)) \right] \cos([\omega_{AM} + \omega_{ref}]t + \theta_{AM} + \theta_{ref})
 \end{aligned}$$

Since the AM signal is modulated at the same frequency as the carrier signal, $\omega_c = \omega_{ref} = \omega_{AM}$.

Thus, Equation 23 simplifies down to Equation 24.

Equation 24.

$$V_{LIA}(t) = \left[\frac{1}{2} V_{ref}(1 + ms(t)) \right] \cos(\theta_{AM} - \theta_{ref}) - \left[\frac{1}{2} V_{ref}(1 + ms(t)) \right] \cos(2w_c t + \theta_{AM} + \theta_{ref})$$

It is now apparent that the output of the mixing stage results in an AC signal at two times the carrier frequency, a DC signal, and the IPG signal multiplied by a constant. When this signal is passed through a LPF, Equation 25 shows the final output of the phase-sensitive detection.

Equation 25.

$$V_{PSD}(t) = \left[\frac{1}{2} V_{ref}(1 + ms(t)) \right] \cos(\theta_{AM} - \theta_{ref})$$

As stated previously, the phase contribution from BIO-Z is little to none and can be neglected for IPG acquisition. Thus, the approximated output signal from the synchronous demodulation is displayed by Equation 26, which is a DC signal with a sideband IPG signal at a near 1-Hz frequency.

Equation 26.

$$V_{PSD}(t) = \left[\frac{1}{2} V_{ref}(1 + ms(t)) \right]$$

Figure 20 shows the resulting output.

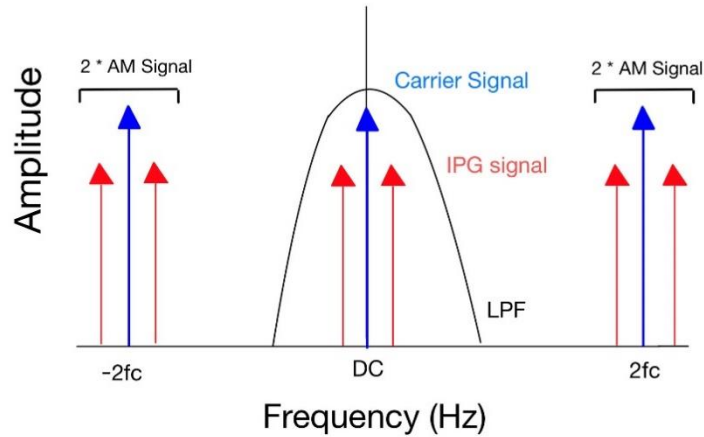


Figure 20. Lock-in Amplifier Response to AM Input

In comparison to other methods, this approach is more sensitive to small signals because the LIA with a LPF only accepts frequencies that are close to the carrier/AM frequency. For instance, Figure 21 shows the voltage noise with signal density of the AM signal with noise.

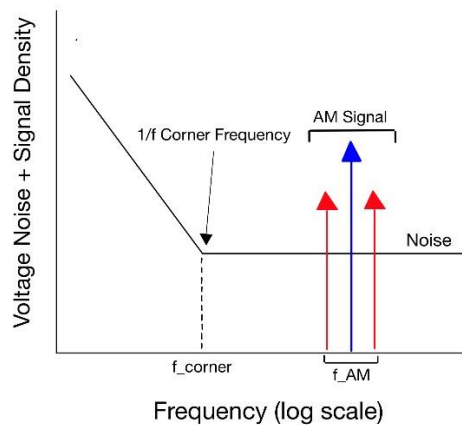


Figure 21. AM Signal with Noise

A BPF with a very high Q-factor and small bandwidth would be required to extract the AM signal with the least amount of noise and pass it through non-synchronous demodulation, like a peak detector. However, because of the nature of a high-Q BPF, there are performance issues at high frequencies due to more power consumption and encountering additional challenges to tune the center frequency as the frequency increases. Additionally, even with a small bandwidth BPF, a lot of the surrounding noise is still captured in the bandpass at the same gain as the desired signal. Figure 22 displays the filtering performance of an ideal BPF.

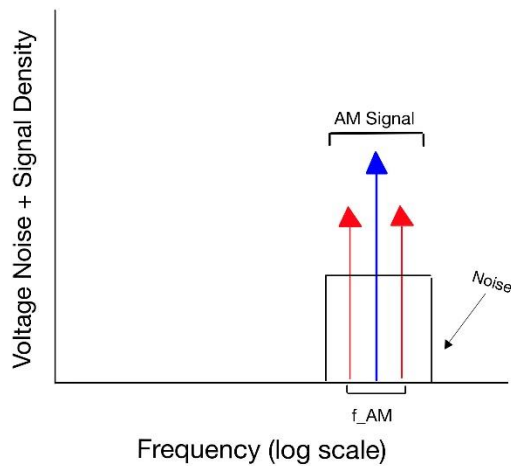


Figure 22. Filtering AM Signal + Noise with an Ideal BPF

Synchronous demodulation by phase-sensitive detection excels because the bandwidth is far more narrower than a BPF and the frequencies that are very close to the desired signal are attenuated at a greater scale [67]. At noise frequencies that are not near the desired signal, $w_{noise} + w_{ref}$ and $w_{noise} - w_{ref}$, the noise is eliminated by the LPF since they are far from the DC and the near 1 Hz signal. Correspondingly, the noise frequencies that are close to the desired signal can be significantly attenuated by a high

order LPF. For instance, a LPF with a cutoff frequency 10 Hz correlates to a BPF with a 20 Hz bandwidth, which is difficult to achieve at high frequencies. Overall, the DC signal and the near 1-Hz IPG signal is unaffected by the LPF which is optimal for the demodulation of a low amplitude IPG waveform.

With the purpose of capitalizing on the benefits of synchronous demodulation, the AD630 by Analog Devices serves as the mixer for the phase-sensitive detection of the IPG waveform. This IC is a high precision balanced modulator/demodulator with a variety of modes and applications [68]. When in the LIA configuration as a phase-sensitive detecting, synchronous demodulator, the AD630 can capture low amplitude signals from 100dB of interfering noise[68]. Despite demonstrating favorable demodulation attributes, the IC comes in a surface mount device (SMD) package that is much larger than most of the components used in the previous stages. Additionally, the data sheet references a 2 MHz channel bandwidth; however, in the LIA configuration, the IC has been optimized for frequencies up to 1 kHz, but “still useful” up to a few hundreds of kilohertz [68]. For this reason, a 17 kHz frequency has been chosen for three reasons: (1) Coté and coworkers have previously synthesized an IPG system at 17 kHz using an alternative circuit design, (2) it is slightly greater than the minimum frequency (10kHz) for penetration of the ICF and ECF, (3) the performance of the chosen demodulation chip degrades at frequencies over 1 kHz; thus, the oscillator should not exceed the minimum penetration frequency by too much.

After the mixing stage the signal is passed through the final stage of the dual-IPG system: a second order LPF with a cutoff frequency of 10.61 Hz and a gain of 1.5.

Figure 23 displays one set of the voltage sensing network.

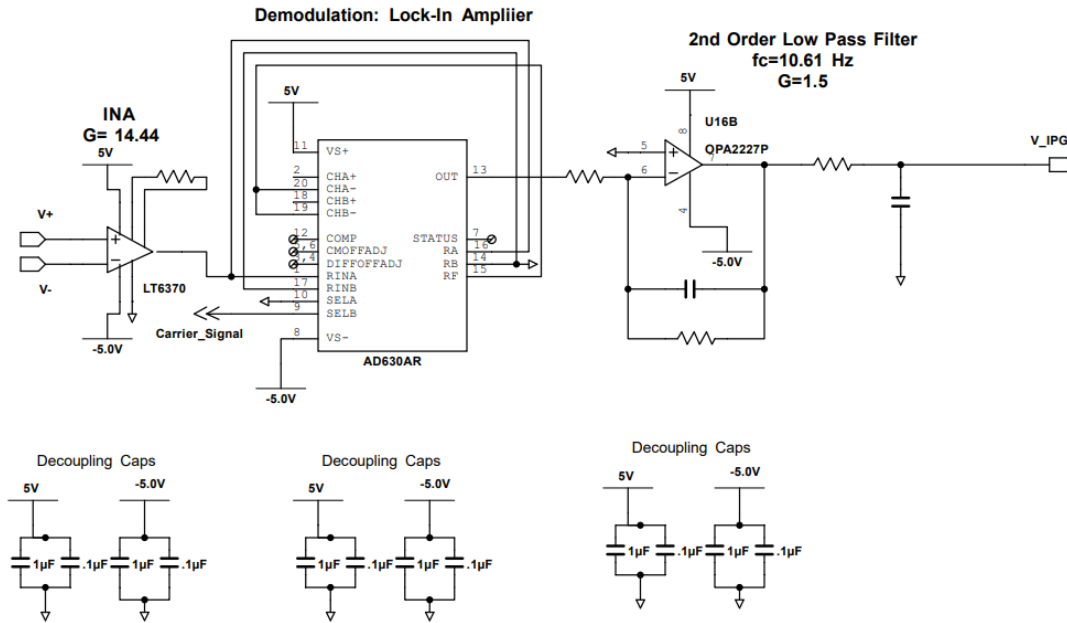


Figure 23. Schematic of Voltage Sensing Network

It is important to note that the carrier signal received by the LIA is a buffered version of the waveform generated in the current driving network because the inputs of the AD630 should be driven by low impedance sources.

CHAPTER III

FEASIBILITY STUDY WITH PROTOTYPE DEVICE

III.1 Introduction: Design of Experiment

As the ultimate goal is to develop a system that may be used for the continuous measurement of HR and PTT, a custom, prototype device was developed to explore the feasibility and effectiveness of the designed circuit. The performance of the device was assessed by acquiring continuous and simultaneous dual-IPG data on three subjects using the prototype device and the standard benchtop system: the BIOPAC's Impedance Cardiography System (BIOPAC Systems Inc., NICO100C). Additionally, before and after the data collection session, the subject's HR was documented by an off-the-shelf cuffed, BP monitor. Three, 45-second trials were collected on each subject with both systems. Each subject remained seated in a static, resting position during data collection. Through signal processing and feature extraction, the MS fiducial points of the IPG signal were identified on MATLAB by Mathworks. Following feature extraction, the computation of HR and PTT was performed for both the data collected on the standard impedance cardiography system and the custom device. Between trials and in each trial, the average HR and PTT was resolved for each subject. The results were assessed by direct comparison to the heart rate monitor and the BIOPAC NICO100C via paired T-test and the percent error.

III.2 Feasibility Study: Materials

III.2.i Feasibility Study: Custom Prototype Device

The custom prototype device consists of the through-hole and/or SMD-to-DIP equivalent of the IC's mentioned in the AFE Circuit Design section. As stated previously, the prototype device was developed to fulfill two main objectives: dual-IPG acquisition and direct comparison of HR and PTT to the standard benchtop system. To achieve these tasks, the parameters of the custom system should correspond to their counterpart in terms of frequency and output current. Due to this, there are some deviations from the final AFE design that allowed the operator to have access to more adjustment features while conducting the study with a simpler iteration of the final device. Figure 24 shows the prototype (8 cm x 9 cm) used for the study.

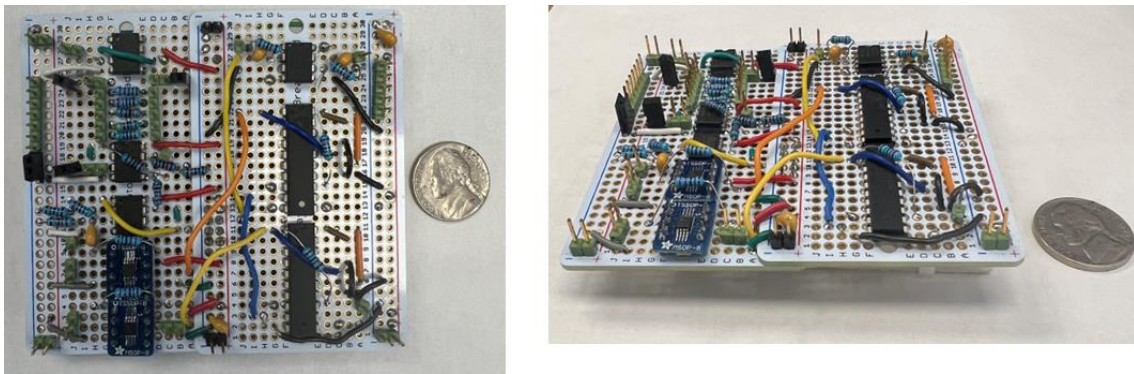


Figure 24. Custom Prototype Device

In terms of circuit design, the feasibility study was performed with just the subsystems that are required for dual-IPG acquisition: the current driver and the voltage sensing networks. This means that the current monitor and its programmable, auto-shutdown feedback loop was not included in the prototype testing. With the purpose of

producing an injection current that is similar to that of the benchtop system, rather than using a multiple feedback BPF, a HPF with a cutoff frequency around 1 kHz was employed to allow for a variety of injection frequencies.

III.2.ii Feasibility Study: Electrodes and Electrode Holder

In collaboration with the Tian Lab at Texas A&M University, add-on nanocomposite dry electrodes were connected to each system for dual-IPG acquisition. These electrodes were placed on an electrode-holder interface that allowed the apparatus to be strapped onto the subject during the data collection session. Figure 25 shows an image of the electrode-holder interface with the dry electrodes connected.

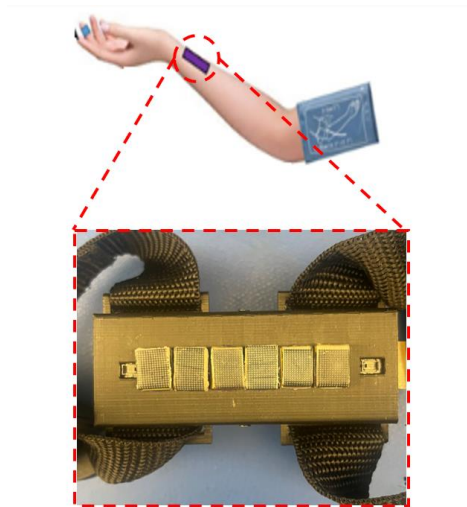


Figure 25. Dry Electrodes on Electrode-Holder Interface

The electrode holder interface is about 1x3 cm in dimension. The connector on the electrode holder interface distributes the signals via FPC cable to a breadboarded cobbler board. This allows the current driving signals to be transmitted and the voltage

response to be received by the custom prototype device or the benchtop system. Figure 26 shows the connection between the electrode holder interface and the cobbler board.

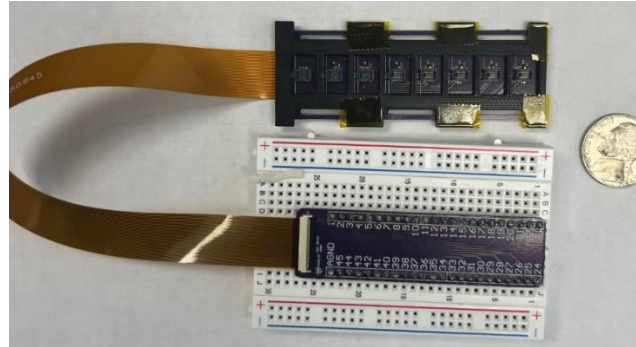


Figure 26. Electrode Interface Connected to Cobbler Board.
(No Electrodes Attached)

III.2.iii Feasibility Study: Acquisition Units

To collect the data from the prototype device, the IPG signals were sampled with the NI USB-6003. Contrarily, the signals from the impedance cardiography system were obtained its own supplementary DAQ: BIOPAC's MP160 in combination with the AMI100D.

III.2.iv Feasibility Study: Other

A standard, off-the-shelf BP monitor was used to collect the subjects cuffed, HR. The ultrasonic doppler machine was used to determine the optimal location along the radial artery of the wrist for IPG measurement. Lastly, signal processing and feature extraction was performed on MATLAB.

III.3 Feasibility Study: Methods

III.3.i Feasibility Study: Initial and Final HR Measurement

Prior to collecting any data, each subject sat for 15 minutes to allow for all cardiovascular activity to stabilize. Once the resting period concluded, a cuffed BP monitor was used to obtain the pre-study HR. At the end of the study, another HR measurement was collected, and the two values were averaged.

III.3.ii Feasibility Study: Electrode Placement and Arrangement

To ensure an accurate placement along the radial artery, a skin marker was used to indicate the ideal signal acquisition location based off the response from the ultrasonic doppler machine. For the six-electrode configuration, the pair of electrodes closest to the heart is denoted the proximal IPG signal, while the pair near the fingertips is the distal IPG signal. Figure 27 provides a visual for the location definitions along the forearm.

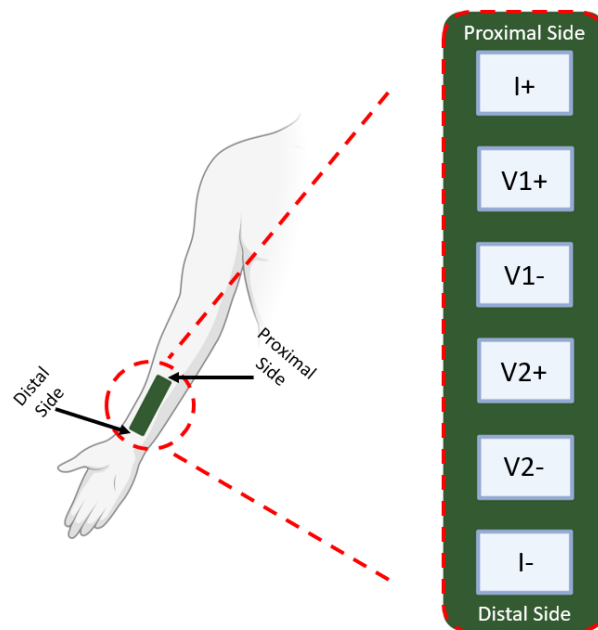


Figure 27. Proximal and Distal Locations for Dual-IPG Acquisition
[Created with BioRender.com]

III.3.iii Feasibility Study: Device and Acquisition Parameters for Dual IPG Acquisition

As mentioned briefly, in order to properly compare and validate the performance of the prototype with the benchtop system, the parameters for the customizable prototype device were configured to settings that directly corresponded to the output of the impedance cardiography unit. Therefore, the injection frequency of the custom prototype was programmed to the same as the benchtop system: 50 kHz. The magnitude of current for the custom prototype was adjusted to 189 μA , which is 15 μA larger than the current applied by the benchtop system; however, since the PTT and HR are the attributes of comparison, time-based parameters like frequency are of main concern rather than a small difference in signal magnitude.

Regarding acquisition parameters, PTT measurements at the wrist can expect values at the millisecond scale [56, 69]. For this reason, the design requirement for the sampling rate of the final iteration has been set to 10 kHz (one sample per microsecond) since it will not present a great demand on an MCU, while remaining fast enough for accurate PTT. Nonetheless, for the feasibility study with the prototype device, both DAQs sampled at a rate of 50 kHz. This is due to the LIA's degradation in performance at higher frequencies, making it necessary to increase the sampling rate to prevent aliasing from residual 50 kHz signal.

Table 3 provides a summary of the device and acquisition settings for the benchtop and custom prototype.

Table 3. Device and Acquisition Settings for Feasibility Study

	BIOPAC	Prototype
Current Injection Magnitude	165 μA	189 μA
Current Injection Frequency	50 kHz	50 kHz
Sampling Rate	50 kHz	50 kHz
Sample Time per Trial	45 s	45 s

III.3.iv Feasibility Study: Dual-IPG Signal Processing and Data Analysis for HR and PTT

III.3.iv.a Filter

The first stage of the signal processing procedure includes filtering the raw signals obtained from the custom prototype and benchtop system. An infinite impulse response LPF with a cutoff frequency of 4.5 and a steepness of 0.85 was used to extract the desired IPG signal. Figure 28 shows an excerpt of filtering stage from the MATLAB code.

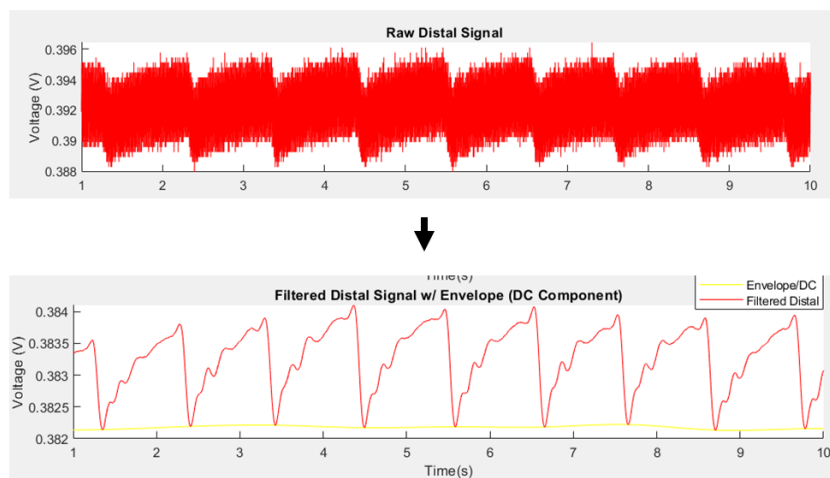


Figure 28. Signal Processing: Filtering Stage

III.3.iv.b Envelope Removal

Due to the basal impedance of an IPG signal and the nature of LIA operation, there is a DC and low frequency signal (0.14-0.9 Hz) that should be extracted from the filtered IPG waveform. By doing so, the contribution of the pulsatile and non-pulsatile components of an IPG waveform can be isolated and analyzed separately.

To extract the non-pulsatile component, an envelope detector is used to identify the lower envelope of the filtered IPG signal. The outcome of this function results in the waveform for the basal impedance. As the equation for the IPG signal is the sum of the pulsatile and non-pulsatile component, the MATLAB code then subtracts the acquired basal signal from the total, which isolates the pulsatile component for subsequent feature identification. Lastly, with the goal of making the MS point of the IPG waveform more distinguishable, the derivative of the pulsatile, or AC, component is taken feature extraction as well.

Figure 29 shows a sample of the envelope removal stage from the signal processing procedure.

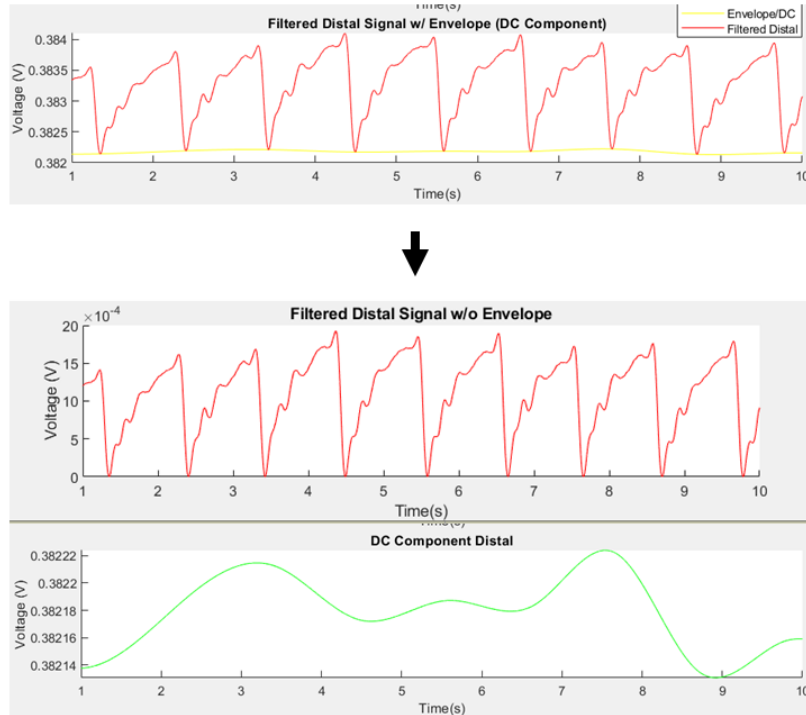


Figure 29. Signal Processing: Envelope Removal

III.3.iv.c Feature Extraction

For this feasibility study, the MS points of the IPG signals were identified for HR and PTT computation. The waveform of the IPG derivative was inverted, making the MS point the “peak” of the signal. A peak detector was then used to obtain the location/time of the MS peaks for the next stage of signal processing.

Figure 30 shows the identification of the MS points on the IPG derivative.

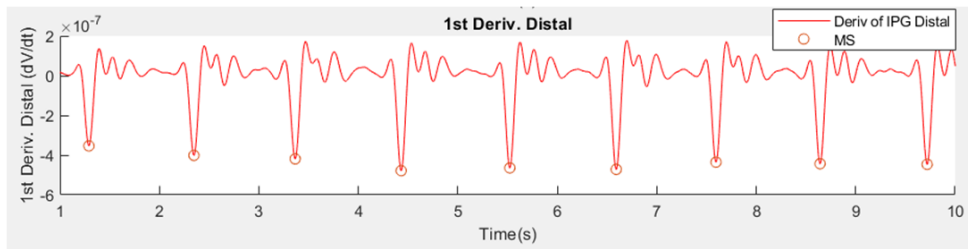


Figure 30. Signal Processing: Feature Extraction

III.3.iv.d HR Computation

Although the HR can be obtained from both of the dual-IPG signals, the MATLAB code recovers the HR from the pair of electrodes located on the distal region of the wrist. Being that the impedance change from systolic activity is the most distinct feature of the IPG waveform, the frequency of MS peaks should not differ between IPG pairs. Additionally, the signal resolved from the distal region typically has a higher SNR due to less tissue being encountered at that area in comparison to the proximal region. For those reasons, it is acceptable to obtain the HR solely from the distal pair in good faith.

In regard to the computation protocol, HR is defined as beats per minute, the MATLAB code assesses the frequency of the MS points divided by the total acquisition time (45 s). This calculation results in one HR value per trial. Therefore, only the average HR and standard deviation was collected for each system and not HR within the trial.

III.3.iv.e PTT Computation

Due to how small the distance is between the electrode pairs on the wrist, the continuous measurement of PTT is highly sensitive to several distortion sources including, but not limited to, motion, unstable electrode-skin adherence, electrode placement that deviates from the radial artery, and backflow of blood from the relaxation of the vascular walls after systole. The result of these distortion sources may cause instances of negative PTT during computation, where the cardiovascular fiducial points obtained from the proximal region trails that of the distal rather than leads. Physiologically, these instances do not accurately describe the flow of blood in the cardiovascular system and should be treated as errors. The program compensates for this by removing any negative PTT values obtained during the analysis.

Figure 31 provides a visual of negative PTT during continuous measurement and Figure 32 shows incidents of PTT error over time.

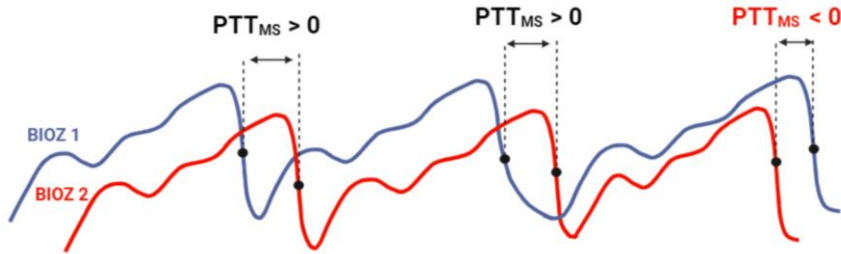


Figure 31. Occurrences of Negative PTT
[Created with BioRender.com]

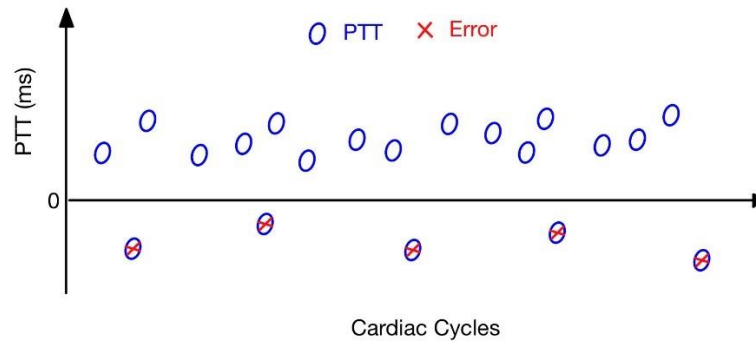


Figure 32. PTT Error Occurrence Over Time

For computation, the MATLAB code obtains PTT by subtracting the time of a MS occurrence in the distal signal from the corresponding time of a MS occurrence in the proximal signal. This calculation is done for each MS instance in each trial. Therefore, there are multiple PTT resolved from one trial of dual-IPG acquisition. Equation 27 displays the function used to obtain PTT.

$$PTT_{MS} (s) = t_{MS_{Distal}} - t_{MS_{Proximal}} \quad \text{Equation 27.}$$

After error compensation, the average and standard deviation of PTT is reported between trials and for each individual trial. Additionally, as error compensation is performed for each trial, the error occurrence ratio (EOR) is reported for each trial and the average EOR is reported between trials. Equation 28 displays the definition of the EOR.

$$EOR (\%) = \frac{\# PTT \text{ Errors}}{\# Total PTT \text{ Occurrences}} * 100$$

Equation 28.

III.3.v Feasibility Study: Statistical Analysis

Ideally, the performance goal for the custom prototype device is to function similarly to the benchtop impedance cardiography system. To validate the HR and PTT measurements from the prototype, the percent error between the detected features was obtained. Additionally, paired t-tests were conducted with the results collected from the prototype, the benchtop system, and the cuffed HR/BP monitor (for HR only). In doing so, significant difference between the average HR and PTT collected from each instrument can be confirmed or denied.

III.4 Feasibility Study: Results and Discussion

III.4.i Feasibility Study: Error Ratio

The EOR varied across each subject. Figure 33 and Figure 34 display the within trial and between trial EOR for the BIOPAC and custom device, respectively.

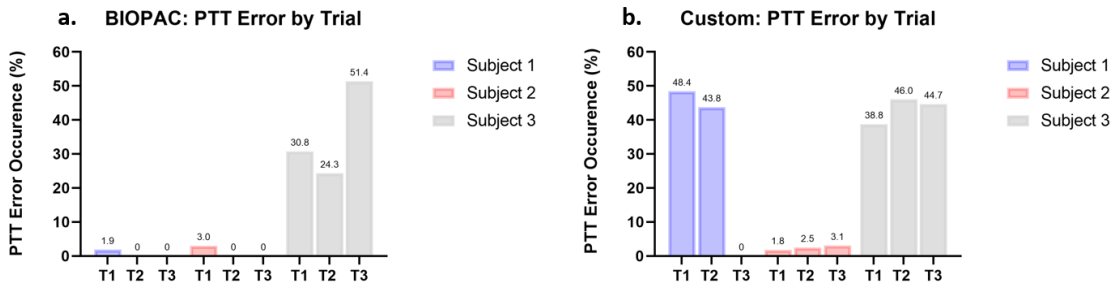


Figure 33. Feasibility Study: Within Trial EOR. a) BIOPAC: EOR by Trial. b) Custom: EOR by Trial.

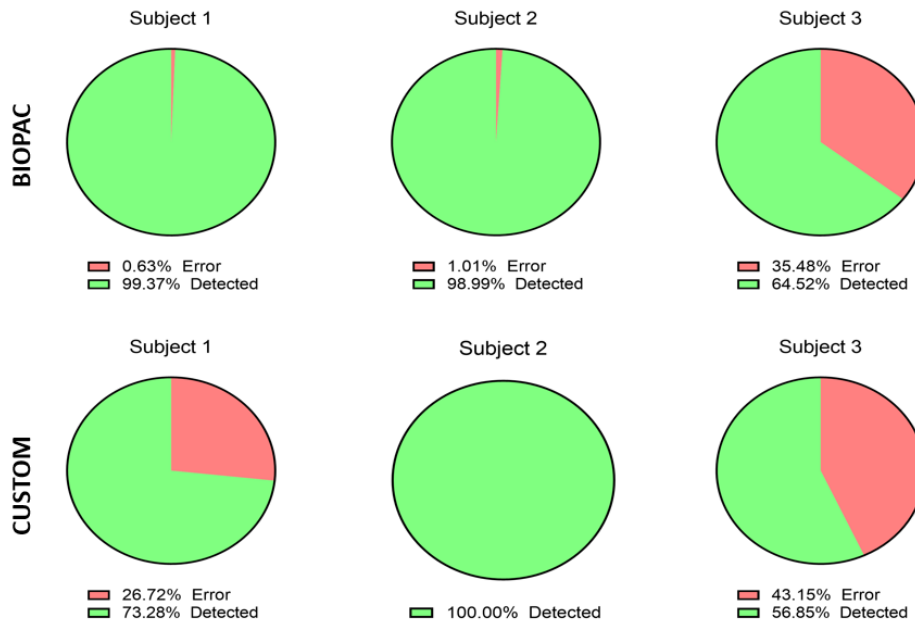


Figure 34. Feasibility Study: Between Trial EOR

III.4.ii Feasibility Study: HR and PTT Detection

Figure 35 displays the within trial HR and PTT acquired from the BIOPAC and prototype device.

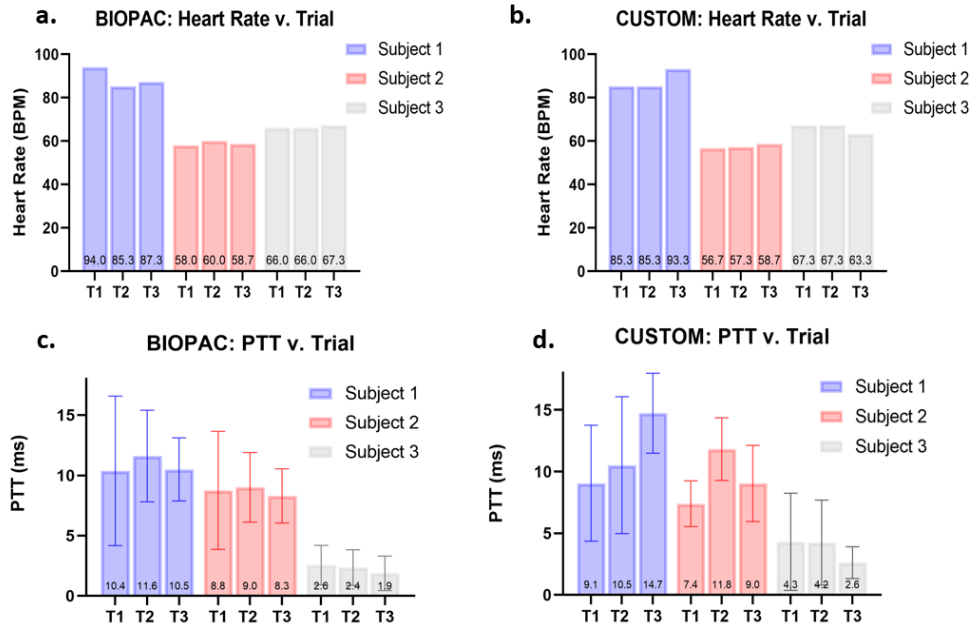


Figure 35. Feasibility Study Within Trial HR and PTT. a) BIOPAC: HR by Trial. b) Custom: HR by Trial. c) BIOPAC: PTT by Trial. d) CUSTOM: PTT by Trial.

Figure 36 displays the between trial HR and PTT acquired from the BIOPAC and prototype device.

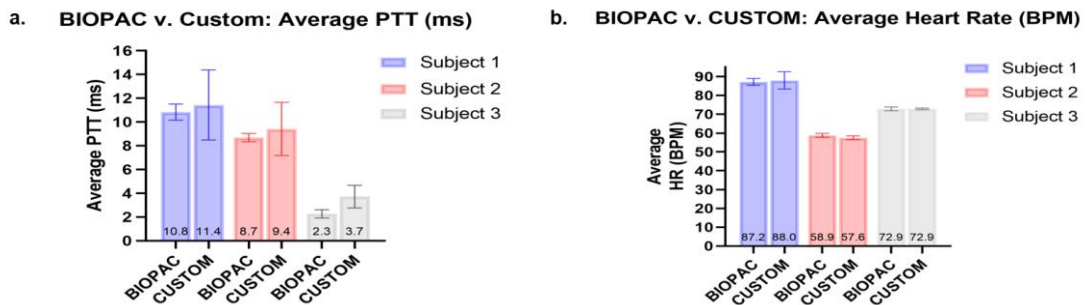


Figure 36. Feasibility Study Between Trial HR and PTT. a) PTT Comparison Between BIOPAC and Custom. b) HR Comparison Between BIOPAC and Custom.'

A summary of the between trial PTT and HR exhibited by each system is shown in Table 4 and Table 5, respectively, with a percent error analysis.

Table 4. Feasibility Study: Between Trial PTT of BIOPAC and Prototype

Subject #	BIOPAC		CUSTOM		% Error Between AVG PTT
	AVG PTT (ms)	STD (ms)	AVG PTT (ms)	STD (ms)	
1	10.830	0.681	11.438	2.951	5.618499743
2	8.694	0.359	9.416	2.241	8.305631281
3	2.267	0.351	3.724	0.956	64.2732152

Table 5. Feasibility Study: Between Trial HR of BIOPAC and Prototype

Subject #	BIOPAC		CUSTOM		% Error Between AVG HR
	AVG HR (BPM)	STD (BPM)	AVG HR (BPM)	STD (BPM)	
1	88.889	4.538	88.000	4.538	1.000
2	58.889	1.018	57.556	1.018	2.264
3	66.444	0.770	66.000	2.309	0.669

The PTT paired t-test resulted in no significant difference between the mean detected PTT of the BIOPAC and prototype device ($P = 0.742$). Similarly, the HR paired t-test concluded no significant difference between the mean HR of the BIOPAC and the prototype device ($P = 0.730$).

III.5 Chapter Summary and Conclusions

In this chapter, the prototype device was able to produce continuous, dual-IPG waveform for the detection of HR and PTT over a 45 second period. Although the EOR for the prototype device was generally larger than the benchtop system, the HR performance of the device remained accurate and precise. The HR acquired from the prototype displayed low variability and low percent error from the benchtop impedance cardiography system and the reference, cuffed BP/HR monitor. In doing so, the paired t-test deemed that the HR results from the benchtop system and prototype device were from the same population, which validates the HR readings collected from the prototype.

In terms of continuous PTT monitoring, the results from the feasibility study highlighted the increased sensitivity that comes with PTT in comparison to HR. While both the benchtop and prototype devices expressed low variation for HR monitoring, both PTT results displayed higher standard deviations within each trial and between trials. When compared to the benchtop system, the prototype device showed greater variation in PTT. Despite this, the paired t-test deemed no significant difference between the measured PTT both units, which validates the PTT data collected from the prototype.

Although both the HR and PTT obtained by the prototype device corresponded to the benchtop system, additional measures should be taken to decrease the PTT variability. Moreover, a study with more subjects and a longer data collection time can be useful for better understanding the AFE's performance for the continuous monitoring of HR and PTT.

CHAPTER IV

PERFORMANCE CHARACTERIZATION OF FINAL AFE HARDWARE

IV.1 Introduction: Design of Experiments

Following HR and PTT validation with the prototype, the final iteration of the device was fabricated onto a 1 cm x 3 cm printed circuit board (PCB). Figure 37 displays an image of the PCB, which consumes a total of 246.2 mW.

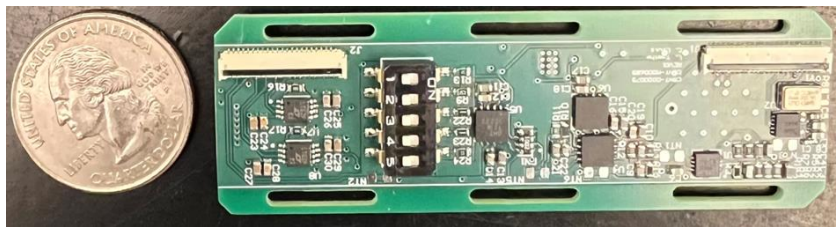


Figure 37. Dual-IPG PCB

In order to characterize the device's performance, preliminary studies were conducted for the current driving and monitoring subsystems. The goal of these studies was to determine two device attributes: the range of impedances that can be loaded onto the current source and the accuracy of the continuous current monitor. By conducting these studies at each of the various output currents, an optimal magnitude of current and range of resistive load cells were chosen for the succeeding calibration and in vivo studies. Additionally, a quick functionality test was performed to simulate and employ the automatic shutdown feature.

Following the preliminary studies, to fully describe the impedance of a biological medium, the output of the IPG system was converted to ohms by a resistive calibration

process. This allows for measurements from the device to be reported in units that are standard to BIO-Z. Prior to utilizing the calibration curves for an in vivo study, the method of calibration was validated by comparing the measured impedance from the calibrated device to that of a benchtop LCR meter. A series of single-dispersion Cole models served as the test load to ensure the calibration approach was suitable for describing complex impedances.

Lastly, after device calibration, an in vivo study was performed on six subjects (3 male, 3 female). Wet electrodes (3M, 2560 Red Dot™ ECG Electrode) were used for the in vivo study because they are the standard for clinical practices and the dry electrodes used in the feasibility study are mounted on foam, causing a drift in impedance until stabilization. During data collection, the following features were extracted: HR, PTT, average change in pulsatile impedance (ΔZ_p), and average basal impedance (Z_b).

IV.2 Preliminary Study 1: Loading Limits of Current Source

IV.2.i Preliminary Study 1: Overview

All sensors share a common parameter that plays a key role in determining the application of the device: the upper limit of quantification (ULOQ). This parameter is defined as the highest amount of the target substance that can be measured with precision and accuracy by the sensor. It is important to determine this parameter to ensure that the sensor can perform accordingly in a wrist wearable environment. Therefore, before the dual-IPG system can be calibrated, it is necessary to establish the loading limitations of the device.

For this system, the effectiveness of the device relies largely on the quality of the current injection signal. If the applied current exhibits any type of inconsistencies, the resulting signal measured from the electrodes will display the same effects. Therefore, this preliminary study determines the maximum loading impedance by the current injection network where the performance of this system was assessed at different resistor loads. Evidently, the current delivered by an ideal current source is consistent and independent of the load; however, real current sources will display a relationship between the load and the current delivered. Typically, the amount of current gradually decreases as the load increases. Using this information, the ULOQ was determined by utilizing the current detection system, sweeping the load impedance, and quantifying the RMS current v. load impedance relationship. This methodology was applied to each injection current output. The impedance values that result in an RMS current that is 90% of the nominal value was defined as the maximum impedance load for the device.

IV.2.ii Preliminary Study 1: Materials and Methods

Using the PCB for the final iteration of the dual-IPG system, the output of the current driving subsystem was applied to twenty-seven resistive test loads, R_L , at a tolerance of 0.1%.

Figure 38 displays a diagram for the experiment. The resistor values used were 1, 10, 16, 20, 25, 34, 47.5, 56, 68, 75, 100, 150, 180, 220, 270, 470, 680, 750, 820, 910, 1000, 1200, 1600, 1800, 2200, 2700, and 3300 Ω .

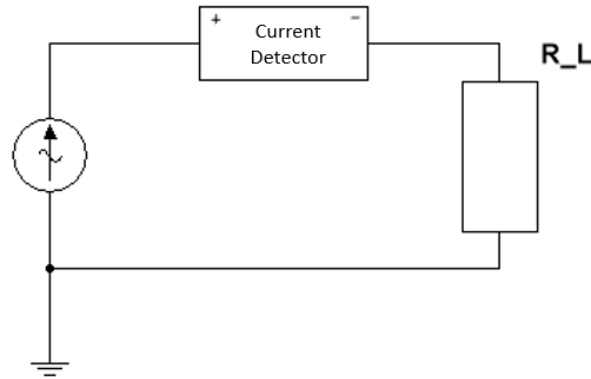
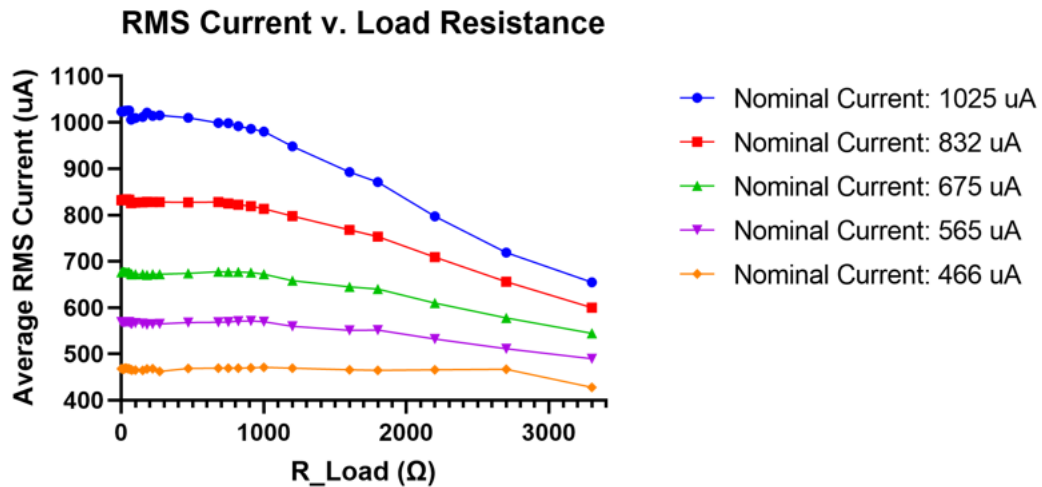


Figure 38. Preliminary Study 1: Schematic Diagram for ULOQ Study

During current application, the current detector samples the magnitude of current through the load for 5 seconds at a sampling rate of 10 kHz. For each resistor value at each applied current, three trials of data was collected. The average current with its standard deviation is reported between trials and within a trial. With the five resistors in the current adjusting subsystem of the current driving network, five different current outputs were applied to the resistive loads. This protocol was executed at each magnitude of current detected by the current monitor subsystem (1025, 832, 675, 565, and 466 μA).

IV.2.iii Preliminary Study 1: Results and Discussion

Figure 39 displays the relationship between the load resistance and the average output current.



Note: The standard deviation bars are too small to view; however, for all currents the variability ranged from 4.61-5.61 μ A.

Figure 39. Preliminary Study 1: Average RMS Current v. Load Resistance

It is important to note that one RMS current detected by the current monitoring subsystem is above 1 mA. Due to the fact that a resistor load was used, and the detected current is slightly above the threshold, the auto-shut off feature was disabled for this study to allow for full characterization of the device's performance.

Using the graphs obtained at each current setting, the estimated maximum load impedance for each current was determined. Table 6 summarizes these results, where the ULOQ is the resistance that causes a 10% current reduction from the nominal.

Table 6. Preliminary Study 1: Estimated ULOQ Load of Current Source

Nominal Current (μA)	R_L @ 90% Nominal Current ($k\Omega$)
1025	~1.4
832	~2.0
675	~2.2
565	~3.0
466	>3.3

Overall, as the current magnitude increased the ULOQ impedance decreases for the current source. In any case, all the ULOQs are much larger than the expected BIO-Z at the forearm. Thus, the design of the current driving network is acceptable for this application.

IV.3 Preliminary Study 2: Current Monitor Accuracy and Feedback Loop

IV.3.i Preliminary Study 2: Overview

Commonly, portable current detectors, like DMMs, use a resistive load to measure AC and DC signals. Thus, the ideal test condition for detecting the effective current across a load is to use a resistor with an impedance value that is in the range of typical BIO-Z measurements on the wrist. In doing so, the designed system was evaluated using a load that is similar in magnitude to a BIO-Z load without the distortion that can come from a live subject. In a tetrapolar configuration, impedance values from the wrist commonly range between 1-100 Ω ; thus, a resistive load of 47 Ω is used to validate the current detector's performance in phase one of this preliminary study [42,

47, 70]. The output from the system was converted to current and compared to a calibrated DMM. The schematic for the test setup is shown in Figure 40.

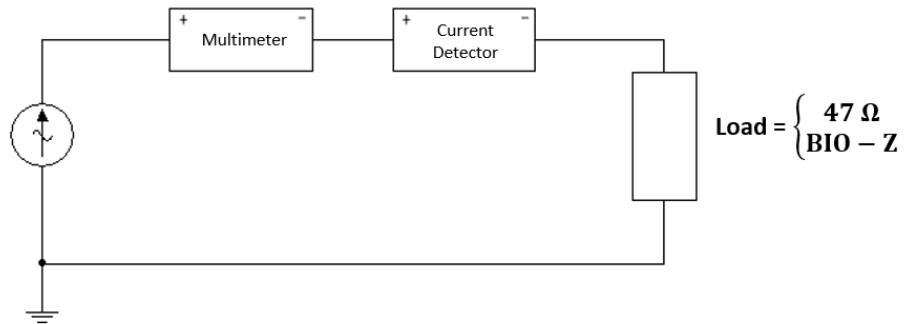


Figure 40. Preliminary Study 2: Schematic Diagram for Current Accuracy Study

After displaying feasibility of the current sensor with a resistive load, the accuracy of the system was assessed with the non-ideal, real world test condition: a BIO-Z load. The output from this system was also compared to the values measured by the calibrated DMM. The test set up remains the same for part one where the load is the impedance of the wrist rather than a resistor.

Lastly, part three of the preliminary study confirms the function of the auto-shutdown feedback loop.

IV.3.ii Preliminary Study 2: Materials and Methods

IV.3.ii.a Preliminary Study 2.i: Examine Current Detector Accuracy with Resistor Loads

The current output of the PCB was used to apply current across a 47 Ω load. Similar to the first preliminary study, all five of the current outputs were applied to the resistor load. During current application, the output of the current monitoring subsystem

was sampled for 5 seconds at a sampling frequency of 10 kHz. For each current, three trials of data were collected. The average current with its standard deviation is reported between trials and within a trial. The current values measured by the fabricated device were compared to the current measured simultaneously by the DMM. The results are reported in percent error followed by a paired t-test to determine if there is a significant difference between the measured current of the device and the DMM.

IV.3.ii.b Preliminary Study 2.ii: Examine Current Detector Accuracy with BIO-Z Load

For part two of the preliminary study, the current monitor was evaluated with the tetra-polar electrode configuration on a subject. All five currents were injected and the current applied was detected by DMM and the fabricated device simultaneously. The sampling time and frequency were set to the same settings as part 1 of this preliminary study. Additionally, the results were reported in the same manner as well.

IV.3.ii.c Preliminary Study 2.iii: Functionality Test of Auto-Shutdown Feature

For the testing of the auto-shutdown feature, the current was set to the second highest current of the device ($832 \mu A$) for 60s. Then, the MCU was switched to the highest current ($1025 \mu A$). During this period of time, the digital output of the MCU to the PMIC was recorded at a sampling frequency of 100 Hz to ensure the enable was set to low when an RMS current exceeded 1 mA.

IV.3.iii Preliminary Study 2: Results and Discussion

IV.3.iii.a Preliminary Study 2.i: Current Detector Accuracy with Resistor Load

The relationship between the measured current by the DMM and the current monitoring subsystem with a resistive load is displayed in Figure 41.

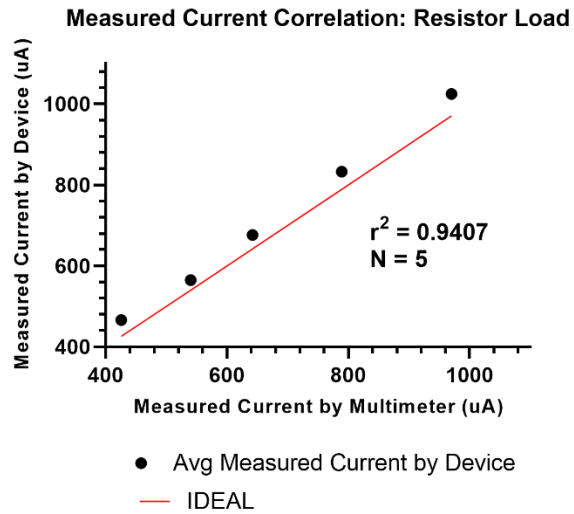


Figure 41. Preliminary Study 2.i: Correlation of Measured Current with Resistor Load

The paired t-test for the resistive load measurements resulted in a P-value of 0.0013, meaning there was a significant difference between the mean RMS current measured by the DMM and the current monitoring subsystem. Additionally, the paired t-test concluded that the average difference between the two groups was $39.33 \mu A$.

A summary of the measured data by both devices with a percent error analysis is provided in Table 7.

Table 7. Preliminary Study 2.i: Accuracy of Current Detector with Resistor Load

Measured Current Within Each Trial						Measured Current Between Trials		% Error Between Device AVG and DMM	
T1 AVG (μA)	T2 AVG (μA)	T3 AVG (μA)	T1 STD (μA)	T2 STD (μA)	T3 STD (μA)	AVG (μA)	STD (μA)	DMM (μA)	% Error
1023.8	1025.0	1025.0	3.43	3.44	3.46	1024.6	0.71	970	5.63
831.8	832.6	832.5	3.40	3.40	3.41	832.3	0.45	789	5.49
676.3	676.0	675.6	3.64	3.64	3.64	676.0	0.32	642	5.29
564.8	564.8	564.9	3.32	3.33	3.31	564.8	0.09	540	4.60
466.1	466.0	465.9	3.27	3.28	3.29	466.0	0.08	426	9.39

Despite the significant difference, the percent error for all currents was less than 10% with a resistor load. By plotting the measured current relationship, a high correlation and coefficient of determination was observed while the current measured by the device is near-parallel to the ideal. It can be assumed that current measured by the current monitoring subsystem is precise; however, the accuracy is shifted by an average offset of $39.33 \mu A$. A simple current calibration protocol can be implemented to increase accuracy.

IV.3.iii.b Preliminary Study 2.ii: Current Detector Accuracy with BIO-Z Load

Due to the current detection offset discovered when examining the accuracy of the current monitoring subsystem with a resistor load, the actual injection current at the highest setting is less than 1 mA ($970 \mu A$) rather than $1025 \mu A$. Therefore, the second part of this preliminary study proceeded with all 5 currents applied to the same BIO-Z load. The relationship between the measured current by the DMM and the current monitoring subsystem is displayed in Figure 42.

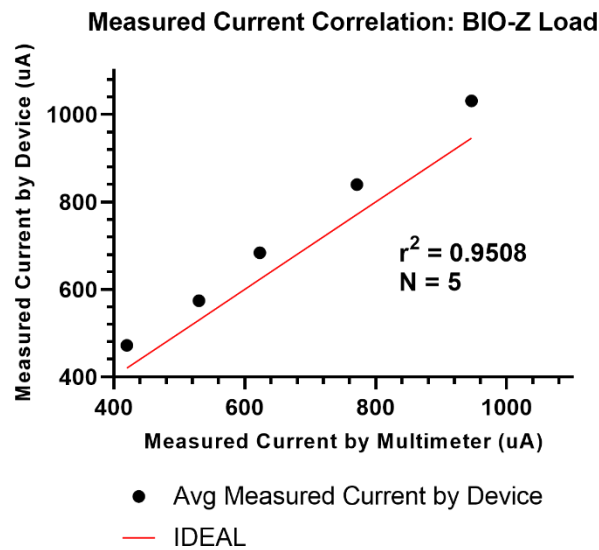


Figure 42. Preliminary Study 2.ii: Correlation of Measured Current with BIO-Z

The paired t-test for the BIO-Z load resulted in a P-value of 0.0009 and the average difference between the two groups was $62.06 \mu A$.

A summary of the measured data by both devices with a percent error analysis is provided by Table 8.

Table 8. Preliminary Study 2.ii: Accuracy of Current Detector with BIO-Z Load

Measured Current Within Each Trial						Measured Current Between Trials		% Error Between Device AVG and DMM	
T1 AVG (μA)	T2 AVG (μA)	T3 AVG (μA)	T1 STD (μA)	T2 STD (μA)	T3 STD (μA)	AVG (μA)	STD (μA)	DMM (μA)	% Error
1032.5	1030.5	1029.7	3.34	3.35	3.28	1030.9	1.46	946	8.98
840.6	839.5	839.3	3.34	3.31	3.30	839.8	0.70	771	8.92
683.6	683.8	683.6	3.37	3.38	3.38	683.7	0.08	623	9.74
573.8	574.3	574.1	3.51	3.49	3.49	574.1	0.21	530	8.31
471.2	472.2	472.3	3.51	3.49	3.49	471.9	0.56	420	12.35

Like the accuracy study with the resistive load, a high correlation and coefficient of determination was expressed by the current monitoring subsystem. As expected with an unideal, BIO-Z load, the overall error for all output currents and the average difference between the two systems was slightly larger than that of the study with the resistor load. While the measurements of the current monitoring subsystem for a BIO-Z load is precise and follows the same trends as that of the DMM, the accuracy can greatly increase with the same type of calibration methods mentioned in the results of the previous current accuracy mini-study for the resistor load.

IV.3.iii.c Preliminary Study 2.iii: Auto-shutdown Feature Functionality Test

After examining the accuracy of the current detector, the auto-shutoff feature was activated, and the digital output response to detecting an RMS current above 1 mA is shown in Figure 43.

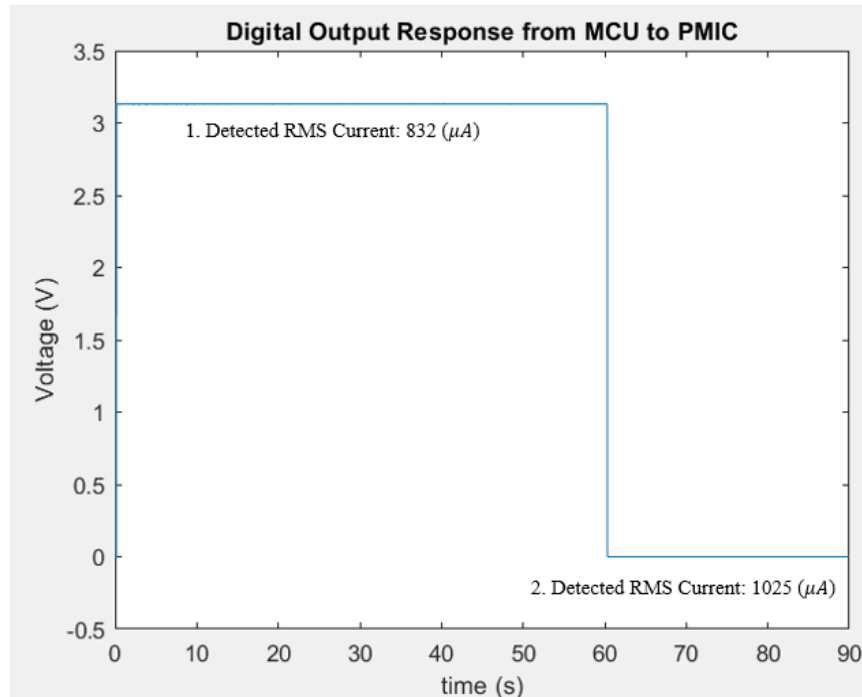


Figure 43. Preliminary Study 2.iii: Functionality Test for Automatic Shutdown Feature

To summarize the results in Figure 43, Table 9 describes the enabling/disabling output to PMIC.

Table 9. Preliminary Study 2.iii: Summary of Digital Response to PMIC

Detected Current (μA)	Digital Output to PMIC (High/Low)
832	High (Enable)
1025	Low (Disable)

By simulating a current output above 1 mA, the automatic feedback loop successfully triggered a system power off.

IV.4 Preliminary Study 3: Calibration

IV.4.i Preliminary Study 3: Overview

A resistive calibration approach was used to convert the voltage output from the dual-IPG system to ohms. Resistor modeling can be used because 1) a tetrapolar/six electrode configuration mitigates the influence from the skin-electrode contact impedance, 2) a majority of the IPG signal is composed of the real component of BIO-Z, and 3) the demodulation stage of the voltage measurement network is phase-sensitive. Additionally, this technique has been adopted by many bioimpedance-based instruments, like BIOPAC's Impedance Cardiography System and the RJL Bioelectric Impedance Analyzer (RJL Systems Inc, RJL 101A) [71, 72]. Although this method has proven to be inaccurate at frequencies above 500kHz, its performance at lower frequencies authorizes its use for this application due to the linear relationship occurring at 17 kHz [73].

By taking advantage of the almost-resistive properties of continuous BIO-Z measurements along the radial artery, linear calibration curves were obtained to map the output voltage of the device to a series of load resistors. To ensure the calibration method could be used for complex impedances, the device was calibrated and used to measure a set of single-dispersion Cole models. The measured impedance from the device was then compared to that of a standard benchtop LCR meter.

IV.4.ii Preliminary Study 3: Materials and Methods

IV.4.ii.a Preliminary Study 3.i: Obtaining Calibration Curves

Calibration curves were obtained for all five current outputs. The experimental set up is described in Figure 44, where the current source includes the current monitoring subsystem, R_L represents the resistor load, and R_c represents the impedance experienced by the AC current source and the current driving electrodes. Resistor loads of 10, 25, 34, 47.5, 56, 68, 75, and 100 were used during this part of the calibration study. These values were chosen because the standard impedance cardiography system (BIOPAC) maxes out at 100 Ω , the impedance of the wrist is expected to be between 1-100 Ω , and after determining the ULOQ of the device, it is certain that these values will not overload the current source.

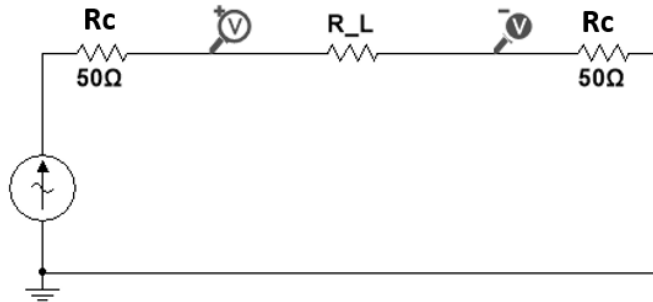


Figure 44. Preliminary Study 3.i: Schematic Diagram for Obtaining Calibration Curves

While applying the current to system, the voltage drop across the load resistor served as the input to the voltage sensing network. The final voltage output from the

voltage sensing network was sampled at 10 kHz for 5 seconds. Three trials of data were obtained for each resistive load at each current. Calibration curves were created by plotting the relationship between the average measured voltage and the value of the resistive load.

IV4.ii.b Preliminary Study 3.ii: Validation of Calibration Method

After obtaining the calibration curves for each current, the calibration equation for one current ($565 \mu A$) was used to validate the calibration method by measuring a series of complex loads rather than resistors. This current was chosen because it displayed the lowest percent error during the current accuracy study. Figure 45 displays the setup for this experiment where R_1 , R_2 , and C make up the single-dispersion Cole model, R_c remains as the skin-electrode contact impedance that the current passes through in a tetrapolar and/or six-electrode configuration, and the current source includes the current monitoring subsystem.

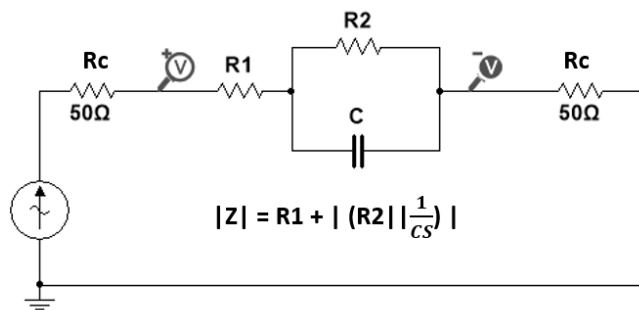


Figure 45. Preliminary Study 3.ii: Schematic Diagram for Calibration Method Validation

Table 10 consists of the different single-dispersion Cole model configurations that were measured by the device. These values are based off of a phantom used in literature for BIO-Z/IPG calibration [41].

Table 10. Preliminary Study 3.ii: Calibration Validation Component Values

Test Case #	R₁ (Ω)	R₂ (Ω)	C (nF)	Theoretical Impedance (Z) at 17 kHz (Ω)
1	22	22	150	42.75
2	10	22	150	30.75
3	47	22	150	67.75
4	68	22	150	88.75
5	22	10	150	31.87
6	22	47	150	59.55
7	22	68	150	67.98
8	22	22	68	43.72
9	22	22	330	39.39

For each test case, three measurements were made by the calibrated device at a sampling rate of 10 kHz for 5 seconds. Following device measurement, the LCR meter was used to measure single-dispersion model and the measured values of both systems were compared to each other and the respective theoretical impedance of each test case.

IV.4.iii Preliminary Study 2: Results and Discussion

IV.4.iii.a Preliminary Study 2.i: Calibration Curves

Figure 46 displays the calibration curves obtained for each output current setting.

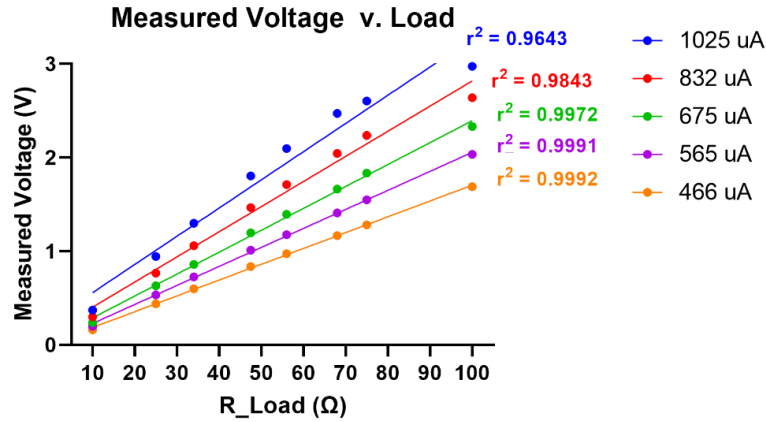


Figure 46. Preliminary Study 2.i: IPG Calibration Curves

The calibration equations for each current setting are described in Table 11.

Table 11. Preliminary Study 2.i: Calibration Curve Equations

Nominal Current (μA)	Calibration Curve Equation	Coefficient of Determination (R^2)
1025	$V = 0.03011 * R + 0.2560$	0.9643
832	$V = 0.02683 * R + 0.1339$	0.9843
675	$V = 0.02339 * R + 0.05368$	0.9972
565	$V = 0.02030 * R + 0.02546$	0.9991
466	$V = 0.01688 * R + 0.01645$	0.9992

The linear calibration curves for each current setting include a non-zero y-intercept. No compensation was performed to set the y-intercept to zero because it can be assumed that a 0 Ω load will still relay an impedance due to parasitic elements.

While the variation in measured voltage was too small to depict for each current applied, Figure 47 displays the within trial standard deviation at every load resistance.

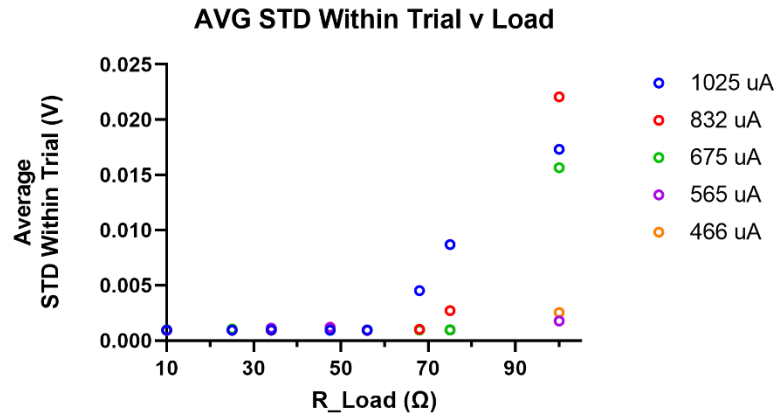


Figure 47. Preliminary Study 2.i: Standard Deviation of Measured Voltage v. Load

Although the standard deviation is relatively small, as the load resistance increases, there is also an increase in variability; however, this is expected due to more thermal noise at larger load resistances. Even so, a detected current of 565 μA was used for the remaining studies because of its low variation, high correlation and coefficient of determination, and the lowest percent error regarding current detection accuracy.

IV.4.iii.b Preliminary Study2.ii: Validation of Calibration Methods

Following calibration with $565 \mu A$ calibration equation, the relationship between the theoretical impedance and the measured impedance by the LCR meter and the dual-IPG device is displayed in Figure 48.

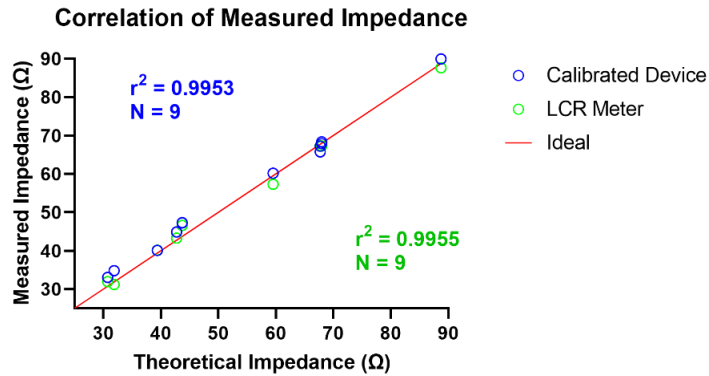


Figure 48. Preliminary Study 2.ii Measured Impedance of LCR and Calibrated Device v. Theoretical Impedance

To compare the measured impedance of both units, the relationship between the measured impedance of the LCR meter and the calibrated, dual-IPG device is plotted in Figure 49.

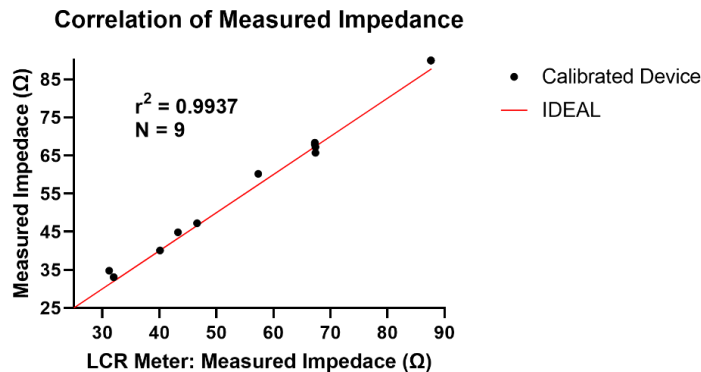


Figure 49. Preliminary Study 2.ii: Calibrated Device v. LCR Meter Measured Impedance

Table 12 provides a summary of the measurements obtained by the benchtop LCR meter and the calibrated device with a percent error analysis.

Table 12. Preliminary Study 2.ii: Measured Impedance of LCR Meter and Calibrated Device

Test Case #	T1 (Ω)	T2 (Ω)	T3 (Ω)	AVG (Ω)	STD (Ω)	LCR Meter (Ω)	% Error Between Device AVG and LCR
1	44.844	44.904	44.929	44.892	0.0435	43.27	3.749
2	33.019	33.049	33.076	33.048	0.0286	31.97	3.372
3	67.234	65.695	65.790	66.240	0.8625	67.38	1.692
4	89.932	89.946	89.973	89.950	0.0205	87.62	2.659
5	34.783	34.816	34.837	34.812	0.0273	31.19	11.613
6	60.168	60.183	60.200	60.184	0.0162	57.32	4.996
7	68.346	68.365	67.873	68.195	0.2789	67.28	1.359
8	47.237	47.278	47.327	47.281	0.0452	46.6	1.461
9	40.086	40.067	40.077	40.077	0.0095	40.12	0.108

The paired t-test for calibrated device v. LCR meter comparison resulted in a P-value of 0.027, meaning there was a significant difference between the mean impedance measurements. Nonetheless, the average difference between the two groups was a mere 1.325 Ω and because the models were static impedances, this difference is to be seen in the measured basal impedance of an IPG waveform. Thus, an average 1.325 Ω difference in a basal impedance range of 1-100 Ω is acceptable considering the percent error for the test cases were low and the correlation and coefficient of determination were high.

IV.5 In Vivo Study

IV.5.i In Vivo Study: Overview

Following the calibration of the entire system, an in vivo study was conducted on a total of six subjects (three male, three female). Dual-IPG acquisition was performed to capture HR, PTT, and the variation in BIO-Z from subject-to-subject. In comparison to the PTT extraction methods in Chapter III, a new approach was adopted to decrease the variability in PTT. Regarding the BIO-Z traits, two parameters were extracted for further analysis: the average basal impedance (Z_b) and the average of the max change in pulsatile impedance (ΔZ_p). Statistical analysis was performed to determine if there is a significant difference in impedance between male and female subjects. The raw data for the figures of the in vivo study are provided in Appendix A.

IV.5.ii In Vivo Study: Materials and Methods

IV.5.ii.a In Vivo Study: Data Acquisition

Like the feasibility study, each subject sat for 15 minutes to allow for all cardiovascular activity to stabilize before data collection. The ultrasonic doppler machine was used to find the optimal location for electrode placement along the radial artery. Although the electrode-holder interface was not used in this study, the wet electrodes were applied in the same arrangement as that of Figure 27, where the proximal electrodes are closer to the heart, the distal electrodes near the fingertips, and the current driving electrodes sandwich the voltage sensing electrodes.

Figure 50 displays wet electrode placement along the radial artery.

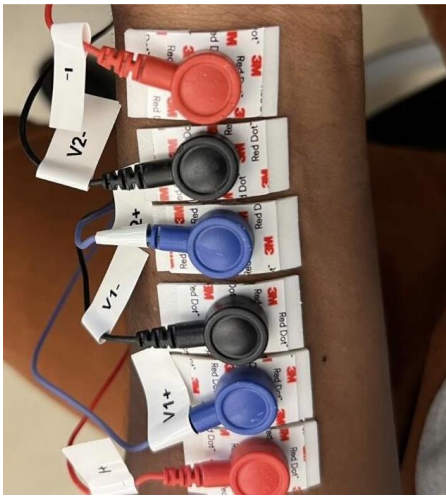


Figure 50. In Vivo Study: Wet Electrode Placement

For each subject, three trials of dual-IPG data were sampled at a rate of 10 kHz for 90 seconds. The magnitude of current was set to the same that was used to validate the calibration method: $565 \mu A$. Table 13 provides a summary of the device and acquisition settings for the in vivo study.

Table 13. In Vivo Study: Device and Acquisition Settings

Current Injection Magnitude	565 μA
Current Injection Frequency	17 kHz
Sampling Rate	10 kHz
Sample Time per Trial	90 s

IV.5.ii.b In Vivo Study: Signal Processing

Other than one deviation made in the feature extraction stage, the signal processing approach was the same as the methods used in the feasibility study. Rather than only extracting the MS point, the SYS and DIA features were identified and included for PTT computation. Figure 51 shows an example of one channel MS peak,

SYS foot, and DIA peak detection with the GUI made on the MATLAB software. The code for the in vivo study is provided in Appendix B.

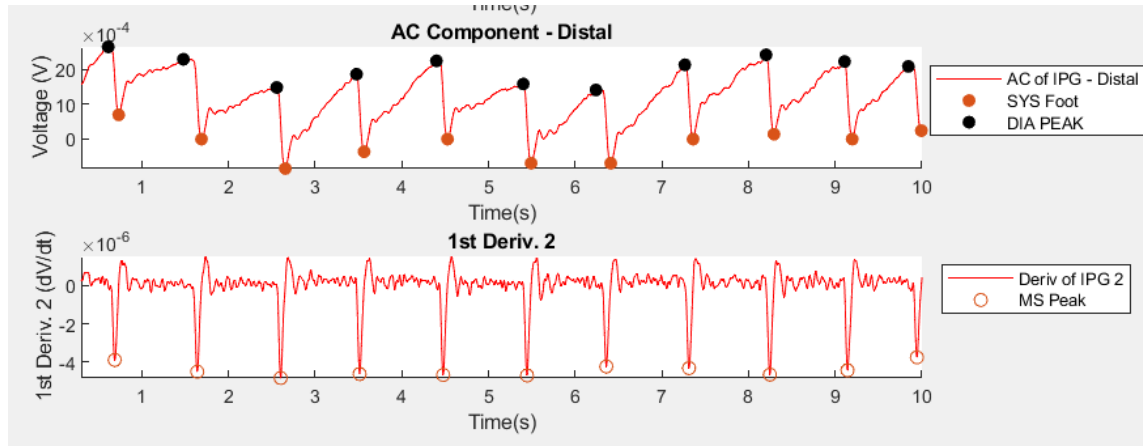


Figure 51. In Vivo Study: Feature Identification of SYS, DIA, and MS

IV.5.ii.c In Vivo Study: HR Computation

Since the HR detection performed in the feasibility study showed small variability, no significant difference between the detected HR of the benchtop system, and a high correlation to the benchtop system and the reference HR monitor, the computation methods remained the same for the in vivo study.

IV.5.ii.d In Vivo Study: PTT Computation

With the goal of reducing the variance in PTT, two modifications were made to the PTT computation methods used in the feasibility study from Chapter III: the addition of the SYS and DIA fiducial points for PTT calculation and the omission of PTTs that are unrealistic for detection at the wrist (> 30 ms). By adding the PTT from the SYS foot and DIA peak for calculation, an overall average PTT that included the average PTT

from the MS, SYS, and DIA points were reported for each subject. Equation 29 and Equation 30 define PTT function for the added fiducial points.

$$PTT_{DIA}(s) = t_{DIA_{Distal}} - t_{DIA_{Proximal}} \quad \text{Equation 29.}$$

$$PTT_{SYS}(s) = t_{SYS_{Distal}} - t_{SYS_{Proximal}} \quad \text{Equation 30.}$$

Equation 31 displays the expression for the reported PTT.

$$PTT = \frac{avg(PTT_{DIA}) + avg(PTT_{SYS}) + avg(PTT_{MS})}{3} \quad \text{Equation 31.}$$

In regard to PTT exclusion, the MATLAB code considered any PTT over 30 ms as an error. Detecting PTTs at values over 30 ms is not realistic for electrode pairs that are closely separated; thus, these incidences may occur due to motion artifacts and/or detecting a fiducial point in one IPG pair and not the other.

Figure 52 provides a visual for the error compensation performed in the in vivo study.

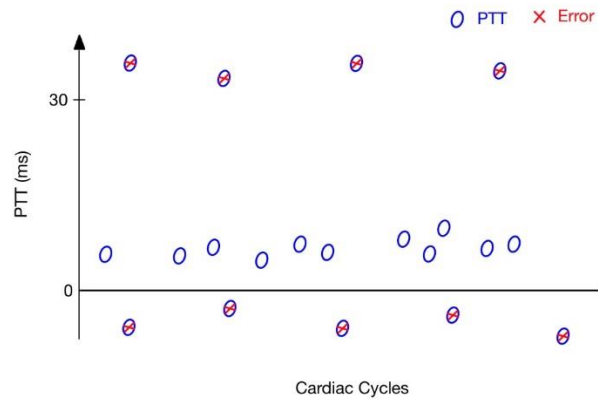


Figure 52. In Vivo Study: Error Compensation

IV.5.ii.e In Vivo Study: Pulsatile and Basal Impedance Acquisition

By utilizing the equation obtained from the calibration curve, the voltage, dual-IPG waveforms were converted to ohms. The basal impedance was then defined as the average of the DC/envelope of the IPG signals. The pulsatile impedance was obtained by subtracting the DIA peak from the SYS foot and averaging that max change in BIO-Z within a trial.

IV.5.iii In Vivo Study: Results and Discussion

IV.5.iii.a In Vivo Study: PTT and HR Detection

In obtaining the average PTT from the MS, DIA, and SYS fiducial points, Figure 53 displays these results for each subject.

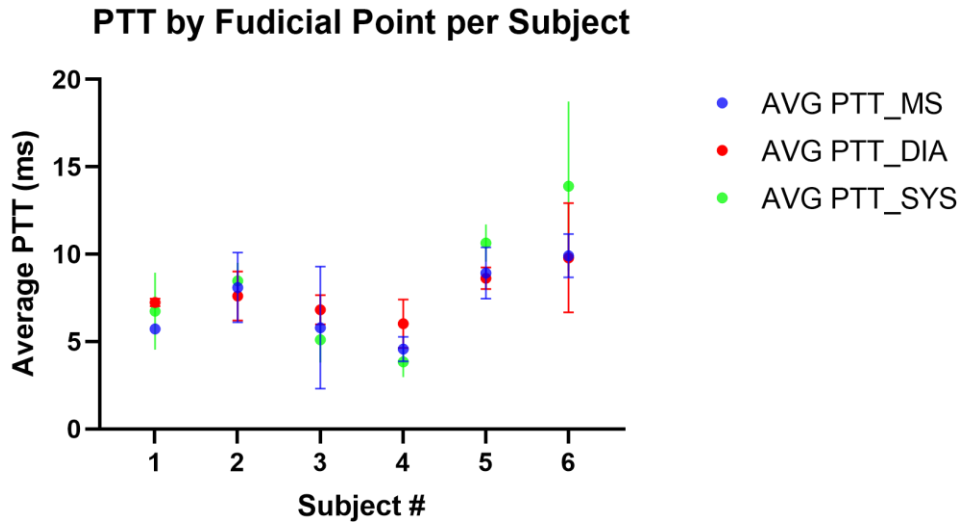


Figure 53. In Vivo Study: Detect PTT by Fiducial Point Per Subject

As shown, the PTT obtained from each fiducial point follows a similar trend between subjects. By using all three features for PTT time computation, there is more confidence in the overall results.

Figure 54 displays the collected HR and PTT from each subject where blue indicates male and purple indicates female.

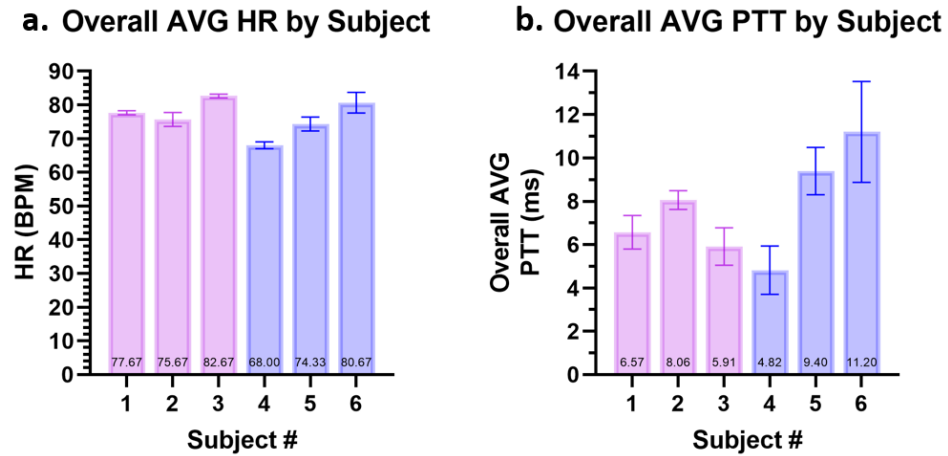


Figure 54. In Vivo Study: Average HR and PTT. a) Average Detected HR by Subject. b) Average Detected PTT by Subject.

When comparing to the feasibility study, the variability in the collected HR corresponds to that of the prototype device, which displayed accurate and precise HR detection. In regard to PTT monitoring, the standard deviation for each subject, except subject 6, was reduced by about 50%. Thus, the new approach to PTT computation improved the precision of the device’s PTT detection.

IV.5.iii.b In Vivo Study: Pulsatile and Basal Impedance

Since the IPG signal was acquired at two locations, the basal and pulsatile impedance was observed at the proximal and distal regions. Figure 55 displays the basal

impedance by each subject at both detection areas. The diagonal lines indicate the male subjects.

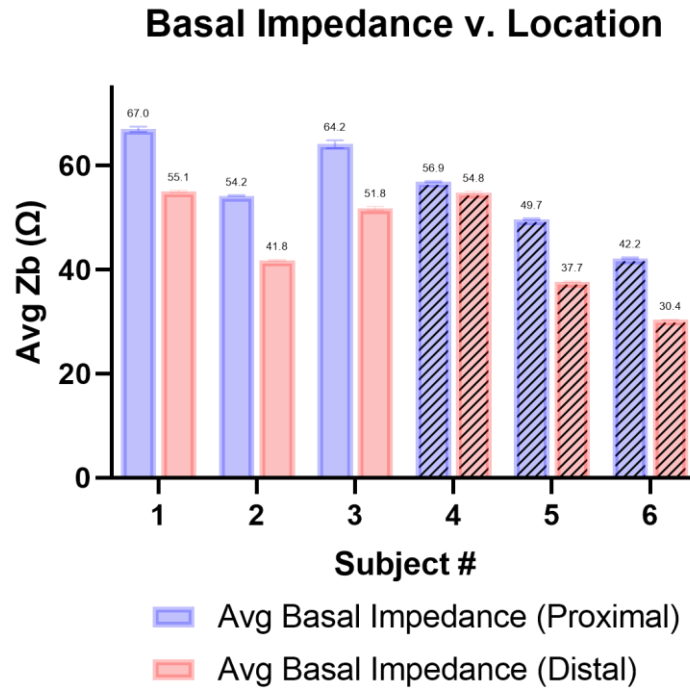


Figure 55. In Vivo Study: Basal Impedance v. Location

As expected, the proximal location resulted in a larger impedance for all test subjects. This is because there is usually more tissue along the forearm as you move closer to the heart; thus, a greater BIO-Z at the proximal pair of voltage sensing electrodes was examined. Additionally, the measured basal impedances are within the typical range of BIO-Z near the wrist (1-100 Ω).

Figure 56 shows the pulsatile impedance obtained from each subject at both locations, where the diagonal lines indicate a male subject.

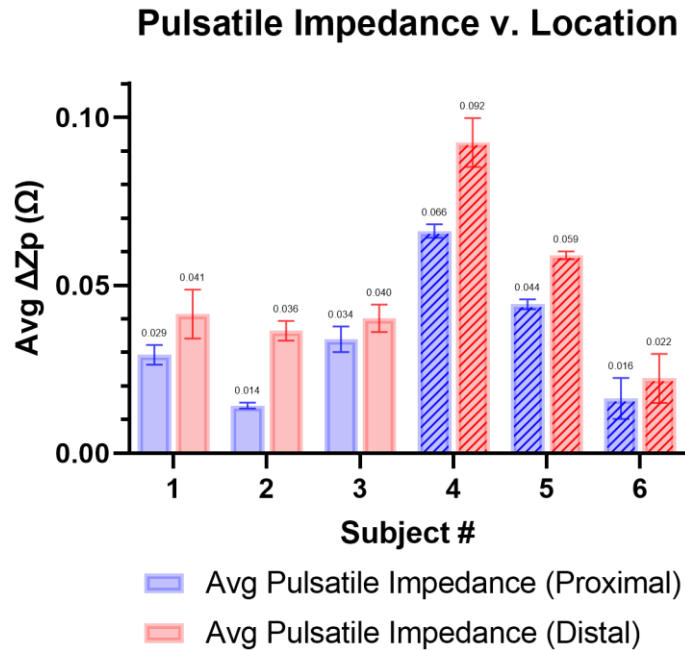


Figure 56. In Vivo Study: Pulsatile Impedance v. Location

Overall, the pulsatile impedance at the distal location was larger than that of the proximal for all subjects. This result is mainly due to the tissue-to-artery ratio at each location. Since the electrodes confide in a small area, the cross-sectional area of the artery does not differ as much between the IPG sensors; however, depending on the BMI of the subject, the tissue area can significantly increase along the forearm near the heart. Therefore, the distal location interacts with less tissue, which allows for better resolving of the blood's contribution to BIO-Z and a larger SNR. Additionally, the measured pulsatile impedances are within the expected displacement of BIO-Z due to cardiac activity (up to 0.1 Ω).

To understand if sex influences the basal and pulsatile impedance, Figure 57 displays a side-by-side comparison for both parameters.

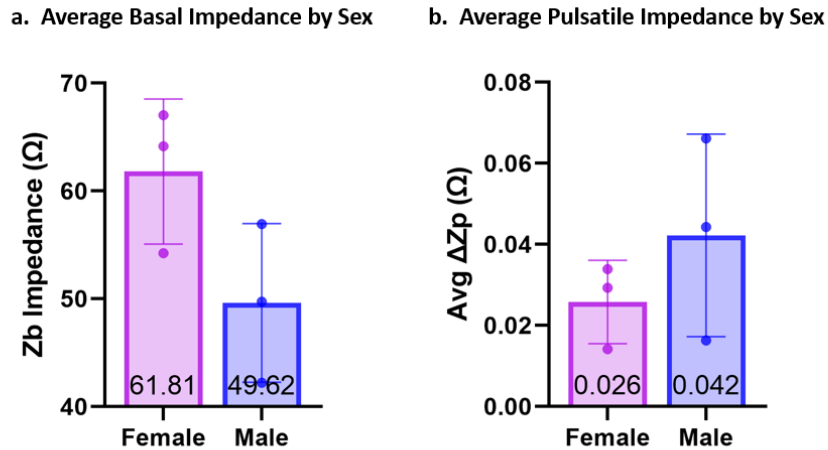


Figure 57. In Vivo Study: Measured Impedance by Sex. a) Average Basal Impedance by Sex. b) Average Pulsatile Impedance by Sex

On average, the female subjects displayed a larger basal impedance and smaller pulsatile impedance when comparing to their male counterparts. This is most likely due to the cardiovascular and body composition differences between males and females. Women typically have a much lower cardiac output than men, resulting in a smaller pulsatile impedance. Additionally, body fat, which is a substantial contributor to BIO-Z, is usually higher in women than men, causing higher basal impedance measurements for female subjects. Even so, other factors like hydration, BMI, and cardiovascular health can cause the basal impedance and pulsatile impedance to vary significantly within one sex. For this reason, the unpaired t-test for both the basal impedance and pulsatile

impedance determined no significant difference between male and female subjects with a P-value of 0.015 and 0.3511, respectively.

IV.6 Cost of Goods

The total price of components for the dual-IPG AFE is shown in Table 14. It is important to mention the potential price of the entire system is also dependent on the production cost, which varies by manufacturing site and their fee for labor, assembly, material, desired profit margin, etc. For a University laboratory, the cost of components for the proposed AFE is a start but can not be directly compared to the total cost of commercially available BP/HR monitors.

Table 14. Cost of AFE Components

Components	QTY	Unit Price	Total
AD630	2	38.21	76.42
XTAL	1	20.25	20.25
AD9837	1	6.27	6.27
AD8045	1	4.99	4.99
OPA2227	3	13.20	39.60
OPA227	1	7.62	7.62
LT6370	3	7.62	22.86
AD736	1	14.98	14.98
RES	29	0.05	1.45
CAP	52	0.05	2.60

TOTAL 197.04

The cost of the AD630, the 16 MHz crystal oscillator, and the precision op-amps (OPA2227) make up more than half of the total for this circuit. A future design should implement a precision mixer/multiplier that is lower in price for lock-in amplification. Additionally, rather than utilizing a programable DDS, the PWM output from the MCU could be filtered to generate a sinusoidal waveform, which would eliminate the need for

the XTAL and AD9837; however, this option is only acceptable if there is minimal distortion in the sine wave. Another option would be to utilize a standard 16 MHz oscillator rather than a spread spectrum oscillator, which offers similar functionality at 1/20th the price. Lastly, the OPA2210 can replace the OPA2227. This IC is a drop-in replacement and provides better performance at 1/3rd the cost. Alternatively, the quad-package of the OPA2227 can also be used to drive costs down rather than the using dual-package.

Overall, as one of the main goals for POC technology is to deliver healthcare at an affordable price point, the reduction in the total component cost for the AFE combined with a reasonable overall pricing structure as noted above to match or be less than current devices could thus be attractive to insurance companies, especially considering the novelty in the system's intended application over existing systems namely: continuous, cuffless, and wearable HR and BP detection. In terms of offering the system commercially, the potential price of the cost-of-goods for the device (PMIC, MCU, and components) aligns with competing products that do not offer the benefits of long-term, continuous cardiovascular monitoring. It is also important to note that the mass production of this system and the component changes described to be made in the future will significantly decrease the overall component costs. Additionally, fabricating this design into an application-specific IC (ASIC) can also lower cost and size significantly. For these reasons, the system shows promise as a cost-effective, preventative solution to mitigating CVD-related events in underserved and underrepresented populations.

IV.7 Chapter Summary and Conclusions

In this chapter, a deep-dive analysis of the AFE was conducted to characterize the features of the system, examine the performance of the hardware designed for a dual-IPG application, and obtain an insight on the approximate cost of the circuit. For all current settings, the current source displayed the ability to withstand impedances greater than the typical range of BIO-Z near the wrist. Furthermore, the current detector proved to be precise and correlated with the current detected by the DMM; however, due to an average $62.06 \mu A$ offset, the maximum percent error by the current detector was 12.35% for a BIO-Z load. Nonetheless, since this offset was consistent for all current settings, a calibration program that removes the offset can significantly increase the accuracy of the continuous current monitor. Following accuracy examination, the automatic shutdown feature passed the functionality test and was able to deliver a “disable” signal to the PMIC.

In terms of BIO-Z calibration, five linear calibration curves were obtained and utilized to resolve the impedance of a series of nine single-dispersion Cole models. By comparing the measured impedance of the calibrated device to an LCR meter, the calibration method showed high correlation to the LCR meter and low variability between measurements. Although the statistical analysis resulted in a significant difference between the measurements of the LCR meter and the calibrated device, the percent error was small. Additionally, the mean difference between the units were minimal in comparison to the total range of basal BIO-Z near the wrist ($1.325 \Omega / 99 \Omega$).

Following calibration, a dual-IPG in vivo study was performed on six subjects. A new PTT computation method was implemented, and the approach reduced the overall variability in the average PTT when comparing to the feasibility study. Continuous measurement of HR remained precise for all test subjects. The basal and pulsatile impedances resolved from the study aligned with their expected impedance ranges determined in literature. Even more, two theories were deduced by examining the relationship between basal/pulsatile impedance, location, and sex: 1) the distal location typically relays a smaller basal impedance, yet larger pulsatile impedance in comparison to the proximal region and 2) men typically produce a smaller basal impedance, yet larger pulsatile impedance in comparison to women. Lastly, the total cost of components was examined to evaluate the cost-effectiveness of the system.

CHAPTER V

CONCLUSIONS

The goal of this work was to develop the AFE of a dual-IPG device that is compact, low-cost, and noninvasive for the continuous monitoring of cardiovascular health via HR and PTT detection. To do this, the current driving and voltage sensing networks were designed with features that allow for resolving small bio-signals, programmable output frequencies of the current driving network, and manual current adjustment to improve SNR. Following circuit design, a prototype device and signal processing code was produced to acquire dual-IPG signals and extract PTT and HR on three subjects. The results of this study demonstrated the feasibility of continuous PTT and HR detection by direct comparison to the benchtop, impedance cardiography system.

To fulfill the user needs that come with developing a wearable device, the AFE was fabricated into a 1x3 cm PCB and the current monitoring network was added for safety purposes. An in-depth characterization and analysis of the AFE was then performed on the hardware. The ULOQ of the current source was determined and ensured the system could withstand BIO-Z values that are common to the wrist region. The accuracy of the current monitor was evaluated with a resistive and BIO-Z load. This study confirmed that the measured current was consistent with that of a calibrated DMM; however, the implementation of a calibration code to shift the measurements by -62.06 μA , would result in a near-exact current measurement. The feedback loop for the automatic shutdown feature was assessed and functioned as designed. After evaluating

the current monitoring subsystem, impedance calibration was performed and validated with complex single-dispersion Cole models. The calibration approach was deemed acceptable, as the percent error, measurement variability, and correlation to the compared LCR was supportive of a restive calibration method. Additionally, this process is common for benchtop BIO-Z systems on the market.

Out of the five current magnitudes from the current source, an injection current of $565 \mu A$ displayed the most optimal attributes throughout the preliminary studies. Therefore, this current was used for an in vivo study that obtained HR, PTT, basal impedance, and pulsatile impedance on six subjects. New PTT computation methods were implemented to increase the confidence in PTT measurement by averaging the PTT from the MS, SYS, and DIA fiducial points. In doing so, the PTT variation was reduced in comparison to that of the feasibility study. The HR performance of the AFE remained consistent and precise. Lastly, the basal/pulsatile impedance obtained from each subject were reasonable in the sense that the measurements coincided with the physiological attributes of skin location versus cross sectional area and male versus female body composition in combination with cardiovascular activity.

Overall, the results presented in this work demonstrate the proof-of-concept for a bioimpedance-based wearable that is a cost-effective and cuffless solution to monitoring cardiovascular health. In the future, the AFE and MCU program can be modified to include a programmable switch with another automatic feedback loop that adjusts the magnitude of applied current based on the SNR of the IPG signals to save power. Additionally, an experiment can be performed to examine the use of the current monitor

to detect the quality in skin-electrode adherence. Since the measured current decreases as the impedance between the source and the electrodes increases, it is expected that the detected current would be far from the nominal current when electrodes are not properly mounted onto the subject. Furthermore, PTT-to-BP models should be investigated in order to map the measured PTT to the SBP and DBP of the subject. Lastly, the AFE should be integrated into ASIC to decrease cost, size, and power consumption. Once the system is optimized, it can be implemented into a fully wearable and wireless POC device for BP management and cardiovascular monitoring.

REFERENCES

- [1] V. L. Roger *et al.*, "Heart disease and stroke statistics—2011 update: a report from the American Heart Association," *Circulation*, vol. 123, no. 4, pp. e18-e209, 2011.
- [2] World Health Organization. "Cardiovascular diseases (CVDs)." World Health Organization. [https://www.who.int/news-room/fact-sheets/detail/cardiovascular-diseases-\(cvds\)](https://www.who.int/news-room/fact-sheets/detail/cardiovascular-diseases-(cvds)) (accessed November 14, 2022).
- [3] J. Frostegård, "Immunity, atherosclerosis and cardiovascular disease," *BMC medicine*, vol. 11, no. 1, pp. 1-13, 2013.
- [4] K. Sawicka, M. Szczyrek, I. Jastrzebska, M. Prasal, A. Zwolak, and J. Daniluk, "Hypertension—the silent killer," *Journal of Pre-Clinical and Clinical Research*, vol. 5, no. 2, 2011.
- [5] M. McClellan, N. Brown, R. M. Califf, and J. J. Warner, "Call to action: urgent challenges in cardiovascular disease: a presidential advisory from the American Heart Association," *Circulation*, vol. 139, no. 9, pp. e44-e54, 2019.
- [6] M. A. Carpenter *et al.*, "Laboratory, reading center, and coordinating center data management methods in the Jackson Heart Study," *The American journal of the medical sciences*, vol. 328, no. 3, pp. 131-144, 2004.
- [7] M. T. Bowers, "Cardiovascular health among an underserved population: clinical implications," *Nursing Clinics*, vol. 50, no. 3, pp. 457-464, 2015.
- [8] B. L. Rayner and J. D. Spence, "Hypertension in blacks: insights from Africa," vol. 35, ed: LWW, 2017, pp. 234-239.
- [9] M. I. Harris, R. Klein, C. C. Cowie, M. Rowland, and D. D. Byrd-Holt, "Is the risk of diabetic retinopathy greater in non-Hispanic blacks and Mexican Americans than in non-Hispanic whites with type 2 diabetes?: A US population study," *Diabetes care*, vol. 21, no. 8, pp. 1230-1235, 1998.
- [10] B. Walton-Moss, L. Samuel, T. H. Nguyen, Y. Commodore-Mensah, M. J. Hayat, and S. L. Szanton, "Community based cardiovascular health interventions in vulnerable populations: a systematic review," *The Journal of cardiovascular nursing*, vol. 29, no. 4, p. 293, 2014.
- [11] K. N. Karmali and D. M. Lloyd-Jones, "Global risk assessment to guide blood pressure management in cardiovascular disease prevention," *Hypertension*, vol. 69, no. 3, pp. e2-e9, 2017.
- [12] P. Palatini, "Heart rate as an independent risk factor for cardiovascular disease," *Drugs*, vol. 67, no. 2, pp. 3-13, 2007.
- [13] J.-C. Fruchart, M. C. Nierman, E. S. Stroes, J. J. Kastelein, and P. Duriez, "New risk factors for atherosclerosis and patient risk assessment," *Circulation*, vol. 109, no. 23_suppl_1, pp. III-15-III-19, 2004.
- [14] H. Kiers, J. Hofstra, and J. Wetzels, "Oscillometric blood pressure measurements: differences between measured and calculated mean arterial pressure," *Neth J Med*, vol. 66, no. 11, pp. 474-9, 2008.

- [15] K. Babadağ and A. Zaybak, "Comparing intra-arterial, auscultatory, and oscillometric measurement methods for arterial blood pressure," *Florence Nightingale Journal of Nursing*, vol. 29, no. 2, p. 194, 2021.
- [16] J. Liu *et al.*, "Patient-specific oscillometric blood pressure measurement," *IEEE Transactions on Biomedical Engineering*, vol. 63, no. 6, pp. 1220-1228, 2015.
- [17] T. Unger *et al.*, "2020 International Society of Hypertension global hypertension practice guidelines," *Hypertension*, vol. 75, no. 6, pp. 1334-1357, 2020.
- [18] P. Palatini, "Ambulatory and home blood pressure measurement: complementary rather than competitive methods," *Hypertension*, vol. 59, no. 1, pp. 2-4, 2012.
- [19] J. Solà and R. Delgado-Gonzalo, "The Handbook of Cuffless Blood Pressure Monitoring," *Cham: Springer*, 2019.
- [20] D. M. Bard, J. I. Joseph, and N. van Helmond, "Cuff-less methods for blood pressure telemonitoring," *Frontiers in cardiovascular medicine*, vol. 6, p. 40, 2019.
- [21] J. Balmer *et al.*, "Pre-ejection period, the reason why the electrocardiogram Q-wave is an unreliable indicator of pulse wave initialization," *Physiological measurement*, vol. 39, no. 9, p. 095005, 2018.
- [22] Y. Cao, H. Chen, F. Li, and Y. Wang, "Crisp-BP: Continuous wrist PPG-based blood pressure measurement," in *Proceedings of the 27th Annual International Conference on Mobile Computing and Networking*, 2021, pp. 378-391.
- [23] T. Boonya-Ananta, A. J. Rodriguez, V. Du Le, and J. C. Ramella-Roman, "Monte Carlo analysis of optical heart rate sensors in commercial wearables: the effect of skin tone and obesity on the photoplethysmography (PPG) signal," *Biomedical Optics Express*, vol. 12, no. 12, pp. 7445-7457, 2021.
- [24] A. Pedrana, D. Comotti, V. Re, and G. Traversi, "Development of a wearable in-ear PPG system for continuous monitoring," *IEEE Sensors Journal*, vol. 20, no. 23, pp. 14482-14490, 2020.
- [25] J. I. Rodriguez-Labra, C. Kosik, D. Maddipatla, B. B. Narakathu, and M. Z. Atashbar, "Development of a PPG sensor array as a wearable device for monitoring cardiovascular metrics," *IEEE Sensors Journal*, vol. 21, no. 23, pp. 26320-26327, 2021.
- [26] P. Mehrgardt, M. Khushi, S. Poon, and A. Withana, "Deep learning fused wearable pressure and PPG data for accurate heart rate monitoring," *IEEE Sensors Journal*, vol. 21, no. 23, pp. 27106-27115, 2021.
- [27] T. Tamura, Y. Maeda, M. Sekine, and M. Yoshida, "Wearable photoplethysmographic sensors—past and present," *Electronics*, vol. 3, no. 2, pp. 282-302, 2014.
- [28] P. C. Schönle, "A power efficient spectrophotometry & PPG integrated circuit for mobile medical instruments," ETH Zurich, 2017.
- [29] A. V. Moço, S. Stuijk, and G. de Haan, "Skin inhomogeneity as a source of error in remote PPG-imaging," *Biomedical optics express*, vol. 7, no. 11, pp. 4718-4733, 2016.
- [30] J. Fine *et al.*, "Sources of inaccuracy in photoplethysmography for continuous cardiovascular monitoring," *Biosensors*, vol. 11, no. 4, p. 126, 2021.

- [31] S. Lee, H. Shin, and C. Hahm, "Effective PPG sensor placement for reflected red and green light, and infrared wristband-type photoplethysmography," in *2016 18th International Conference on Advanced Communication Technology (ICACT)*, 2016: IEEE, pp. 556-558.
- [32] S. Alharbi, S. Hu, D. Mulvaney, and P. Blanos, "An applicable approach for extracting human heart rate and oxygen saturation during physical movements using a multi-wavelength illumination optoelectronic sensor system," in *Design and Quality for Biomedical Technologies XI*, 2018, vol. 10486: SPIE, pp. 85-99.
- [33] T.-W. Wang *et al.*, "Bio-impedance measurement optimization for high-resolution carotid pulse sensing," *Sensors*, vol. 21, no. 5, p. 1600, 2021.
- [34] K. Meng *et al.*, "Wearable pressure sensors for pulse wave monitoring," *Advanced Materials*, p. 2109357, 2022.
- [35] S. Zhao *et al.*, "3D dielectric layer enabled highly sensitive capacitive pressure sensors for wearable electronics," *ACS applied materials & interfaces*, vol. 12, no. 28, pp. 32023-32030, 2020.
- [36] K. Bayoumy *et al.*, "Smart wearable devices in cardiovascular care: where we are and how to move forward," *Nature Reviews Cardiology*, vol. 18, no. 8, pp. 581-599, 2021.
- [37] B. Brown. "Cuff-Free BP Wearable Gets CE and FDA Clearance [video]." Health Tech Insider. <https://healthtechinsider.com/2022/07/18/cuff-free-bp-wearable-gets-ce-and-fda-clearance-video/> (accessed December 3, 2022).
- [38] A. Ivorra, "Bioimpedance monitoring for physicians: an overview," *Centre Nacional de Microelectrònica Biomedical Applications Group*, vol. 11, no. 17, 2003.
- [39] T. K. Bera, "Bioelectrical impedance methods for noninvasive health monitoring: a review," *Journal of medical engineering*, vol. 2014, 2014.
- [40] C. Corciova, R. Ciorap, D. Zaharia, and D. Matei, "Hemodynamic monitoring using peripheral impedance plethysmography," in *2011 7TH INTERNATIONAL SYMPOSIUM ON ADVANCED TOPICS IN ELECTRICAL ENGINEERING (ATEE)*, 2011: IEEE, pp. 1-4.
- [41] S. Kaufmann, A. Malhotra, G. Ardel, and M. Ryschka, "A high accuracy broadband measurement system for time resolved complex bioimpedance measurements," *Physiological Measurement*, vol. 35, no. 6, p. 1163, 2014.
- [42] G. McConnell, "The use of impedance plethysmography to predict the onset of blood flow beneath a tourniquet cuff," University of British Columbia, 1988.
- [43] Z. Cheng *et al.*, "Smart handheld medical device with patient-specific force regulation mechanism," *Assembly Automation*, 2022.
- [44] P. Kassanos, "Bioimpedance sensors: A tutorial," *IEEE Sensors Journal*, 2021.
- [45] R. E. Dodde, G. H. Kruger, and A. J. Shih, "Design of bioimpedance spectroscopy instrument with compensation techniques for soft tissue characterization," *Journal of Medical Devices*, vol. 9, no. 2, 2015.
- [46] J. Nyboer, M. M. Kreider, and L. Hannapel, "Electrical impedance plethysmography: a physical and physiologic approach to peripheral vascular study," *Circulation*, vol. 2, no. 6, pp. 811-821, 1950.

- [47] E. Piuze, S. Pisa, E. Pittella, L. Podestà, and S. Sangiovanni, "Low-cost and portable impedance plethysmography system for the simultaneous detection of respiratory and heart activities," *IEEE Sensors Journal*, vol. 19, no. 7, pp. 2735-2746, 2018.
- [48] D. Naranjo-Hernández, J. Reina-Tosina, and M. Min, "Fundamentals, recent advances, and future challenges in bioimpedance devices for healthcare applications," *Journal of Sensors*, vol. 2019, 2019.
- [49] J. Heikenfeld *et al.*, "Wearable sensors: modalities, challenges, and prospects," *Lab on a Chip*, vol. 18, no. 2, pp. 217-248, 2018.
- [50] H. Caytak, A. Boyle, A. Adler, and M. Bolic, "Bioimpedance spectroscopy processing and applications," *Encyclopedia of Biomedical Engineering*, vol. 3, pp. 265-279, 2019.
- [51] S. Yao and Y. Zhu, "Nanomaterial-enabled dry electrodes for electrophysiological sensing: A review," *Jom*, vol. 68, no. 4, pp. 1145-1155, 2016.
- [52] K. Pesti, M. Metshein, P. Annus, H. Kõiv, and M. Min, "Electrode placement strategies for the measurement of radial artery bioimpedance: Simulations and experiments," *IEEE Transactions on Instrumentation and Measurement*, vol. 70, pp. 1-10, 2020.
- [53] M. Jaffrin and C. Vanhoutte, "Quantitative interpretation of arterial impedance plethysmographic signals," *Medical and Biological Engineering and Computing*, vol. 17, no. 1, pp. 2-10, 1979.
- [54] L. D. Trong, L. N. Quang, D. H. Anh, D. D. Tuan, H. N. Chi, and D. N. Minh, "A portable band-shaped bioimpedance system to monitor the body fat and fasting glucose level," *Journal of Electrical Bioimpedance*, vol. 13, no. 1, pp. 54-65, 2022.
- [55] N. D. P. Ferreira, C. Gehin, and B. Massot, "A review of methods for non-invasive heart rate measurement on wrist," *IRBM*, vol. 42, no. 1, pp. 4-18, 2021.
- [56] A. Hammoud *et al.*, "Multi-Channel Bioimpedance System for Detecting Vascular Tone in Human Limbs: An Approach," *Sensors*, vol. 22, no. 1, p. 138, 2021.
- [57] Analog Devices. "AD9837." Analog Devices. <https://www.analog.com/media/en/technical-documentation/data-sheets/AD9837.PDF> (accessed January 2., 2023).
- [58] R. Mancini and R. Palmer. "Sine-Wave Oscillator." Texas Instruments. <https://www.ti.com/lit/an/sloa060/sloa060.pdf?ts=1674003926472#:~:text=8.1%20Wein%20Bridge%20Oscillator,components%20and%20good%20frequency%20stability.> (accessed January 5., 2023).
- [59] Texas Instruments. "AN-1515 A Comprehensive Study of the Howland Current Pump." Texas Instruments. <https://www.ti.com/lit/an/snoa474a/snoa474a.pdf> (accessed January 8, 2023).
- [60] I. V. Lam. "Analysis of Improved Howland Current Pump Configurations." Texas Instruments.

- https://www.ti.com/lit/an/sboa437/sboa437.pdf?ts=1674080601608&ref_url=https%253A%252F%252Fwww.google.com%252F (accessed January 11, 2023).
- [61] T. Menden, J. Matuszczyk, S. Leonhardt, and M. Walter, "Bandwidth and Common Mode Optimization for Current and Voltage Sources in Bioimpedance Spectroscopy," *Journal of Electrical Bioimpedance*, vol. 12, no. 1, pp. 135-146, 2021.
- [62] W. R. Lionheart, J. Kaipio, and C. N. McLeod, "Generalized optimal current patterns and electrical safety in EIT," *Physiological measurement*, vol. 22, no. 1, p. 85, 2001.
- [63] M. A. Callejón, P. Del Campo, J. Reina-Tosina, and L. M. Roa, "A parametric computational analysis into galvanic coupling intrabody communication," *IEEE Journal of Biomedical and Health Informatics*, vol. 22, no. 4, pp. 1087-1096, 2017.
- [64] C. Newcombe. "Facts About True-RMS Measurement." Fluke. <https://www.fluke.com/en-us/learn/blog/digital-multimeters/facts-about-true-rms-measurement> (accessed November 3, 2022).
- [65] L. M. Tolbert, H. D. Hollis, and P. S. Hale, "Survey of harmonics measurements in electrical distribution systems," in *IAS'96. Conference Record of the 1996 IEEE Industry Applications Conference Thirty-First IAS Annual Meeting*, 1996, vol. 4: IEEE, pp. 2333-2339.
- [66] S. Ha *et al.*, "Integrated circuits and electrode interfaces for noninvasive physiological monitoring," *IEEE Transactions on biomedical engineering*, vol. 61, no. 5, pp. 1522-1537, 2014.
- [67] A. L.-I. Amplifiers. "About Lock-In Amplifiers." Stanford Research Systems. (accessed Jan 28, 2023).
- [68] Analog Devices. "Balanced Modulator/Demodulator Data Sheet AD630." Analog Devices. <https://www.analog.com/media/en/technical-documentation/data-sheets/AD630.pdf> (accessed January 20, 2023).
- [69] J. Gomez-Clapers, R. Casanella, and R. Pallas-Areny, "A novel method to obtain proximal plethysmographic information from distal measurements using the impedance plethysmogram," *Journal of Electrical Bioimpedance*, vol. 6, no. 1, pp. 44-48, 2015.
- [70] L. D'Alvia *et al.*, "Tetrapolar low-cost systems for thoracic impedance plethysmography," in *2018 IEEE International Symposium on Medical Measurements and Applications (MeMeA)*, 2018: IEEE, pp. 1-6.
- [71] BIOPAC Systems Inc. "Z IMPEDANCE CALIBRATOR – EBI100C/NICO100C." BIOPAC Systems Inc.,. <https://www.biopac.com/product/z-impedance-calibrator-ebi100cnico100c/> (accessed December 17, 2022).
- [72] W. C. Fornetti, J. M. Pivarnik, J. M. Foley, and J. J. Fiechtner, "Reliability and validity of body composition measures in female athletes," *Journal of Applied Physiology*, vol. 87, no. 3, pp. 1114-1122, 1999.

- [73] Y. Yang, J. Wang, G. Yu, F. Niu, and P. He, "Design and preliminary evaluation of a portable device for the measurement of bioimpedance spectroscopy," *Physiological Measurement*, vol. 27, no. 12, p. 1293, 2006.

APPENDIX A
IN VIVO STUDY DATA

Table 15. In Vivo Study: Detected PTT from MS, DIA, and SYS Fiducial Points

Subject #	PTT_MS					PTT_DIA					PTT_SYS					PTT Overall (ms)	
	T1 (s)	T2 (s)	T3 (s)	AVG (ms)	STD (ms)	T1 (s)	T2 (s)	T3 (s)	AVG (ms)	STD (ms)	T1 (s)	T2 (s)	T3 (s)	AVG (ms)	STD (ms)	AVG	STD
1	0.006	0.006	0.006	5.721	0.159	0.007	0.007	0.007	7.242	0.216	0.008	0.004	0.008	6.738	2.198	6.567	0.775
2	0.010	0.007	0.007	8.096	1.996	0.009	0.008	0.006	7.610	1.396	0.008	0.010	0.008	8.473	1.035	8.060	0.433
3	0.002	0.009	0.006	5.797	3.487	0.006	0.007	0.008	6.830	0.835	0.005	0.004	0.007	5.107	1.304	5.911	0.867
4	0.004	0.004	0.005	4.582	0.699	0.005	0.005	0.008	6.030	1.383	0.003	0.003	0.005	3.842	0.874	4.818	1.113
5	0.010	0.007	0.009	8.923	1.473	0.009	0.009	0.008	8.623	0.613	0.012	0.010	0.010	10.644	1.063	9.397	1.091
6	0.011	0.010	0.009	9.916	1.244	0.007	0.009	0.013	9.797	3.126	0.014	0.009	0.019	13.890	4.856	11.201	2.330

Table 16. In Vivo Study: Detected HR and Applied Current

Subject #	HR (BPM)					Current (uA)				
	T1	T2	T3	AVG	STD	T1	T2	T3	AVG	STD
1	77.00	78.00	78.00	77.67	0.58	578.02	577.91	577.88	577.94	0.07
2	75.00	78.00	74.00	75.67	2.08	577.86	578.15	578.05	578.02	0.15
3	82.00	83.00	83.00	82.67	0.58	578.14	578.13	578.07	578.12	0.04
4	68.00	67.00	69.00	68.00	1.00	580.01	579.96	579.99	579.99	0.03
5	75.00	76.00	72.00	74.33	2.08	582.11	582.15	582.41	582.22	0.16
6	80.00	84.00	78.00	80.67	3.06	577.82	577.81	578.02	577.88	0.12

Table 17. In Vivo Study: Measured Basal and Pulsatile Impedance at the Proximal Electrode Pair

Subject #	Avg Basal Impedance (Proximal) (Ω)					Averag Pulsatile Impedance (Proximal) (Ω)				
	T1	T2	T3	AVG	STD	T1	T2	T3	AVG	STD
1	67.546	66.588	66.952	67.028	0.484	0.032	0.030	0.026	0.029	0.003
2	54.243	54.310	54.151	54.234	0.080	0.014	0.015	0.013	0.014	0.001
3	64.993	64.034	63.482	64.170	0.765	0.037	0.035	0.030	0.034	0.004
4	57.071	56.875	56.847	56.931	0.122	0.064	0.068	0.066	0.066	0.002
5	49.913	49.605	49.657	49.725	0.165	0.043	0.046	0.044	0.044	0.001
6	42.330	42.315	41.992	42.213	0.191	0.014	0.023	0.011	0.016	0.006

Table 18. In Vivo Study: Measured Basal and Pulsatile Impedance at the Distal Electrode Pair

Subject #	Avg Basal Impedance (Distal) (Ω)					Averag Pulsatile Impedance (Distal) (Ω)				
	T1	T2	T3	AVG	STD	T1	T2	T3	AVG	STD
1	54.848	55.051	55.263	55.054	0.207	0.038	0.050	0.037	0.041	0.007
2	41.666	41.807	41.948	41.807	0.141	0.034	0.040	0.036	0.036	0.003
3	52.202	51.777	51.476	51.818	0.365	0.041	0.036	0.044	0.040	0.004
4	55.122	54.837	54.560	54.840	0.281	0.092	0.100	0.085	0.092	0.007
5	37.893	37.690	37.645	37.743	0.132	0.058	0.058	0.060	0.059	0.001
6	30.380	30.319	30.488	30.396	0.086	0.021	0.030	0.015	0.022	0.007

APPENDIX B

MATLAB CODE FOR DUAL-IPG SIGNAL PROCESSING, FEATURE EXTRACTION, AND BASELINE/PULSATILE IMPEDANCE ACQUISITION

```
%%  
close all  
clc  
clear  
  
%% Get Data  
[name, folder] = uigetfile('.csv');  
cd(folder)  
  
data = table2array(readtable(name));  
data3= data(:,3);  
CURRENT = (mean(data3)/100) *10^6;  
  
%% Settings  
  
fs = 10001; %sampling frequenxy  
lowp_freq = 4.5; %lpf cutoff frequency  
envelope_number = 1;  
peak_number = 0.6;  
x1 = 0;  
x2 =60;  
  
len = length(data); % length of signal  
time_axis = 0:1/fs:((len-1)/fs);  
freq_axis = fs*(0:(len-1))/len;  
  
    signal=data(:,1); %IPG signal 1  
    %signal = 1.*(signal - mean(signal));  
    signal2=data(:,2); %IPG signal 2  
    %signal2 = 1.*(signal2 - mean(signal2));  
  
    %filter  
    [recovered_signal,d] =  
    lowpass(signal,lowp_freq,fs,'ImpulseResponse','iir','Steepness',0.85);  
    [recovered_signal2,d2] =  
    lowpass(signal2,lowp_freq,fs,'ImpulseResponse','iir','Steepness',0.85);  
  
    %find low envelope  
    [hi , lo] =  
    envelope(recovered_signal,round(fs/envelope_number),'peak');  
    sig_no_env = recovered_signal - lo; %remove envelope  
    [hi2 , lo2] =  
    envelope(recovered_signal2,round(fs/envelope_number),'peak');
```

```

sig_no_env2 = recovered_signal2 - lo2; %remove envelope

%derivative
y = gradient(sig_no_env);
y2 = gradient(sig_no_env2);

%plot
figure(1)
subplot(6,2,1)
hold on
plot(time_axis,signal,'k')
xlim([x1,x2])
title('Measured Signal IPG 1')
ylabel('Voltage (V)')
xlabel('Time(s)')
hold off

subplot(6,2,2)
hold on
plot(time_axis,signal2,'r')
xlim([x1,x2])
title('Measured Signal IPG 2')
ylabel('Voltage (V)')
xlabel('Time(s)')
hold off

subplot(6,2,3)
hold on
plot(time_axis, lo,'c')
plot(time_axis,recovered_signal,'k')
xlim([x1,x2])
title('Filtered Signal w/ Envelope')
xlabel('Time(s)')
ylabel('Voltage (V)')
legend('Envelope','IPG 1')
hold off

subplot(6,2,4)
hold on
plot(time_axis, lo2,'y')
plot(time_axis,recovered_signal2,'r')
xlim([x1,x2])
title('Filtered Signal 2 w/ Envelope')
xlabel('Time(s)')
ylabel('Voltage (V)')
legend('Envelope','IPG 2')
hold off

subplot(6,2,5)
hold on
plot(time_axis, sig_no_env,'k')
xlim([x1,x2])
title('Filtered Signal 1 w/o Envelope')
ylabel('Voltage (V)')
xlabel('Time(s)')

```

```

hold off

subplot(6,2,6)
hold on
plot(time_axis, sig_no_env2,'r')
xlim([x1,x2])
title('Filtered Signal 2 w/o Envelope')
ylabel('Voltage (V)')
xlabel('Time(s)')
hold off

subplot(6,2,7)
hold on
plot(time_axis, y,'k')
xlim([x1,x2])
title('First Derivative 1')
ylabel('First Derivative (dV/dt)')
xlabel('Time(s)')
hold off

subplot(6,2,8)
hold on
plot(time_axis, y2,'r')
xlim([x1,x2])
title('First Derivative 2')
ylabel('First Derivative (dV/dt)')
xlabel('Time(s)')
hold off

subplot(6,2,9:10)
hold on
plot(time_axis, sig_no_env,'k')
plot(time_axis, sig_no_env2,'r')
xlim([x1,x2])
title('Filtered Signal w/o Envelope')
xlabel('Time(s)')
ylabel('Volatage (V)')
legend('IPG 1', 'IPG 2')
hold off

subplot(6,2,11:12)
hold on
plot(time_axis, y,'k')
plot(time_axis, y2,'r')
xlim([x1,x2])
title('First Derivative')
ylabel('First Derivative (dV/dt)')
xlabel('Time(s)')
legend('IPG 1',' IPG 2')
hold off

subplot(6,2,9:10)
hold on
plot(time_axis, sig_no_env,'k')
plot(time_axis, sig_no_env2,'r')

```

```

xlim([x1,x2])
title('Filtered Signal w/o Envelope')
ylabel('Volatage (V)')
xlabel('Time(s)')
legend('IPG 1', 'IPG 2')
hold off

subplot(6,2,11:12)
hold on
plot(time_axis, y,'k')
plot(time_axis, y2,'r')
xlim([x1,x2])
title('First Derivative')
ylabel('First Derivative (dV/dt)')
xlabel('Time(s)')
legend('IPG 1',' IPG 2')
hold off

figure(2)
subplot(2,1,1)
hold on
plot(time_axis, sig_no_env,'k')
plot(time_axis, sig_no_env2,'r')
xlim([x1,x2])
title('AC Component of IPG Signal')
xlabel('Time(s)')
ylabel('Volatage (V)')
legend('IPG 1', 'IPG 2')
hold off

subplot(2,1,2)
hold on
plot(time_axis, y,'k')
plot(time_axis, y2,'r')
xlim([x1,x2])
title('1st Deriv.')
ylabel('1st Deriv. (dV/dt)')
xlabel('Time(s)')
legend('IPG 1',' IPG 2')
hold off

%%

sig_no_env_neg = -1*sig_no_env;
sig_no_env_neg2 = -1*sig_no_env2;
y_neg = -1*y;
y2_neg = -1*y2;
[pks,locs] =
findpeaks(sig_no_env,fs,"MinPeakDistance",peak_number);
[pks2,locs2] =
findpeaks(sig_no_env2,fs,"MinPeakDistance",peak_number);
[pks_neg,locs_neg] =
findpeaks(sig_no_env_neg,fs,"MinPeakDistance",peak_number);
[pks2_neg,locs2_neg] =
findpeaks(sig_no_env_neg2,fs,"MinPeakDistance",peak_number);

```

```

    [pks_y_neg,locs_y_neg] =
findpeaks(y_neg,fs,"MinPeakDistance",peak_number,'MinPeakHeight',.1e-
6);
    [pks_y2_neg,locs_y2_neg] =
findpeaks(y2_neg,fs,"MinPeakDistance",peak_number,'MinPeakHeight',.1e-
6);

    figure(3)
    subplot(5,2,1)
    hold on
    plot(time_axis,signal,'k')
    xlim([x1,x2])
    title('Raw Signal IPG - Proximal')
    ylabel('Voltage (V)')
    xlabel('Time(s)')
    hold off

    subplot(5,2,2)
    hold on
    plot(time_axis,signal2,'r')
    xlim([x1,x2])
    ylabel('Voltage (V)')
    title('Raw Signal - Distal')
    xlabel('Time(s)')
    hold off

    subplot(5,2,3)
    hold on
    %plot(time_axis, lo,'c')
    plot(time_axis,recovered_signal,'k')
    xlim([x1,x2])
    %title('Filtered Signal 1 w/ Envelope (DC Component)')
    title('Filtered Signal - Proximal')
    xlabel('Time(s)')
    ylabel('Voltage (V)')
    %legend('Envelope/DC','Filtered IPG 1')
    hold off

    subplot(5,2,4)
    hold on
    %plot(time_axis, lo2,'y')
    plot(time_axis,recovered_signal2,'r')
    xlim([x1,x2])
    % title('Filtered Signal 2 w/ Envelope (DC Component)')
    title('Filtered Signal - Distal')
    xlabel('Time(s)')
    ylabel('Voltage (V)')
    %legend('Envelope/DC','Filtered IPG 2')
    hold off

    subplot(5,2,5)
    hold on
    plot(time_axis, lo,'c')
    xlim([x1,x2])
    title('DC Component - Proximal')

```

```

ylabel('Voltage (V)')
xlabel('Time(s)')
hold off

subplot(5,2,6)
hold on
plot(time_axis, lo2,'g')
xlim([x1,x2])
title('DC Component - Distal')
ylabel('Voltage (V)')
xlabel('Time(s)')
hold off

subplot(5,2,7)
hold on
plot(time_axis, sig_no_env,'k')
scatter(locs_neg, -1*pks_neg,'filled')
scatter(locs, pks, 'k','filled')
xlim([x1,x2])
title('AC Component - Proximal')
ylabel('Voltage (V)')
xlabel('Time(s)')
legend('AC of IPG Proximal', 'SYS Foot','DIA PEAK')
hold off

subplot(5,2,8)
hold on
plot(time_axis, sig_no_env2,'r')
scatter(locs2_neg, -1*pks2_neg,'filled')
scatter(locs2, pks2, 'k','filled')
xlim([x1,x2])
title('AC Component - Distal')
ylabel('Voltage (V)')
xlabel('Time(s)')
legend('AC of IPG - Distal', 'SYS Foot','DIA PEAK')
hold off

subplot(5,2,9)
hold on
plot(time_axis, y,'k')
scatter(locs_y_neg, -1*pks_y_neg)
xlim([x1,x2])
title('1st Deriv. 1')
ylabel('1st Deriv. 1 (dV/dt)')
legend('Deriv of IPG 1', 'MS Peak')
xlabel('Time(s)')
hold off

subplot(5,2,10)
hold on
plot(time_axis, y2,'r')
scatter(locs_y2_neg, -1*pks_y2_neg)
xlim([x1,x2])
title('1st Deriv. 2')
ylabel('1st Deriv. 2 (dV/dt)')

```

```

        legend('Deriv of IPG 2', 'MS Peak')
        xlabel('Time(s)')
        hold off
%%
        figure(4)
        subplot(2,1,1)
        hold on
        plot(time_axis, sig_no_env,'k')
        plot(time_axis, sig_no_env2,'r')
        scatter(locs, pks, 'k')
        scatter(locs2, pks2,'r')
        scatter(locs_neg, -1*pks_neg,'filled','k')
        scatter(locs2_neg, -1*pks2_neg,'filled','r')
        xlim([x1,x2])
        title('AC Component of IPG Signal')
        xlabel('Time(s)')
        ylabel('Volatage (V)')
        legend('IPG 1', 'IPG 2','DIA PEAK 1','DIA PEAK 2','SYS Foot 1','SYS
Foot 2')
        hold off

        subplot(2,1,2)
        hold on
        plot(time_axis, y,'k')
        plot(time_axis, y2,'r')
        scatter(locs_y_neg, -1*pks_y_neg,'filled','k')
        scatter(locs_y2_neg, -1*pks_y2_neg, 'filled','r')
        xlim([x1,x2])
        title('1st Deriv.')
        ylabel('1st Deriv. (dV/dt)')
        xlabel('Time(s)')
        legend('IPG 1', ' IPG 2', 'MS PEAK 1', 'MS PEAK 2')
        hold off

%% ms ptt

ms_y1 = locs_y_neg( locs_y_neg >= x1 & x2 >= locs_y_neg);
ms_y2= locs_y2_neg( locs_y2_neg >= x1 & x2 >= locs_y2_neg);
length_y2 = length(ms_y2);
length_y1 = length(ms_y1);
keep_y2 = [];
keep_y1 = [ ];

if length_y2 < length_y1
    for i = 1:length_y2
        for j = 1:length_y1
            diff_ms = abs(ms_y2(i) - ms_y1(j));
            if diff_ms <.2
                length_keep_y1 = length(keep_y1);
                length_keep_y2 = length(keep_y2);
                keep_y1(length_keep_y1+1) = ms_y1(j);
                keep_y2(length_keep_y2+1) = ms_y2(i);
            end
        end
    end
end

```



```

        end
elseif length_y2 > length_y1
    for i = 1:length_y1
        for j = 1:length_y2
            diff_ms = abs(ms_y1(i) - ms_y2(j));
            if diff_ms <.2
                length_keep_y1 = length(keep_y1);
                length_keep_y2 = length(keep_y2);
                keep_y1(length_keep_y1+1) = ms_y1(i);
                keep_y2(length_keep_y2+1) = ms_y2(j);
            end
        end
    end
end
else
    for i = 1:length_y1
        for j = 1:length_y2
            diff_ms = abs(ms_y1(i) - ms_y2(j));
            if diff_ms <.2
                length_keep_y1 = length(keep_y1);
                length_keep_y2 = length(keep_y2);
                keep_y1(length_keep_y1+1) = ms_y1(i);
                keep_y2(length_keep_y2+1) = ms_y2(j);
            end
        end
    end
end

end

%% DIA ptt

ms_dia1 = locs( locs>= x1 & x2 >= locs);
ms_dia2= locs2( locs2 >= x1 & x2 >= locs2);
length_dia2 = length(ms_dia2);
length_dia1 = length(ms_dia1);
keep_dia2 = [];
keep_dia1 = [ ];

if length_dia2 < length_dia1
    for k = 1:length_dia2
        for l = 1:length_dia1
            diff_dia = abs(ms_dia2(k) - ms_dia1(l));
            if diff_dia <.2
                length_keep_dia1 = length(keep_dia1);
                length_keep_dia2 = length(keep_dia2);
                keep_dia1(length_keep_dia1+1) = ms_dia1(l);
                keep_dia2(length_keep_dia2+1) = ms_dia2(k);
            end
        end
    end
end
elseif length_dia2 > length_dia1
    for k = 1:length_dia1
        for l= 1:length_dia2
            diff_dia = abs(ms_dia1(k) - ms_dia2(l));
            if diff_dia <.2
                length_keep_dia1 = length(keep_dia1);
                length_keep_dia2 = length(keep_dia2);

```

```

        keep_dia1(length_keep_dia1+1) = ms_dia1(k);
        keep_dia2(length_keep_dia2+1) = ms_dia2(l);
    end
end
end
else
    for k = 1:length_dia1
        for l = 1:length_dia2
            diff_dia = abs(ms_dia1(k) - ms_dia2(l));
            if diff_dia <.2
                length_keep_dia1 = length(keep_dia1);
                length_keep_dia2 = length(keep_dia2);
                keep_dia1(length_keep_dia1+1) = ms_dia1(k);
                keep_dia2(length_keep_dia2+1) = ms_dia2(l);
            end
        end
    end
end
end

%% SYS ptt

ms_sys1 = locs_neg( locs_neg>= x1 & x2 >= locs_neg);
ms_sys2= locs2_neg( locs2_neg >= x1 & x2 >= locs2_neg);
length_sys2 = length(ms_sys2);
length_sys1 = length(ms_sys1);
keep_sys2 = [];
keep_sys1 = [ ];

if length_sys2 < length_sys1
    for m = 1:length_sys2
        for n = 1:length_sys1
            diff_sys = abs(ms_sys2(m) - ms_sys1(n));
            if diff_sys <.2
                length_keep_sys1 = length(keep_sys1);
                length_keep_sys2 = length(keep_sys2);
                keep_sys1(length_keep_sys1+1) = ms_sys1(n);
                keep_sys2(length_keep_sys2+1) = ms_sys2(m);
            end
        end
    end
elseif length_sys2 > length_sys1
    for m = 1:length_sys1
        for n= 1:length_sys2
            diff_sys = abs(ms_sys1(m) - ms_sys2(n));
            if diff_sys <.2
                length_keep_sys1 = length(keep_sys1);
                length_keep_sys2 = length(keep_sys2);
                keep_sys1(length_keep_sys1+1) = ms_sys1(m);
                keep_sys2(length_keep_sys2+1) = ms_sys2(n);
            end
        end
    end
end
else

```

```

    for m = 1:length_sys1
        for n = 1:length_sys2
            diff_sys = abs(ms_sys1(m) - ms_sys2(n));
            if diff_sys < .2
                length_keep_sys1 = length(keep_sys1);
                length_keep_sys2 = length(keep_sys2);
                keep_sys1(length_keep_sys1+1) = ms_sys1(m);
                keep_sys2(length_keep_sys2+1) = ms_sys2(n);
            end
        end
    end
end

ms_time = keep_y2-keep_y1;
ptt_ms = ms_time(ms_time > 0 & ms_time < .3);
avg_ptt_ms = mean(ptt_ms);
ptt_std_ms = std(ptt_ms);

ms_logic_error_neg = ms_time > 0;
ms_logic_error_unreal = ms_time < .3;
ms_del_error_neg = sum(ms_logic_error_neg(:) == 0);
ms_del_error_unreal = sum(ms_logic_error_unreal(:) == 0);
ms_ratio_del_neg = (ms_del_error_neg/length(ms_time)) *100;
ms_ratio_del_unreal = (ms_del_error_unreal/length(ms_time))*100;

dia_time = keep_dia2-keep_dia1;
ptt_dia = dia_time(dia_time > 0 & dia_time < .3);
avg_ptt_dia= mean(ptt_dia);
ptt_std_dia = std(ptt_dia);
ratio_dia = length(ptt_dia)/length(dia_time) *100;

dia_logic_error_neg = dia_time > 0;
dia_logic_error_unreal = dia_time < .3;
dia_del_error_neg = sum(dia_logic_error_neg(:) == 0);
dia_del_error_unreal = sum(dia_logic_error_unreal(:) == 0);
dia_ratio_del_neg = (dia_del_error_neg/length(dia_time)) *100;
dia_ratio_del_unreal = (dia_del_error_unreal/length(dia_time))*100;

sys_time = keep_sys2-keep_sys1;
ptt_sys = sys_time(sys_time > 0 & sys_time < .3);
avg_ptt_sys= mean(ptt_sys);
ptt_std_sys = std(ptt_sys);
ratio_sys = length(ptt_sys)/length(sys_time) *100;

sys_logic_error_neg = sys_time > 0;
sys_logic_error_unreal = sys_time < .3;
sys_del_error_neg = sum(sys_logic_error_neg(:) == 0);
sys_del_error_unreal = sum(sys_logic_error_unreal(:) == 0);
sys_ratio_del_neg = (sys_del_error_neg/length(sys_time)) *100;
sys_ratio_del_unreal = (sys_del_error_unreal/length(sys_time))*100;

%% Calibration
logic_cal = time_axis >= x1 & time_axis <= x2;

lo_cal_prox = (lo(logic_cal) -.0255) ./ .0203;

```

```
lo2_cal_distal = (lo2(logic_cal) -.0255) ./ .0203;
hi_cal_prox = (hi(logic_cal) -.0255) ./ .0203;
hi2_cal_distal = (hi2(logic_cal) -.0255) ./ .0203;

zb_distal_avg = mean(lo2_cal_distal);
zb_prox_avg = mean(lo_cal_prox);
zb_distal_std = std(lo2_cal_distal);
zb_prox_std = std(lo_cal_prox);

Zp_distal_avg = mean(hi2_cal_distal-lo2_cal_distal);
Zp_prox_avg= mean(hi_cal_prox-lo_cal_prox);
Zp_distal_std = std(hi2_cal_distal-lo2_cal_distal);
Zp_prox_std = std(hi_cal_prox-lo_cal_prox);
```